

Structural Analysis of Cylindrical Particles by Small Angle X-ray Scattering

DISSERTATION

Zur Erlangung des akademischen Grades eines
Doktors der Naturwissenschaften (Dr. rer. Nat.)
in Fach Chemie der Fakultät für Biologie, Chemie und Geowissenschaften
der Universität Bayreuth

vorgelegt von
Li Li, M. Sci.
aus Sichuan, VR China

Bayreuth, 2005

Die vorliegende Arbeit wurde in der Zeit von April 2001 bis Dezember 2003 am Polymer-Institut der Universität Karlsruhe (TH) und von Januar 2004 bis November 2004 am Lehrstuhl für Physikalische Chemie I der Universität Bayreuth unter Betreuung von Herrn Prof. Dr. M. Ballauff angefertigt.

Vollständiger Abdruck der von der Fakultät für Biologie, Chemie und Geowissenschaften der Universität Bayreuth zur Erlangung des akademischen Grades eines Doktors der Naturwissenschaften genehmigten Dissertation.

| | |
|---|------------|
| Dissertation eingereicht am: | 12.01.2005 |
| Zulassung durch die Promotionskommission: | 19.01.2005 |
| Wissenschaftliches Kolloquium: | 09.05.2005 |

Amtierender Dekan: Prof. Dr. O. Meyer

Prüfungsausschuß:

Prof. Dr. M. Ballauff (Erstgutachter)
Prof. Dr. G. Krausch (Zweitgutachter)
Prof. Dr. J. Breu (Vorsitzender)
Prof. Dr. P. Strohrig

Acknowledgements

First of all, I would like to express my deepest gratitude to Prof. Dr. M. Ballauff, for being an outstanding advisor. Thank him for giving me the interesting subjects, many valuable discussions during this work, and being very helpful for the publications and this thesis.

I would like to thank the groups of Prof. Dr. J. Beck and Prof. Dr. Höger for kindly providing samples and many helpful discussions during our collaborations in projects of polymer carbon suboxide system and block copolymer system, respectively. Many thanks are given to Dr. L. Harnau for his outstanding contribution to the simulation work on interparticle interactions of Laponite.

I am grateful to all of my colleagues, who have constructed a very friendly atmosphere for working. I give my acknowledgement especially to Dr. S. Rosenfeldt for her critical reading of this thesis and many helps in my private life, to colleagues Dr. N. Dingenouts and Dr. J. Bolze, who paid a lot of time to answer my questions about adjustment of Kratky-Camera and computer simulation problems. They also discussed with me about part of this work and gave good suggestions. I appreciate Dr. A. Wittemann and E. Breiniger for the nice correction of German abstract of this thesis. I thank Dr. D. Pontoni, Dr. S. Rosenfeldt, M. Partel and B. Haupt for their help in SAXS measurements of Laponite in Grenoble, France. I thank B. Haupt and Y. Mei very much for their help in solving computer problems. Thanks are also given to H. Kuhn, A. Wolfgang, Dr. M. Zhang and H. Hörig for their helps in techniques for instruments of Kratky-Camera, sophica and refractor meter. I treasure the friendship with my colleagues Y. Mei, Dr. J. Bolze, Dr. A. Kellarakis, Dr. Y. Lu, J. Crassous and M. Partel.

My special thanks are given to my family. My husband Xuhong has encouraged me and shown his appreciation for my every progress in this work, although he could not be always beside me; my daughter Chuwen and son Hanxi have given me a lot of delicious time for working instead of playing with them. Without their understanding and support it is impossible to finish this work.

To Xuhong, Chuwen and Hanxi

Structural Analysis of cylindrical Particles by Small Angle X-ray Scattering

Contents

| | |
|--|-----------|
| 1 Introduction and motivation | 9 |
| 2 Theory of SAXS | 12 |
| 2.1 Introduction | 12 |
| 2.2 Scattering functions of single cylindrical particles | 17 |
| 2.2.1 Long rods | 18 |
| 2.2.2 Disc-shaped particles | 21 |
| 2.2.3 Polymer chains in solution | 23 |
| 2.2.4 Semi-flexible chains | 25 |
| 2.3 Interparticle interference; Structure factor | 32 |
| 2.3.1 Systems of identical particles | 33 |
| 2.3.2 Polydisperse systems | 37 |
| 2.4 Interpretation of scattering functions | 44 |
| 3 Experimental techniques | 46 |
| 3.1 SAXS by a modified Kratky-Compact-Camera | 46 |
| 3.1.1 Construction and set-up of Kratky-Compact-Camera | 46 |
| 3.1.2 Smearing | 48 |
| 3.1.3 Data treatment | 49 |
| 3.2 SAXS by Synchrotron | 58 |
| 3.3 Static light scattering | 60 |
| 3.4 Mass density measurement | 61 |

4 Structural analysis and interaction of Laponite particles in aqueous solutions **63**

| | |
|--|----|
| 4.1 Introduction | 63 |
| 4.2 Sample preparation | 67 |
| 4.3 Experimental form factor and determination of size and shape of Laponite particles | 68 |
| 4.4 Influence of finite concentration: Structure factor $S(q,c)$ | 75 |
| 4.4.1 Apparent virial coefficient B_{app} | 75 |
| 4.4.2 Structure factor and consistency check | 76 |
| 4.4.3 Comparison of $S(q,c)$ with multicomponent interaction site model | 81 |
| 4.5 Conclusion | 84 |

5 Structural analysis of Poly(carbon suboxide) in binary water/DMF solutions **85**

| | |
|---|-----|
| 5.1 Introduction | 85 |
| 5.2 Investigated samples | 86 |
| 5.3 Scattering result and structural analysis for polymer dissolved in water/DMF of 10/90 | 87 |
| 5.3.1 Comparison of different evaluation processes of scattering data | 87 |
| 5.3.2 Structural analysis | 94 |
| 5.4 Effect of binary water/DMF solvents on the structure of poly(carbon suboxide) | 96 |
| 5.5 Conclusion | 100 |

6 Structural analysis of nano-scaled aggregations derived from self-assembly of coil-ring-coil block copolymers **102**

| | |
|---------------------------------|-----|
| 6.1 Introduction | 102 |
| 6.2 Experimental | 107 |
| 6.3 SAXS results and discussion | 107 |
| 6.4 Conclusion | 112 |

| | |
|--|------------|
| 7 Summary/Zusammenfassung | 113 |
| References | 117 |
| Appendix | 123 |
| Appendix A Investigated samples of dissolved poly(carbon suboxide) | 123 |
| Appendix B Derivation of Eq. (2.22) | 124 |
| Publications | 125 |
| Erklärung | 126 |

1 Introduction and motivation

Small Angle X-ray Scattering (SAXS) has become a powerful technique in colloidal science for determining size, shape and internal structure of polymer particles in the size range from a few nanometers up to about 100 nm [Guinier & Fournet, 1955; Glatter & Kratky, 1982; Feigin & Svergun, 1987; Lindner & Zemb, 1991; Brumberger, 1995; Hunter, 1989]. With an improved Kratky-camera [Dingenouts, 1998] the measurable size even approaches to 200 nm [Dingenouts, 1998; 1999]. SAXS is mainly applied to systems of randomly oriented and statistically distributed structures of colloidal dimensions, such as latexes [e.g. Ballauff, 1996; Dingenouts, 1998; 1999], supramolecular aggregations (e.g. micelles [e.g. Kratky & Müller, 1982; Hickl, 1996]), proteins [Pilz, 1982], natural and synthetic high polymers dispersed in solutions [e.g. Kratky, 1982; Kirste & Oberthür, 1982; Hickl, 1997; Kholodenko, 1998; Dingenouts, 1998] or precipitates in amorphous materials [e.g. Bergmann, 2000; Bolze, 2002; 2004].

Apart from the structural analysis of single particles, the spatial and orientational arrangement of particles in colloidal suspensions which is determined by the interaction between the particles and by their form and symmetry can also be studied by SAXS. Colloidal suspensions of monodisperse or narrowly distributed spheres, which have a relatively simple equilibrium phase diagram determined by the volume fraction and the ionic strength, have been well understood after intensive investigations [e.g. Pusey, 1991; Vrij, 1979; Hayter, 1981; Hayter and Hansen, 1982; Grunder, 1993]. However, for anisotropic particles such as cylinders and disks, which have an additional degree of freedom-the orientation, our knowledge is limited and thus they become an area of much current interest [e.g., de Gennes and Prost, 1993; Veerman and Frenkel, 1992].

The motivation of this thesis is to analyze by SAXS the structure and mutual interactions of three nano-scaled particles: anisotropic disc-shaped (or cylindrical) Laponite particles, polymer carbon suboxides with pre-unknown structure and shape persistent supramolecular aggregates formed by coil-ring-coil block copolymers. All of them can be classified as

cylindrical particles. The general goal is to improve our understanding on this kind of anisotropic geometry by SAXS.

Since the commercial available synthetic colloidal clay, Laponite [www.laponite.com] shows unique disk shape in aqueous solutions, it is chose as ideal model systems to analyze anisotropic particles by SAXS in this work. Laponite particles are reported as disc-shaped particles with radius of about 15 nm and thickness of 1 nm, and more interestingly, suspensions of these charged colloidal discs are observed to undergo a transition from a fluid-like sol to a solid-like gel, instead of entering a liquid-crystalline phase [Ramsay, 1986; Avery and Ramsay, 1986; Rosta and von Gunten, 1990; Thompson and Butterworth, 1992; Mourchid, 1995; Pignon, 1997; Kroon, 1996; Willenbacher, 1996]. This interesting phenomenon has attracted many theoretical investigations, among them, the “house of cards” structure [Dijkstra, Hansen and Madden, 1997] is well known, which originates from the quadrupolar disc model, and their Monte Carlo simulations point to a reversible sol-gel transition. However, this is an oversimplified model, and the status and the origin of the sol-gel transition are still a matter of controversy. Recently, the PRISM (“polymer reference interaction site model”), originally designed for the study of polymer solutions and melts [Schweizer, 1997], has been extended to investigate monodisperse [Harnau et al., 2001] and bidisperse [Harnau et al., 2002] platelet suspensions.

Although Laponite has received relatively intensive investigations, the experimental results and their theoretical models are full of controversy, even contradictory. The present work aims to clarify the fact by combining SAXS (synchrotron radiation combined with a Kratky-Camera) and static light scattering measurements to analyze Laponite particles in dilute aqueous solutions. The combination of scattering techniques probes more than three orders of magnitude in the scattering vector q . This allows us to investigate the state of Laponite dispersions from sub-particle length scale to the large length scale of particles arrangement. Beyond this, the structure factor $S(q)$, which relates to the interparticle interference, can be experimentally determined as function of scattering vector q and volume fraction ϕ , and be compared with the newly developed PRISM model for anisotropic objects.

Moreover, SAXS techniques can be employed to determine pre-unknown structures of colloidal systems and provide information on the chemical construction of investigated particles. Polymer carbon suboxide ($(C_3O_2)_n$) was found in the beginning of last century

[Diels, 1906], but its chemical structure, polymerization degree as well as chain conformation in solvents have not yet been well characterized up to now [e.g. Ziegler, 1960; Blake, 1964; Snow, 1978; Yang, 1981]. For the first time, we have applied SAXS successfully to determine the chemical structure, polymerization degree and chain conformation in solutions of polymer carbon suboxides. At first, with help of Guinier-law, the molecular weight and radius of gyration of dissolved polymer chains can be obtained from the absolute scale of form factor of the dissolved polymer chains without any prior assumption. Then, by comparing the experimental scattering intensity with several well-established model functions, the conformation of the dissolved polymer chains can be determined. At last, size parameters of polymer chains obtained from SAXS are related directly to the chemical structure and one structure proposed in literature could therefore be confirmed.

SAXS is also suitable for analysis of supramolecular aggregates (such as micelles or self-assembling systems) and the origin of aggregating, i.e., inter-molecular forces, which hold small molecules together and arise from weak van der Waals, hydrophobic, hydrogen-bonding and screened electrostatic interactions [Israelachvili, 1985], especially for determination of the internal structures of aggregates, e.g., the (in)homogeneity (distribution of electron density) inside micelles. Recently, Höger et al. have synthesized several shape-persistent macrocycles which can be used as template molecules to form special shaped supramolecular structures in suitable solvents [Höger, 2004]. In this work, one kind of supramolecular structure derived from self-assembly of coil-ring-coil block copolymers with oligostyrene side chains (M_w (PS) = 2500 g/mol), was determined by SAXS. The used solvent is cyclohexane which is a θ -solvent for PS, but a non-solvent for the rigid core. The difference of solubility between rigid ring and soft coil attributes to the self-assembling structure [Höger, 2004], and the ring-coil block copolymer behaves like amphiphilic molecules in this case. The determination of structural information of the supramolecular aggregates by SAXS is very helpful for understanding the formation of supramolecular aggregates as well as the relationship between structure and properties.

2 Theory of SAXS

2.1 Introduction

Small angle scattering techniques, including small angle X-ray scattering (SAXS) and small angle neutron scattering (SANS), are capable to give information on the structural features of particles of colloidal size as well as their spatial correlation. Hence, they are very suitable for a comprehensive analysis of colloidal particles.

The physical principles of SAXS, SANS and static light scattering (SLS) are the same [Schmidt, 1995]. The electric field of the incoming wave induces dipole oscillations in the atoms. The accelerated charges generate secondary waves that add at large distances (far field approach) to the overall scattering amplitude. All secondary waves have the same frequency but may have different phases caused by different path lengths.

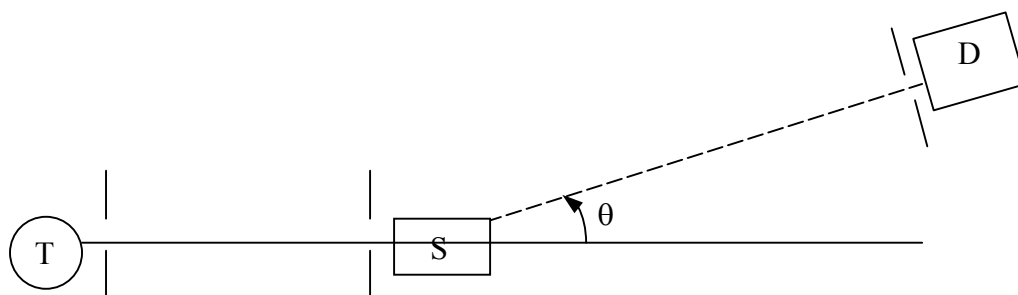


Fig. 2.1 The essential parts of a small angle scattering system. The drawing shows the X-ray source T , the sample S , the scattering angle θ , the slits used to define the incident and scattered beams, and the detector D .

A schematic description of scattering principle is shown in Fig. 2.1. X-ray or neutrons from the source T are formed into a fine beam, often by slits, and strike the samples S . A small fraction of this beam is scattered in other directions, e. g., in Fig. 2.1 an angle θ with the direction of the incoming beam. D is a detector, used to record the scattering intensity

(the square of the scattering amplitude) and its dependence on the scattering angle. Information about the structure of the sample can often be obtained from the analysis of the scattering intensity at a sequence of scattering angles. The procedure of data evaluation will be described in chapter 3 in detail.

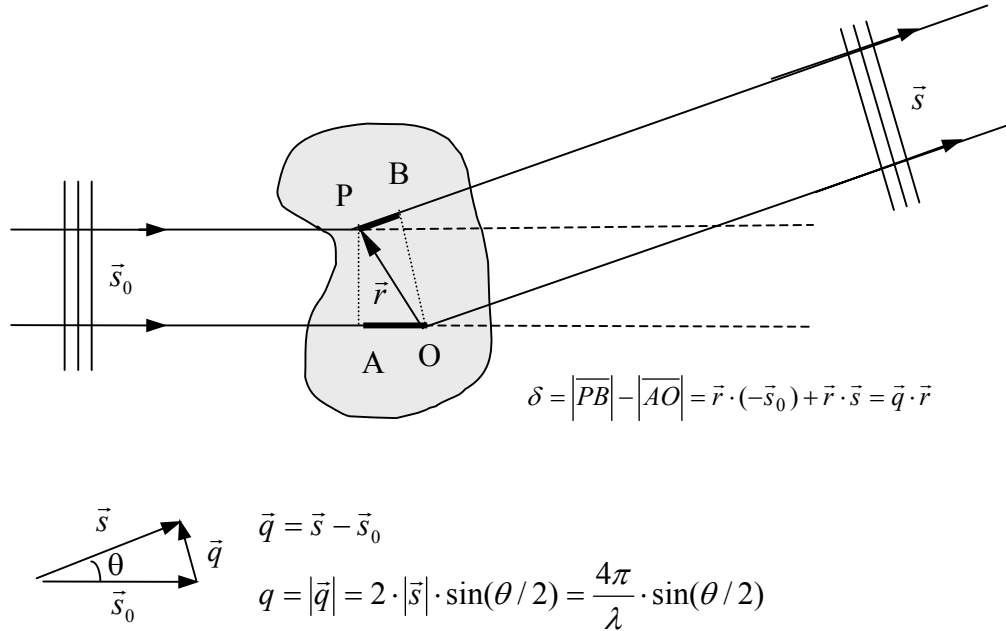


Fig. 2.2 Calculation of the phase difference δ between the waves from scatterers at points O and P in a particle. In the drawing, \vec{s} and \vec{s}_0 are unit vectors in the directions of scattered and incident beams, respectively, and P is displaced from O by the vector \vec{r} . θ denotes scattering angle and \vec{q} scattering vector.

Figure 2.2 illustrates how the phase difference δ between the waves from scatterers at point O and P in a particle can be calculated, where the angle between the incident and scattered beams is the scattering angle θ and the vector \vec{r} goes from point O to point P. The phase difference between the waves scattered by the two scatterers will be $\vec{q} \cdot \vec{r}$.

$$q = |\vec{q}| = \frac{4\pi}{\lambda} \sin(\theta/2) \quad (2.1)$$

where λ is the wave length; \vec{s} and \vec{s}_0 are unit vectors in the direction of the scattered and incident beams, respectively.

The angle-dependent scattering amplitude is related to the electron density distribution $\rho(\vec{r})$ of the scatterer by a Fourier transformation. $\rho(\vec{r})$ is the number of electrons per unit volume at the position \vec{r} . A volume element dV at \vec{r} contains $\rho(\vec{r})dV$ electrons. The scattering amplitude of the whole irradiated volume V is given by

$$A(\vec{q}) = A_e \cdot \int_V \rho(\vec{r}) e^{-i\vec{q}\vec{r}} d\vec{r} \quad (2.2)$$

where A_e denotes the scattering amplitude of one electron.

The scattering intensity of one single particle $I_0(\vec{q})$ is the absolute square given by the product of the amplitude and its complex conjugate $A(\vec{r})^*$

$$I_0(\vec{q}) = A(\vec{q}) \cdot A(\vec{q})^* = I_e \cdot \iint_{VV'} \rho(\vec{r}) \rho(\vec{r}') e^{-i\vec{q}(\vec{r}-\vec{r}')} d\vec{r} d\vec{r}' \quad (2.3)$$

The electron scattering intensity I_e has been given by the well known Thomson formula [e.g., von Laue, 1960]:

$$I_e(\theta) = I_p \cdot 7.9 \cdot 10^{-26} \cdot \frac{1}{d^2} \cdot \frac{1 + \cos^2 \theta}{2} \quad (2.4)$$

where I_p denotes the primary intensity and d the distance between sample and detector. The numerical factor is the square of the so-called classical electron radius. The intensity depends only slightly on the scattering angle θ by the polarization factor, which is practically equal to 1 for the small angles in all problems of interest here. As the electron scattering intensity I_e applies to all formulae to follow, it will be omitted for brevity, i.e., the SAXS scattering intensity is expressed in units of the scattering intensity of a single electron (e.u., electron units).

So far as we discussed is the scattering process of a particle in fixed orientation in vacuum. In most cases of SAXS the following situations are given:

- The particles are statistically isotropic and no long-range order exists, i.e., there is no correlation between particles at great spatial distances.

- The particles are embedded in a matrix. The matrix is considered to be a homogeneous medium with the electron density ρ_0 . This situation is given for particles in solution or for inhomogeneities in a solid. The electron density in equations (2.2 – 2.3) should be replaced by the difference in electron density $\Delta\rho = \rho - \rho_0$, which can take positive or negative value.

In this case the average over all orientations leads to the fundamental formula of Debye [Debye, 1915]

$$\langle e^{-i\vec{q}\vec{r}} \rangle_{\Omega} = \frac{\sin(qr)}{qr} \quad (2.5)$$

Thus, equation (2.3) reduces to the form

$$I_0(q) = 4\pi \int_0^{\infty} \gamma(r) \frac{\sin(qr)}{qr} r^2 dr \quad (2.6)$$

Eq. (2.6) is the most general formula for the scattering pattern of any systems, which obey the above two restrictions. $\gamma(r)$ is the so-called *correlation function* [Debye & Bueche, 1949], or *characteristic function* [Porod, 1951]. It can be obtained by the inverse Fourier transform with

$$\gamma(r) = \frac{1}{2\pi^2} \int_0^{\infty} I_0(q) q^2 \frac{\sin(qr)}{qr} dq \quad (2.7)$$

For $q = 0$ and $r = 0$, as the Debye factor equals to unity, eq. (2.6) and (2.7) reduce to

$$I_0(0) = \int_0^{\infty} 4\pi r^2 \gamma(r) dr \quad (2.8)$$

$$\gamma(0) = \frac{1}{2\pi^2} \int_0^{\infty} I(q) q^2 dq = V_p \overline{(\Delta\rho)^2} \quad (2.9)$$

For eq. (2.8), at $q = 0$ exactly, all secondary waves are in phase, so that $I_0(0)$ may be expected to be equal to the square of the total number of electrons in the irradiated volume V_P (volume of one single particle). However, this quantity is experimentally not available. So, it should be regarded as an extrapolated value through Guinier approximation or Zimm plot, which will be discussed in the next section.

Equation (2.9) shows that the integral of the intensity over all the reciprocal space is directly related to the mean square fluctuation of excess electron density, irrespective of special features of the structure. From this point an important quantity “invariant” Q is produced as

$$Q = \int_0^{\infty} I_0(q) q^2 dq = 2\pi^2 V_P \overline{(\Delta\rho)^2} \quad (2.10)$$

which plays an important role in analysis of the scattering pattern of some deformed particles.

Guinier's Law and radius of Gyration:

At low q region, i.e., for $qr \ll 1$ the Debye factor $\sin(qr)/(qr) \cong 1 - (qr)^2/3! + \dots$, eq. (2.6) reduces to [Guinier, 1939]

$$I_0(q) = 4\pi \int \gamma(r) \left(1 - \frac{(qr)^2}{6} + \dots\right) r^2 dr \cong I_0(0) \left(1 - \frac{q^2 R_g^2}{3}\right) \quad (2.11)$$

where R_g is the radius of gyration given by

$$R_g^2 = \frac{\frac{1}{2} \int \gamma(r) r^4 dr}{\int \gamma(r) r^2 dr} \quad (2.12)$$

which is related to the electron density $\rho(\vec{r})$ of the particle, can also be represented as

$$R_g^2 = \frac{\int \rho(\vec{s}) s^2 d\vec{s}}{\int \rho(\vec{s}) d\vec{s}} \quad (2.13)$$

with defining \vec{s} as the vector taken from the center of gravity of $\rho(\vec{r})$.

For homogeneous particles, the radius of gyration is only related to the geometrical parameters of simple triaxial bodies [Mittelbach, 1964], e.g., $R_g = \sqrt{3/5} \cdot R$ for spheres with radius R ; $R_g = [R^2/2 + H^2/12]^{1/2}$ for cylindrical particles with length H and radius R in cross-section.

Because of $e^{-x} \cong 1-x$, for $qr \ll 1$ eq. (2.11) can be also expressed as

$$I_0(q) \cong I_0(0) \exp\left[-\frac{R_g^2 q^2}{3}\right] \quad (2.14)$$

This is the so-called *Guinier's law*, which is a most useful relation in SAXS analysis since it allows to obtain R_g^2 and $I_0(0)$ from scattering data in the region of smallest angles without any prior assumption on the shape and internal structure of the particles under investigation.

2.2 Scattering functions of single cylindrical particles

Since the interpretation of scattering pattern of nano-scaled cylindrical particles is the objective of the present work, the scattering function of a single particle with cylindrical shape will be considered here in detail.

In general, the form factor of randomly oriented cylindrical particles (homogeneous inside) with any ratio of cross-section radius R to the length H has been given by [Guinier & Fournet, 1955]

$$P(q) = 4 \cdot \int_0^1 \frac{J_1^2[qR(1-x^2)^{1/2}]}{[qR(1-x^2)^{1/2}]^2} \cdot \frac{\sin^2(qHx/2)}{(qHx/2)^2} dx \quad (2.15)$$

where J_1 denotes the Bessel function of first order. Specially, for very long-stretched ($H \gg R$) or very flat particles ($R \gg H$) their scattering patterns show some peculiar features, i.e., scaling laws [e.g., Feigin & Svergun, 1987], which will be discussed respectively. The scattering intensity of a polymer chain, being of some common characteristic of cylindrical particles, will be considered also in this section.

2.2.1 Long rods

We consider at first a long rod with length H ($H \gg R$) and cross-section A , which has a columnar structure, i.e., a structure where the density distribution in cross-section A does not depend on the axis of H . As shown in Fig. 2.3, the vector \vec{r} has components: $\vec{r} = \vec{z} + \vec{r}_C$, so the three-dimensional intensity can be separated into two factors belonging to H and A , respectively.

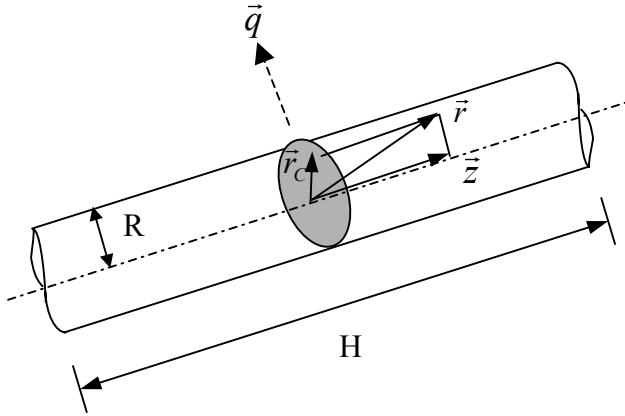


Fig. 2.3 Schematic description of the vectors in a rod-like particle with length of H and radius R in cross-section.

The scattering amplitude of eq. (2.15) in this case may be expressed as [Guinier and Fournet, 1955]

$$F(q) = \Delta\rho \cdot H \cdot \underbrace{\frac{\sin(qH\gamma/2)}{qH\gamma/2}}_{F_H} \cdot \underbrace{\iint dA \cdot e^{-i\vec{q}\vec{r}_C}}_{F_C} \quad (2.16)$$

where $\gamma = \cos\alpha$, α being the angle between the scattering vector q and the z axis in reciprocal space.

The length factor F_H is given by

$$I_H(q) = \langle F_H^2 \rangle = H^2 \int_0^1 \frac{\sin^2(qH\gamma/2)}{(qH\gamma/2)^2} d\gamma \cong H \frac{\pi}{q} \quad \text{for } qH > 2\pi \quad (2.17)$$

The remaining factor F_C , when squared and averaged, gives a function of $I_C(q)$, which is related only to the cross-section.

$$I_C(q) = \langle F_C^2 \rangle = (\Delta\rho)^2 \cdot \iiint dA_1 dA_2 \cdot e^{-i\vec{q}\vec{r}_c} \quad (2.18)$$

Since the variation is in two dimensions,

$$\langle e^{-i\vec{q}\vec{r}_c} \rangle = J_0(qr_c) \quad (2.19)$$

With the help of power series $J_0(qr) = 1 - q^2 r^2 / 4 \dots$, eq. (2.18) can be rewritten as an approximate form for $qR_C < 1$,

$$I_C(q) \cong (\Delta\rho)^2 A^2 \cdot \exp\left[-\frac{1}{2} R_C^2 q^2\right] \quad \text{for } qR_C < 1 \quad (2.20)$$

where A denotes the cross section of the rod-like particle. The radius of gyration R_C is defined in the same way as R_g , but for the cross-section only. For a circular rod, for example, $R_C = R/\sqrt{2}$.

Then the scattering intensity of a long rod with length H and radius of gyration R_C in cross-section has the following form

$$I_0(q) = I_H(q) \cdot I_C(q) \cong H \cdot \frac{\pi}{q} \cdot (\Delta\rho)^2 \cdot A^2 \cdot \exp\left[-\frac{1}{2} R_C^2 q^2\right] \quad (2.21)$$

The factor $1/q$ is characteristic of rod-like particles. Except of the factor of $I_C(q)$, scattering intensity of rod-like particles multiplied by q shows no dependence on q at high q region.

Therefore, if a system with volume V has N_P identical dissolved rod-like particles (length H , radius of gyration in cross-section R_C), the scattering intensity of this system at $2\pi/H < q < 1/R_C$ may be expressed as eq. (2.22) [cf. Appendix], provided that inter-particle interference is negligible.

$$I(q) = \frac{N_P}{V} \cdot I_0(q) \cong \frac{1}{q} \pi c K_{XS} M_L \exp\left[-\frac{1}{2} R_C^2 q^2\right] \quad \text{for } \frac{2\pi}{L} < q < \frac{1}{R_C} \quad (2.22)$$

where $M_L (= M_w/H)$ denotes the molecular weight per unit length of rod-like particles and c concentration of samples. K_{XS} is a contrast factor, defined for SAXS as

$$K_{XS} = N_A \cdot (\Delta z_2)^2 = N_A \cdot \left[\frac{n_e}{M_0} - \frac{\bar{v}_2 \cdot \rho_{0,e}}{N_A} \right]^2 \quad (2.23)$$

where N_A is the Avogadro constant, n_e and M_0 are electron number and molecular weight of repeat units of the polymer, respectively. $\rho_{0,e}$ is electronic density of the solvent and \bar{v}_2 the partial specific volume, which can be obtained from the density measurement of dispersed particles (see section 3.4).

Eq. (2.22) is very useful, as plots of $\ln[I(q)q]$ versus q^2 (cross-section Guinier plot [Brumberger, 1995]) allow to extract M_L and R_C from experimental data measured from rod-like systems. This is due to the fact that the application of eq. (2.22) to experiments does not require an entirely stiff rod but only a certain local stiffness. A slight bending of the rod does not impede the q^{-1} -dependence of the scattering function, i.e., an array of rods assembled at random will exhibit the typical q^{-1} -dependence of the scattering intensity if q is high enough [Glatter & Kratky, 1982]. This point is particular interest for macromolecules in solution, since all linear polymer chains can be treated as rod-like particles but with flexibility which will be discussed separately in the following section.

Fig. 2.4 gives a comparison of the form factor of a single rod with $L/(2R) = 10$ calculated by the exact form (2.15) and its approximation (2.22). The coincidence of the two curves occurs in the region of $\frac{2\pi}{L} < q < \frac{1}{R_C}$ (between two arrows in Fig. 2.4), where it is safe to evaluate experimental data by applying approximation (2.22).

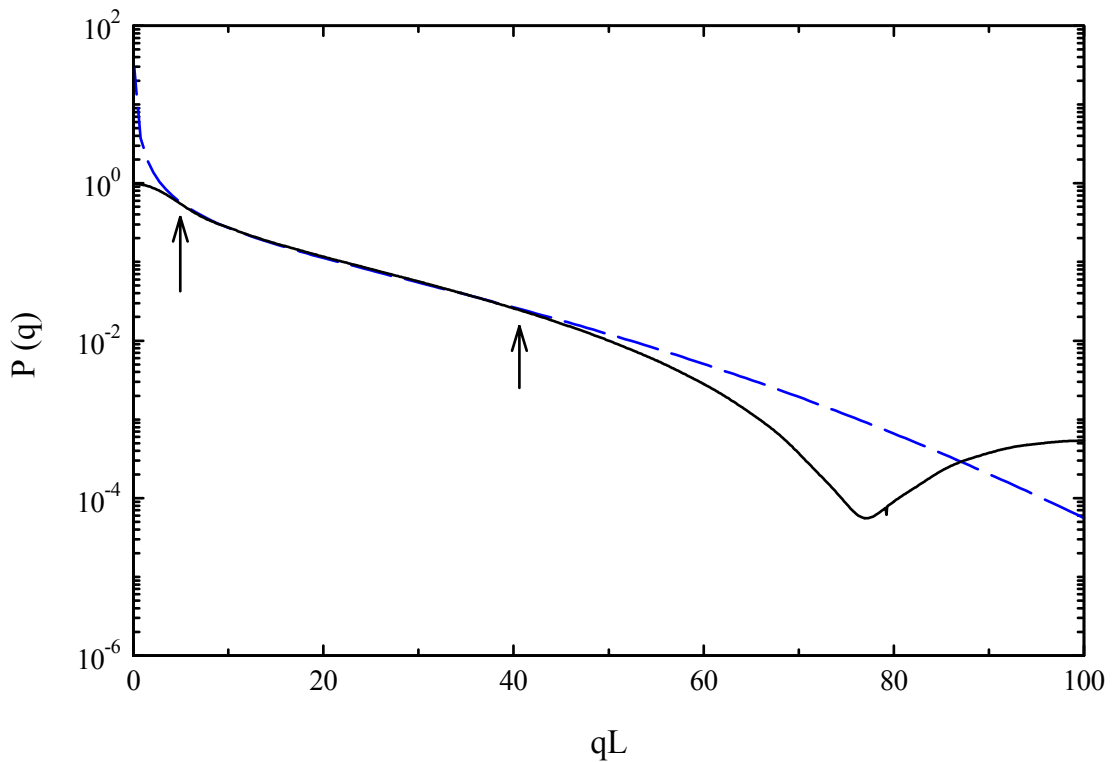


Fig. 2.4 Comparison of scattering intensity of a homogeneous rod with $L/2R = 10$ calculated by exact form (2.15) (solid line) and by approximation (2.22) (dashed line). Arrows indicate the valid region of q for the approximation (2.22).

2.2.2 Disc-shaped particles

In case of $R \gg H$, eq. (2.15) represents the scattering function of a thin platelet (as described in Fig. 2.5) which can be deduced in the same manner as in the case for long rods.

The scattering intensity $I_0(q)$ of the thin platelet may be expressed as [Guinier and Fournet, 1955]

$$I_0(q) = I_A \cdot I_T \cong A \frac{2\pi}{q^2} I_T(q) \quad (2.24)$$

where the first term relates to a very large plane of area A , and the second factor takes into account the interference along the surface normal. For homogeneous platelets $I_T(q)$ is given by

$$I_T(q) = (\Delta\rho)^2 H^2 \left[\frac{\sin(qH/2)}{qH/2} \right]^2 \quad (2.25)$$

After introducing a Guinier type approximation,

$$I_0(q) \cong A(\Delta\rho)^2 \frac{2\pi}{q^2} \exp[-R_T^2 q^2] \quad \text{for } qR_T < 1 \quad (2.26)$$

with $R_T = H/\sqrt{12}$. Thus, the thickness H of platelets can be extracted from plots of $\ln[I_0(q)q^2]$ versus q^2 for experimental data measured from platelet systems.

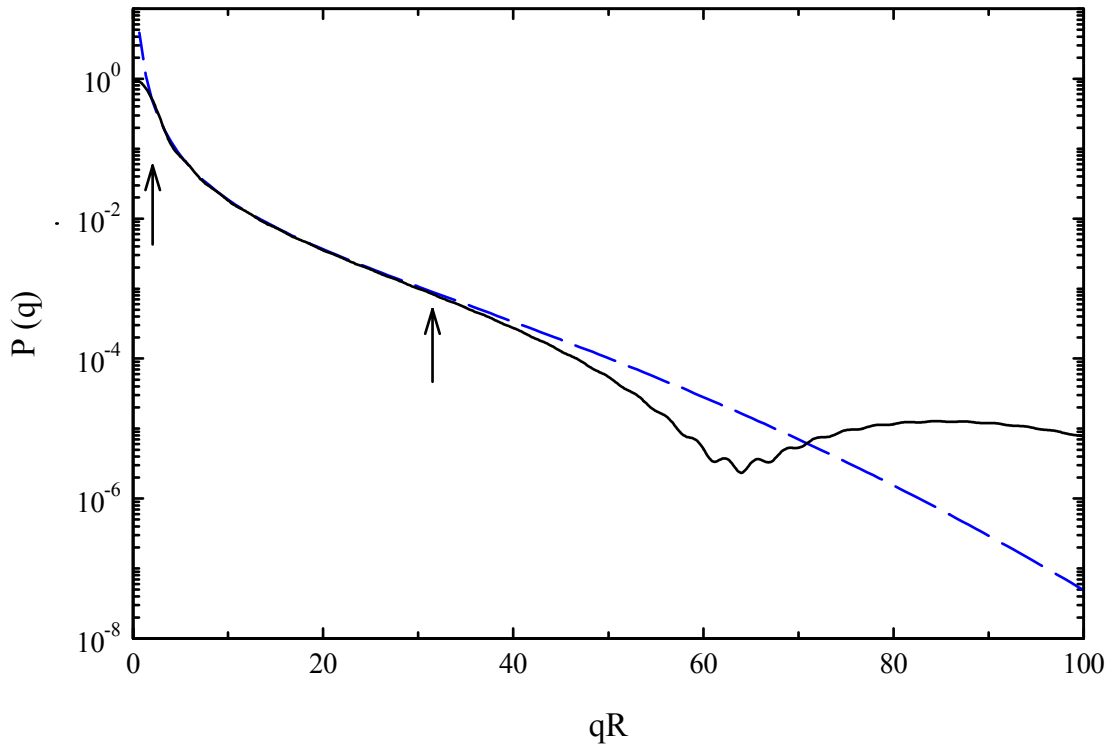


Fig. 2.6 Form factor of a homogeneous platelet of $R/H = 10$ calculated by exact form (2.15) (solid line) and by approximation (2.26) (dashed line). They coincide in the middle q region.

In the same way as for rod-like particles, the form factor of homogeneous platelets calculated by its exact form (2.15) and approximation (2.26) are compared in Fig. 2.6. The

approximate solution works well in middle qR region, as shown in Fig. 2.6 between the two arrows.

2.2.3 Polymer chains in solution

In this section the scattering function of polymer chains in dilute solutions is considered as cylindrical particles, since a local stiffness always exists for polymer chains, despite the entirely more or less flexibility of polymer chains. Here, the influence of the statistical chain conformation of single polymer chains on the scattering pattern will be discussed in detail.

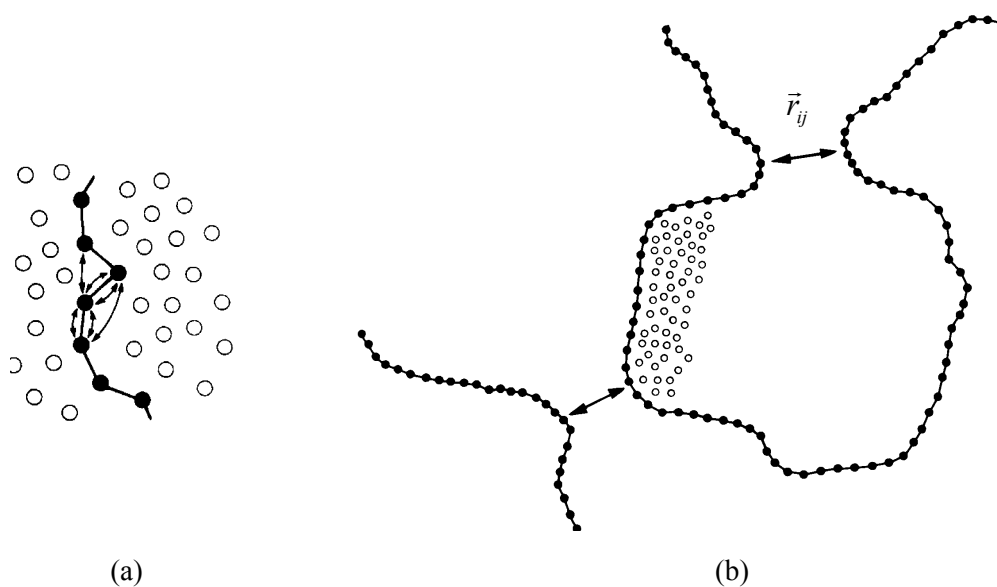


Fig. 2.7 Schematic description of the action of (a) short range (longitudinal) interactions and (b) long range (transversal) interactions in polymer solutions. Solvent molecules are presented by open circles.

A polymer chain may consist of N links, numbered from 1 to N , among which two arbitrary links i and j are considered, as described in Fig. 2.7. The form factor of this chain may be calculated according to the formula of Debye [1915] after averaging all of the interference terms

$$P(q) = \frac{1}{N^2} \cdot \sum_{i=1}^N \sum_{j=1}^N \left\langle \frac{\sin(q \cdot r_{ij})}{q \cdot r_{ij}} \right\rangle_{conf} \quad (2.27)$$

where N is the total number of scattering centers. If the distribution function $g(r_{ij})$ is known, with which the average of the interference term can be rewritten as

$$\left\langle \frac{\sin(q \cdot r_{ij})}{q \cdot r_{ij}} \right\rangle_{conf} = \int_0^{\infty} g(r_{ij}) \cdot \frac{\sin(qr_{ij})}{qr_{ij}} \cdot r_{ij}^2 \cdot dr_{ij} \quad (2.28)$$

To determine the distribution function $g(r_{ij})$ of polymer chains, we should consider at first the following two types of intersegmental interactions [Kirste and Oberthuer, 1982]:

- (1) Short range interactions which act along the chain from neighbor to neighbor, as described in Fig. 2.7 (a) by arrows. These interactions are due to bond forces and hindrance of rotation which are present in every polymer chain and only slightly affected by the solvent.
- (2) Long range interactions which act across the chain, being independent of the distance of interacted points, as described in Fig. 2.7 (b) by the arrow which exists inside of the polymer chain. The long range interactions are affected strongly by the solvent.

The simplest case is that the polymer chains dissolved in such a solution that a second virial coefficient $A_2 = 0$ (theta condition), i.e., the repulsion is compensated by attractive interactions. In this case the long range interactions are neglected and the polymer chain behaves like an unperturbed chain, and is named *Gaussian chain*, because all its intersegmental distances exhibit a Gaussian distribution. For this distribution the integral of eq. (2.28) can be solved analytically and it yields

$$\left\langle \frac{\sin(q \cdot r_{ij})}{q \cdot r_{ij}} \right\rangle_{conf} = \exp \left[-\frac{q^2 \cdot \langle r_{ij}^2 \rangle}{6} \right] \quad (2.29)$$

Eq. (2.27) was calculated by Debye [1947] for Gaussian chains with the result

$$P(q) = \frac{2(e^{-x} + x - 1)}{x^2}, \quad \text{with } x = R_g^2 \cdot q^2 \quad (2.30)$$

A characteristic feature of function (2.30) is its asymptotic behavior for high q

$$P(q) \underset{q \rightarrow \infty}{\propto} q^{-2} \quad (2.31)$$

The mean square of radius of gyration R_g^2 is decided by the number of links N and the segmental length l_0 as following form

$$R_g^2 = \frac{Nl_0^2}{6} \quad (2.32)$$

The segmental length l_0 can be substituted by the Kuhn length b in the Kuhn-model [Kuhn, 1934], where with such a statistical chain element b ($b \geq l_0$) that the bonding angle and angle of rotation can change freely, i.e., in a way of “random walking”, any chains can be treated as Gaussian chains.

2.2.4 Semi-flexible chains

For polymer chains, which can not be treated as a Gaussian chain (or Kuhn chain) due to the number of Kuhn-segment N_K is too small or Kuhn length b is too big (stiff chain), the above described form factor does not work any more. To overcome these restrictions in the interpretation of the scattering function of such semi-flexible polymer chains, a model chain, the so-called *Kratky-Porod chain* (KP-chain, worm-like chain, persistence chain) is developed by Kratky and Porod [1949]. Fig 2.8 described schematically a Kratky-Porod chain with 3 Kuhn-segments b .

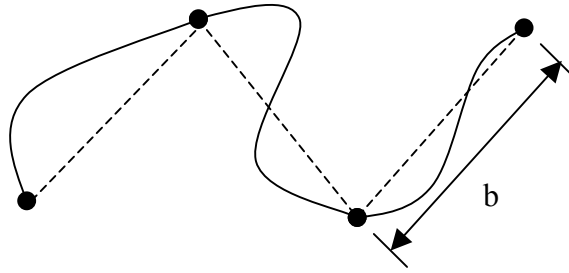


Fig. 2.8 Schematic description of one part of a persistence chain with 3 Kuhn-segments b .

In this model, the stiffness of the polymer chain is characterized by the persistence length a which is defined as the average sum of the projections of all bonds i ($i \rightarrow \infty$) on the direction of the first bond and has the following relationship with Kuhn length in the limit of the infinitely long molecules ($L/b \rightarrow \infty$) [Benoit and Doty, 1953; Doi and Edwards, 1986; de Gennes, 1979]:

$$b = 2a \quad (2.33)$$

L ($= N_K b$, where N_K is the number of Kuhn units in the chain) is the contour length of polymer chains. The radius of gyration of a KP-chain can be approximated by the persistence and contour length with [Benoit and Doty, 1953]:

$$R_g^2 = \frac{aL}{3} - a^2 + \frac{2a^3}{L} - \frac{2a^4(1 - e^{-\frac{L}{a}})}{L^2} \quad (2.34)$$

The problem to solve the scattering function of eq. (2.27) for Kratky-Porod chains lies in the factor that the distribution function $g(q)$ in this case can not be described exactly. There are two ways to solve the problem: one is the Monte Carlo simulation which was used to calculate the scattering function of polymer coils by Peterlin for the first time [Peterlin, 1960]; The other method is the analytical approach, which has been recently summarized by Pötschke et al. [Pötschke, 2000] and compared with the result of Monte Carlo simulations. According to their comparison, the analytical expression (2.35) from Kholodenko

[Kholodenko, 1993] is one of the best descriptions of the scattering function of semi-flexible chains with arbitrary stiffness a (persistence length) and contour length L :

$$P(q) = \frac{2}{x} \left[I_{(1)}(x) - \frac{1}{x} I_{(2)}(x) \right] \quad (2.35)$$

where $I_{(n)}(x) = \int_0^x f(z) z^{n-1} dz$, $n = 1, 2$; $x = 3L/2a$

together with

$$f(z) = \frac{1}{E} \frac{\sinh(Ez)}{\sinh(z)}; \quad q \leq \frac{3}{2a}$$

$$f(z) = \frac{1}{E} \frac{\sin(\hat{E}z)}{\sinh(z)}; \quad q > \frac{3}{2a}$$

and

$$E = \left[1 - \left(\frac{2}{3} aq \right)^2 \right]^{1/2}; \quad \hat{E} = \left[\left(\frac{2}{3} aq \right)^2 - 1 \right]^{1/2}$$

As expected, the form factor given above reproduces correctly the rigid-rod limit and the random-coil limit, i.e., for high q it gives out the expected form

$$P(q) \cong C_\infty (q^2 R_g^2)^{-1/2\nu}; \quad \text{for rigid rods } C_\infty = \pi/\sqrt{12}, \nu = 1 \text{ and } R_g^2 = L^2/12 \quad (2.36)$$

$$\text{for random-coils } C_\infty = 2, \nu = 1/2 \text{ and } R_g^2 = 2aL/6$$

The scattering function of such a chain should approach the scattering of a Gaussian chain (eq. (2.30)) for $q \rightarrow 0$ and $L \rightarrow \infty$, and approach the scattering of an infinitely thin rod for $q \rightarrow \infty$. Fig. 2.9 compares the scattering functions of a Kratky-Porod chain with intermediate stiffness ($L/b = 10$) calculated by Kholodenko's approximation (2.35) and Debye approximation for a Gaussian coil (2.30) in a Holzer presentation, i.e., $P(q)qL$ versus q , respectively. They are compared also with the scattering function of a needle. At low q ($< 1 \text{ nm}^{-1}$) they coincide, however, they deviate from each other due to the different model descriptions when q increases. At high q the Kholodenko's approximation (solid line) obeys

a q^{-1} -decay, whose tail tends to approach the scattering function of a needle (short dashed line), whereas the Debye approximation allows a q^{-2} -decay (long dashed line).

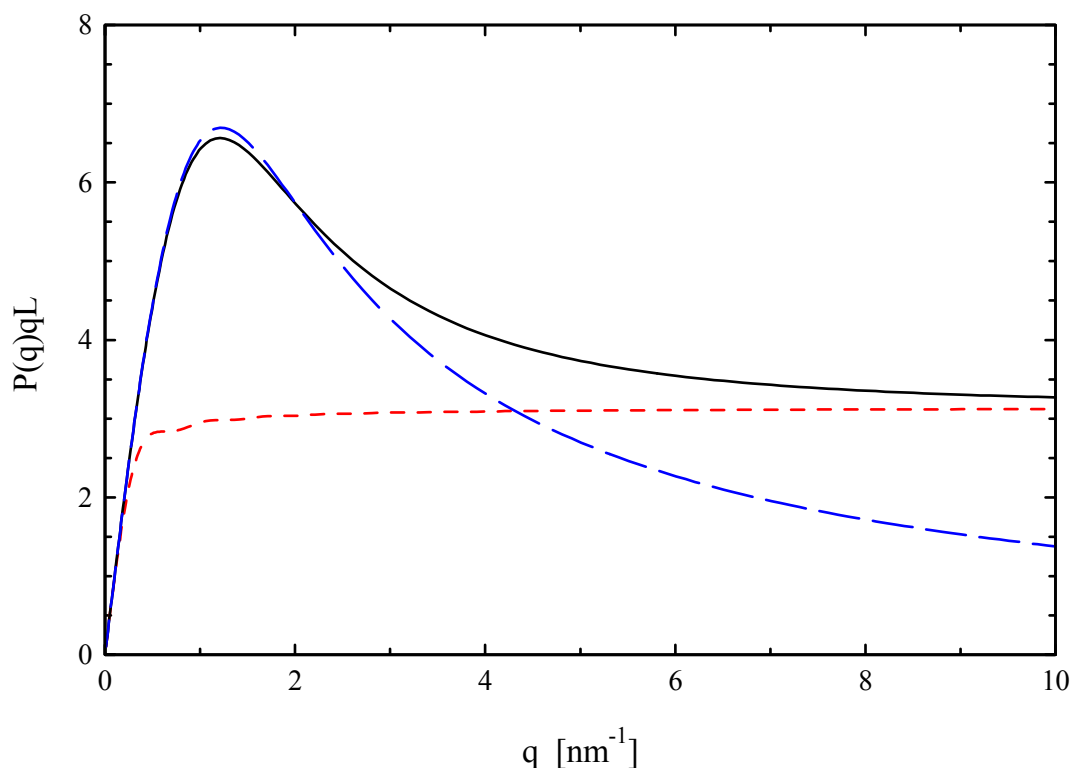


Fig. 2.9 Comparison of the scattering function of a Kratky-Porod chain of intermediate stiffness ($L/b = 10$) using Kholodenko's approximation (solid line) and Debye approximation for a Gaussian coil (long dashed line). The short dashed line represents the scattering function of an infinitely thin rod (needle) with $L = 10$ nm. The scattering function is plotted in a Holzer presentation of $P(q)qL$ versus q .

Above all, the scattering function of a polymer chain in different region of q can be related schematically to the spatial resolution, as shown in Fig. 2.10:

- (1) For low q region ($q < 1/R_g$), the scattering studies polymer chains as a total object, in this case structural parameters, e.g., size and molecular weight can be resulted. The scattering intensity obeys Guinier-law [Guinier, 1939].
- (2) For intermediate q region ($1/R_g < q < 1/b$), the scattering studies the flexibility of polymer chains which can be described by the universal scaling law of de Gennes

[de Gennes, 1979] ($P(q) \propto q^{-\frac{1}{\nu}}$, with $1/\nu$ changing continually from 2 (Gaussian chains) to 1 (rods)).

- (3) For high q region ($q > 1/b$), the local property of polymer chains is studied by scattering methods, in this scale the scattering “observes” a rigid rod, so the scattering intensity follows a q^{-1} decay.

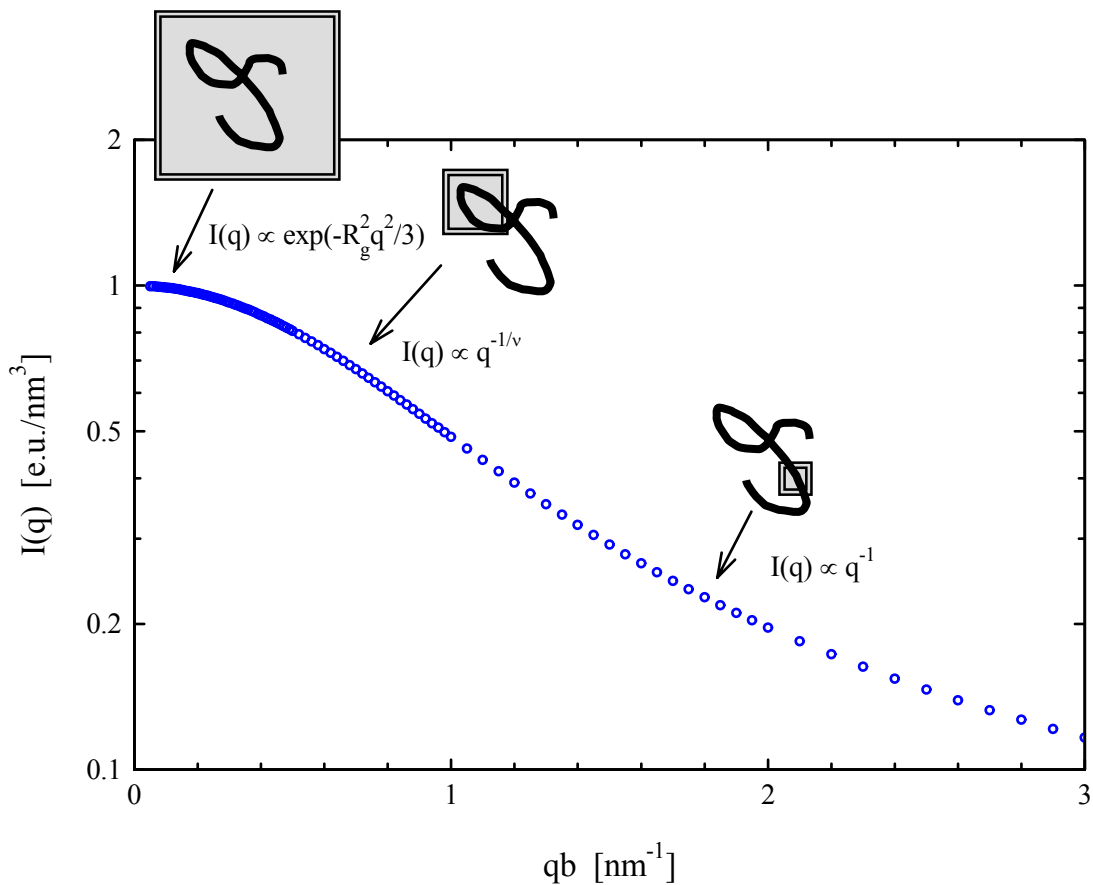


Fig. 2.10 Scaling laws of scattering function of a persistence chain with Kuhn length of b , corresponding to its valid q regions, which is schematically related to the spatial resolution.

So far, polymer chains have been treated as infinitely thin thread. It can be a good approximation if the spatial scale is much larger than the size of a monomer [Rawiso et al., 1987]. However, on a local scale, it is expected to be wrong because the monomer is no longer a point scatterer.

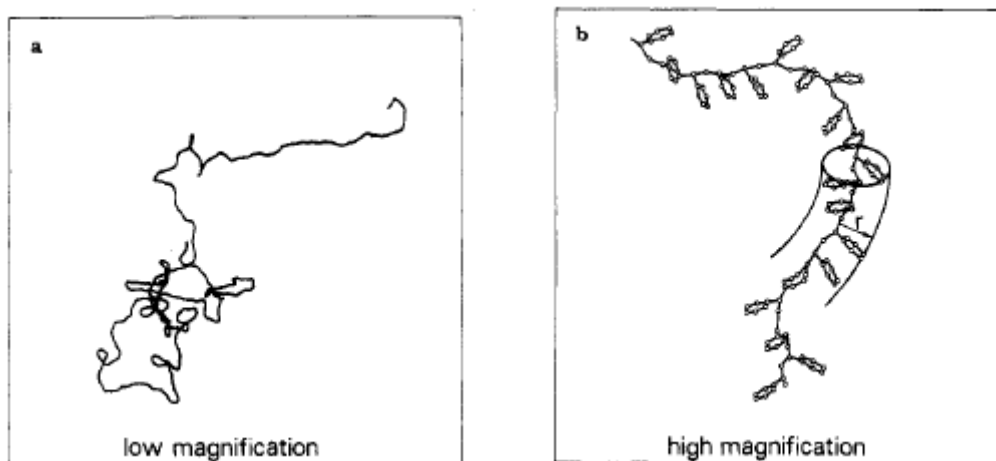


Fig. 2.11 Two resolutions of the structure of polystyrene [Rawiso et al., 1987]: (a) Spatial scale much larger than the size of the phenyl rings, the chain can be therefore represented by a smooth curve in space; (b) Local scale: the cross section of the chain is no longer negligible, and the structure of the chain can be approximated by a circle cylinder with radius of 0.4 nm.

As an example, Fig. 2.11 represents the structure of polystyrene in two spatial resolutions [Rawiso et al., 1987]. In Fig. 2.11 (a) the spatial scale is much larger than the size of the phenyl rings, the chain can be therefore represented by a smooth curve in space; however, on the local scale of Fig. 2.11 (b), the cross section of the chain is no longer negligible, and the structure of the chain can be approximated by a circle cylinder with radius of 0.4 nm.

If $\Delta\rho (= \rho - \rho_0)$ in cross section is assumed to be independent of the position along the polymer chain, the scattering function of a polymer chain can be factorized into two terms which correspond to the scattering contribution of a infinitely thin thread ($I_{0,\infty}(q)$) and a cross section part ($I_C(q)$), respectively [Kratky, 1956; Luzzati, 1960; Koyama, 1974; Glatter and Kratky, 1982]:

$$I_0(q) = I_{0,\infty}(q) \cdot I_C(q) \quad (2.37)$$

For $qR_C < 1$, the cross section term can be replaced by an exponential term, the so-called Guinier approximation, and the scattering function of a chain is

$$I_0(q) = I_{0,\infty}(q) \cdot \exp(-q^2 R_C^2 / 2) \quad (2.38)$$

where R_C^2 is the mean square radius of gyration in cross section and defined as

$$R_C^2 = \frac{\int_0^\infty \bar{r}^2 \Delta\rho(\bar{r}) d\bar{r}}{\int_0^\infty \Delta\rho(\bar{r}) d\bar{r}} \quad (2.39)$$

Fig. 2.12 displays the effect of a cross section on the scattering function of a persistence chain with intermediate stiffness ($L/b = 10$) in a Holzer presentation, i.e., $P(q)qL$ versus qb . The solid line with $R_C = 0$ differs strongly from the dashed line with $R_C = b/10$ and dot-dashed line with $R_C = b/5$, with increasing of the spatial resolution. So the introduction of the cross section term can change drastically the scattering function of persistence chains from $qb > 1$.

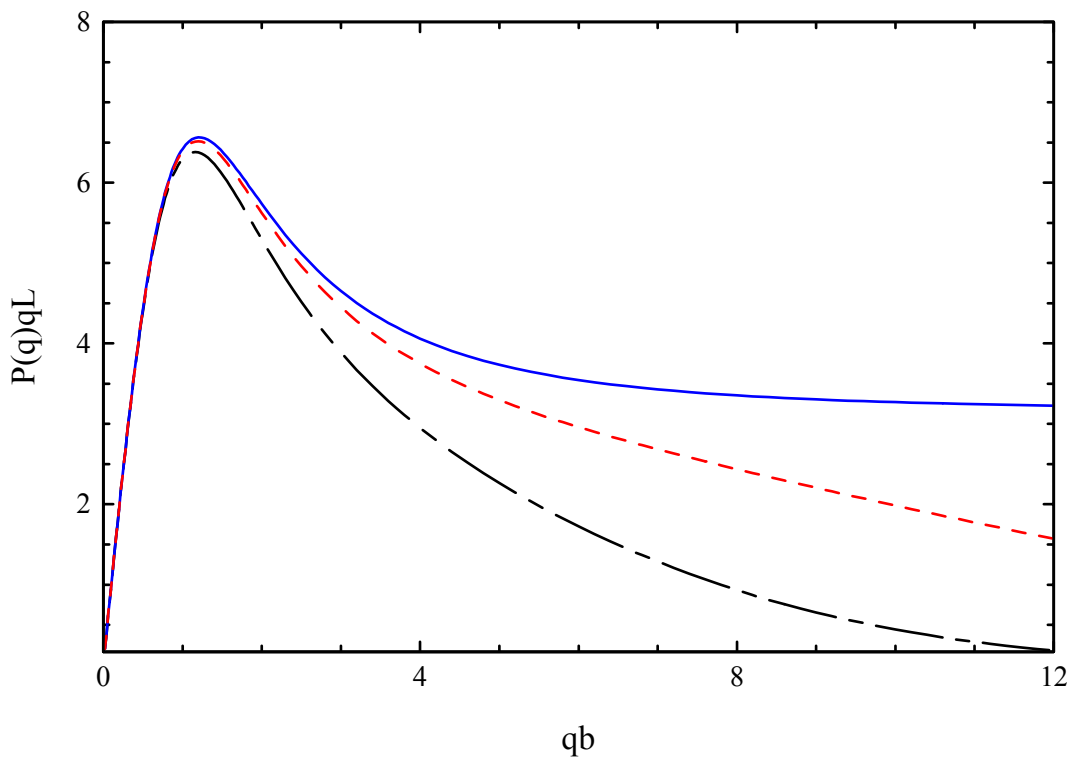


Fig. 2.12 Effect of a cross section on the scattering intensity of a persistence chain with intermediate stiffness ($L/b = 10$) in a Holzer presentation, $P(q)qL$ versus qb : (—) $R_C = 0$, (---) $R_C = b/10$, and (-·-·) $R_C = b/5$.

2.3 Interparticle Interference; Structure factor

So far, the main consideration is focused on the scattering of single particles. Actually, any investigated systems include a great number of particles. For a dilute solution it is assumed that the intensities are simply added to give the total diffraction pattern, but with increasing concentration the interparticle interference effects should be expected, which is another main subject of this work.

This interference comes from two sources: pure geometric influence (impenetrability of the particles) and electrostatic Coulomb interaction. In this chapter these two kinds of interactions will be discussed at first for identical particles with spherical symmetry, then the originated theory will be applied to polydisperse lamellar colloidal system, namely the multicomponent interaction site model, which has been developed by Harnau et al. [2001].

2.3.1 Systems of identical particles

The simplest case is a system of volume V , containing N identical particles. The scattering intensity in this case includes two terms: at first, because of the identity of particles, $I_0(q)$ of the single sphere can be taken as a common factor (intraparticle interference); secondly, an interparticle interference term must be formed to cover all possible arrangements, which is usually represented by structure factor $S(q)$:

$$I(q) = \frac{N}{V} \cdot I_0(q) \cdot S(q) = \frac{N}{V} \cdot \Delta n_e^2 \cdot P(q) \cdot S(q) \quad (2.40)$$

where $P(q)$ is the so-called form factor, corresponding to the scattering intensity of one single particle, but normalized to the number of excess electrons of one particle

$$P(q) = \frac{I_0(q)}{I_0(0)} = \frac{I_0(q)}{\Delta n_e^2} \quad (2.41)$$

As the same derivation procedure for eq. (2.22) in appendix B, eq. (2.40) may be expressed as

$$I(q) = c \cdot K \cdot M_w \cdot P(q) \cdot S(q) \quad (2.42)$$

Eq. (2.42) is a universal function for the scattering intensity of systems containing identical particles, where c [g/l] denotes the weight concentration of solutions and K the contrast factor, defined above as eq. (2.23).

Specially, for a system containing identical spheres (radius R), the interparticle interference term-structure factor $S(q)$ has been given by Guinier and Fournet [1955]

$$S(q) = 1 + \overline{\sum_k \sum_{j \neq k} \cos[\vec{q} \cdot \vec{r}_{jk}]} \quad (2.43)$$

with j, k represent scattering centers in different particles. In order to calculate the structure factor, a radial distribution function, or the so called pair correlation function $g(r)$ should be introduced at first [e.g. Zernicke & Prins, 1927; Hansen and McDonald, 1976].

On average each sphere has the same surrounding, so it will be suffice to regard only one central particle, and to render the possibility that another will be found in the volume element dV at a distance r apart, as shown in fig. 2.13. The mean value of this probability is $(N/V)dV$, any deviation from this may be accounted for by a factor $g(r)$. It is obvious that for $r < 2R$, $g(r) = 0$; and for $r \gg 2R$, $g(r) = 1$. So only the difference $(g(r) - 1)$ is relevant for diffraction.

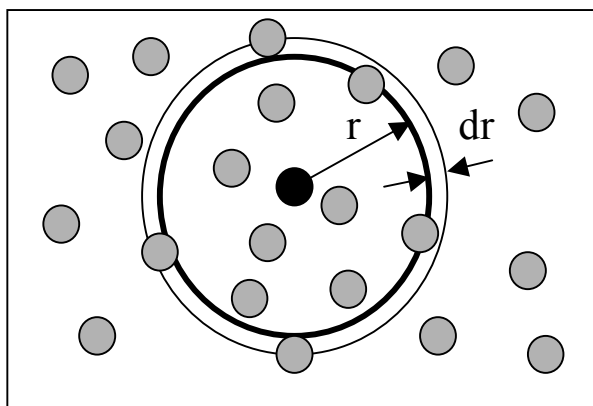


Fig. 2.13 Pair correlation function $g(r)$: $4\pi r^2 \cdot g(r) \cdot dr$ is the possibility that another particle will be found in the volume element $dV (= 4\pi r^2 \cdot dr)$ at a distance r apart.

With help of the pair correlation function $g(r)$ the average term in eq. (2.43) can be treated for all possible positions of arrangement as follows [Guinier & Fournet, 1955]

$$\left\langle \overline{\sum_k \sum_{j \neq k} \cos[\vec{q}\vec{r}_{jk}]} \right\rangle_{Pos} = 4\pi \left(\frac{N}{V} \right)^2 \int_0^\infty g(r) \frac{\sin(qr)}{qr} r^2 dr \quad (2.44)$$

The structure factor then takes the classical form [Zernicke & Prins, 1927]

$$S(q) = 1 + 4\pi \frac{N}{V} \int_0^\infty (g(r) - 1) \frac{\sin(qr)}{qr} r^2 dr \quad (2.45)$$

We should note that most particles investigated by scattering methods are much bigger than the medium molecules, i.e., the medium is considered as no structure molecules for scattering methods. The pair correlation function $g(r)$ can then be calculated with help of the statistic mechanics, while the theory for simple liquids [Hansen & McDonald, 1976] can be applied to the colloidal systems. For sake of simplicity we only discuss the systems of hard spheres interacting through the hard sphere potential

$$\frac{U(r)}{k_B T} = \begin{cases} \infty & r < 2R \\ 0 & r \geq 2R \end{cases} \quad (2.46)$$

or a modified hard sphere potential-Yukawa type for charged hard spheres with consideration of the repulsive Coulomb interaction [Derjaguin and Landau, 1941; Verwey and Overbeek, 1948]

$$\frac{U(r)}{k_B T} = \begin{cases} \infty & r < 2R \\ \frac{Z_P^2 L_B e^{-\kappa(r-2R)}}{(1 + \kappa R)^2 r} & r \geq 2R \end{cases} \quad (2.47)$$

where $L_B [= e^2/(4\pi\epsilon\epsilon_0 k_B T)]$ is the Bjerrum length, $\kappa [= (4\pi L_B I)^{1/2}]$ is the inverse of Debye-Hückel screening length, I denotes ionic strength and Z_P the charge of one particle.

With help of the Ornstein-Zernicke (OZ) equation [Hansen & McDonald, 1976]

$$h(r_{12}) = c(r_{12}) + \frac{N}{V} \int_V h(r_{13})c(r_{23})d\vec{r}_3 \quad (2.48)$$

which links the total correlation function $h(r)$ [= $g(r)-1$] and the direct correlation function $c(r)$, and a closure relation of Percus-Yevick (PY), which links the correlation functions and the pair potential, the structure factor $S(q)$ can be calculated by [Hansen & McDonald, 1976]

$$S(q) = \frac{1}{1 - \frac{N}{V} \bar{c}(q)} \quad (2.49)$$

where $\bar{c}(q)$ is the Fourier transformation of the direct correlation function $c(r)$.

In comparison to the hard sphere potential, the effect of electrostatic repulsive interaction on the structure factor has been discussed by Grunder [1993, see Abb. 3 in Pg. 15]. Because of the existence of electrostatic repulsive interaction, the first peak of the structure factor shifts to lower q and the oscillation of the structure factor is stronger.

For dilute solutions ($\phi \ll 1$), where only binary interaction between dissolved particles is to be considered, $g(r)$ is directly related to the pair potential $U(r)$

$$g(r) \cong \exp\left(-\frac{U(r)}{k_B T}\right) \quad (2.50)$$

At low q region for $qr \ll 1$ the Debye factor $\sin(qr)/(qr) \cong 1 - (qr)^2/3!$, the structure factor (2.48) leads to approximation as following [Guinier & Fournet, 1955; Pötschke & Ballauff, 2002]

$$S(q) \cong 1 + 4\pi \frac{N}{V} \int_0^\infty \left[\exp\left(-\frac{U(r)}{k_B T}\right) - 1 \right] \cdot \left[1 - \frac{(qr)^2}{6} \right] \cdot r^2 dr = 1 - 2\phi B_2 \left(1 - \frac{1}{6} q^2 d_{eff}^2\right) \quad (2.51)$$

with the definition of

$$B_2 = -\frac{2\pi}{V_P} \int_0^\infty \left[\exp\left(-\frac{U(r)}{k_B T}\right) - 1 \right] \cdot r^2 dr \quad (2.52)$$

and

$$d_{eff}^2 = \frac{\int_0^\infty \left[\exp\left(-\frac{U(r)}{k_B T}\right) - 1 \right] \cdot r^4 dr}{\int_0^\infty \left[\exp\left(-\frac{U(r)}{k_B T}\right) - 1 \right] \cdot r^2 dr} \quad (2.53)$$

From eq. (2.51) the dependence of structure factor $S(q, c)$ on concentration for dilute solutions may be expressed in the usual virial series [Guinier and Fournet, 1955]

$$\frac{1}{S(q, c)} = 1 + 2B_{app}\phi + O(\phi^2) \quad (2.54)$$

where the apparent virial coefficient B_{app} depends on q for $qd_{eff} \ll 1$

$$B_{app} = 4 \frac{(\pi/6)d_{eff}^3}{V_p} \left(1 - \frac{1}{10} d_{eff}^2 q^2 + O(q^4)\right) \quad (2.55)$$

Here, d_{eff} is a measure for an effective diameter of interaction in dilute regime, which is the minimum distance to which two solute particles may approach each other [Topp et al., 1999]. For hard spheres, $d_{eff} \approx 2R_g$ [e.g. van Helden and Vrij, 1980; Grimson, 1982; Apfel et al., 1994].

Experimentally, the structure factor is obtained as the ratio of the scattering intensity at finite concentration (ϕ^*) and that at vanishing concentration ($\phi \rightarrow 0$). Of course the scattering intensity should be at first normalized to the concentration.

$$S(q) = \frac{[I(q)/\phi]_{\phi=\phi^*}}{[I(q)/\phi]_{\phi \rightarrow 0}} \quad (2.56)$$

2.3.2 Polydisperse systems

In real systems, no matter natural or synthetic macromolecules, the particles have always a size distribution, i.e., the polydispersity of a real system must be considered. In this chapter two commonly used size distribution functions are introduced at first. Then the effect of size polydispersity of particles on the form factor and the structure factor will be discussed, respectively.

Size distribution functions:

Experimentally, the size distribution can be measured by different methods, such as ultracentrifugation and electron microscopy. The size distribution determined from experiment can be applied directly to the computer fit program [e.g., Grunder, 1993; Bolze, 1997]. However, for systems with no information about the size and size distribution there are two kind of distribution functions used commonly in computer simulations, namely Gaussian distribution for symmetric distributed systems

$$W(R_i) = \frac{1}{\sigma\sqrt{2\pi}} \exp\left(-\frac{(R_i - R_0)^2}{2\sigma^2}\right) \quad (2.57)$$

and Schulz-Zimm distribution for asymmetric distributed systems

$$W(R_i) = \frac{1}{\Gamma(m+1)} R_i^m \left(\frac{m+1}{R_N}\right)^{m+1} \exp\left(-\frac{m+1}{R_N} R_i\right) \quad (2.58)$$

where $W(R_i)$ denotes the number of particles with radius of R_i . R_0 is the average radius at peak position for Gaussian distribution. σ and m ($m = 1/(R_W/R_N - 1) - 1$) are parameters characterizing the width of the distributions and $\Gamma(m+1)$ the gamma function of $(m+1)$.

Form factor and structure factor of polydisperse systems:

The scattering intensity for a polydisperse system with particle density $n_i = N_i/V$ (species i with radius R_i) can be formulated as [Moonen, 1988]

$$I(q) = \sum_{i=1}^k n_i \Delta e_i^2 \bar{P}(q) \bar{S}(q) \quad (2.59)$$

with form factor

$$\bar{P}(q) = \frac{\sum_{i=1}^k n_i \Delta e_i^2 P_i(q)}{\sum_{i=1}^k n_i \Delta e_i^2} \quad (2.60)$$

and structure factor

$$\bar{S}(q) = \frac{\sum_{i,j=1}^k \sqrt{n_i n_j} A_i(q) A_j(q) [\delta_{ij} + \tilde{H}_{ij}(q)]}{\sum_{i=1}^k n_i A_i^2(q)} \quad (2.61)$$

$$\tilde{H}_{ij}(q) = 4\pi \sqrt{n_i n_j} \int_0^{\infty} [g_{ij}(R) - 1] \frac{\sin(qR)}{qR} R^2 dR \quad (2.62)$$

where $A_i(q)$ is the scattering amplitude of species i and δ_{ij} the Kronecker delta ($\delta_{ij} = 1$ for $i = j$; $\delta_{ij} = 0$ for $i \neq j$).

Since the topic of this work is cylindrical particles, the effect of polydispersity on the form factors of cylinder and discs are calculated and shown in Fig. 2.14 and Fig. 2.15, respectively. For cylinder with average length $L = 10$ nm and radius in cross-section $R = 0.5$ nm, only the polydispersity in length is discussed in this case ($L \gg R$). From fig. 2.14 it can be seen that the effect of polydispersity in length is hardly observable even with $\sigma/L = 20$ %. It seems that the influence of polydispersity on the form factor can be neglected if $\sigma/L \leq 40$ %, where σ denotes the half width of a Gaussian distribution.

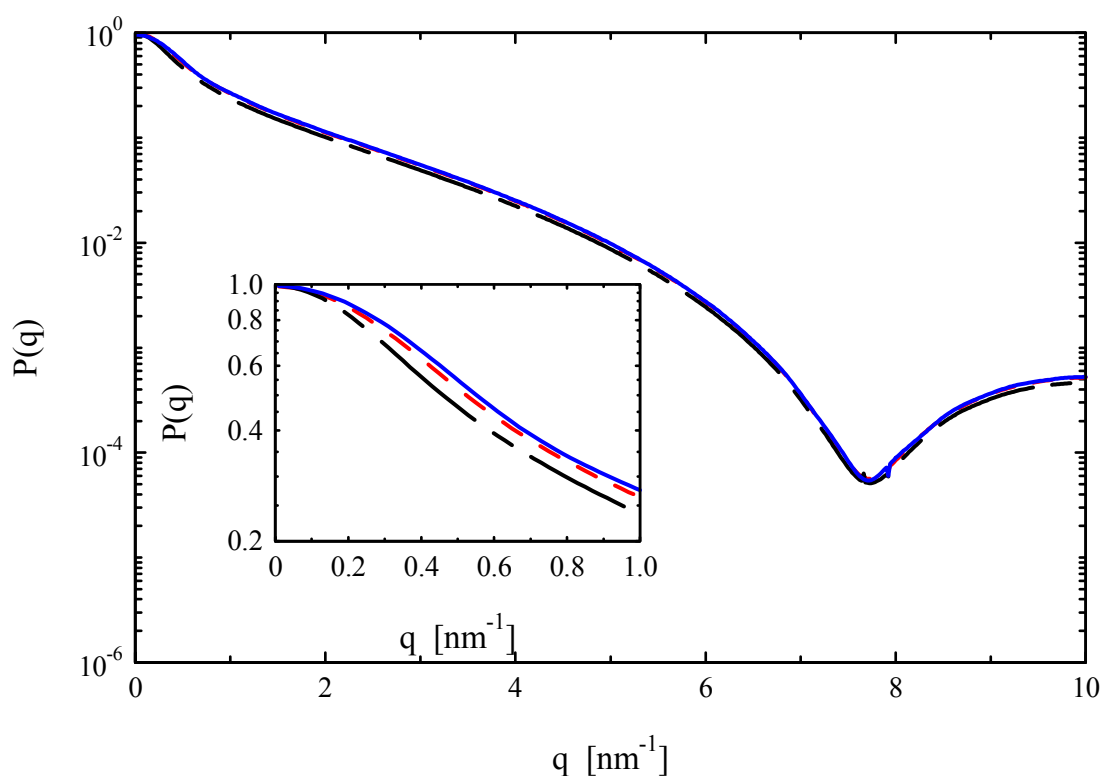


Fig. 2.14 Effect of different polydispersity in length on the form factor of homogeneous rods with average length $L = 10$ nm and radius in cross-section $R = 0.5$ nm. Solid line: monodisperse; dashed lines: polydispersity in length (short dashed line: $\sigma/L = 20$ %; long dashed line: $\sigma/L = 40$ %). For clarity the inset shows the plot again at low q range.

In comparison to cylinder, the effect of polydispersity on the form factor of discs is more pronounced. Fig. 2.15 shows the form factors of discs with average radius $R = 12.5$ nm and thickness $H = 0.9$ nm. In this case ($R \gg H$), we only discuss the polydispersity in radius. At $\sigma/L = 20$ %, the oscillations which exist at low q range and minimum area for monodisperse discs disappear almost completely. Up to $\sigma/L = 40$ % the decay-slope at low q region increases strongly, therefore, the effect of polydispersity on the form factor of discs can never be neglected.

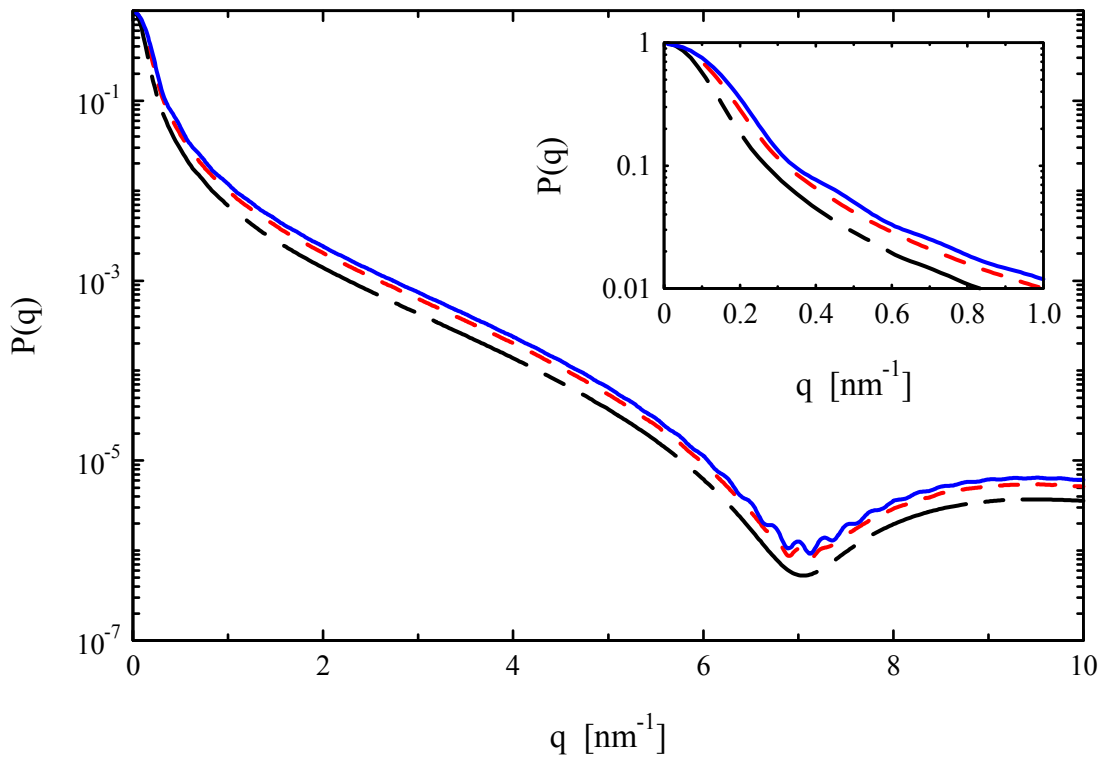


Fig. 2.15 Effect of different polydispersity in radius on the form factor of homogeneous discs with constant thickness of $H = 0.9$ nm and average radius of $R = 12.5$ nm. Solid line: monodisperse; dashed lines: discs with polydispersity in radius (short dashed line: $\sigma/R = 20\%$; long dashed line: $\sigma/R = 40\%$). For clarity the inset shows the plot again at low q region.

Some common characteristics for the effect of polydispersity on the structure factor have been summarized by van Beurten and Vrij [1981] for particles of any shape as: The height of the first peak of $\bar{S}(q)$ decreases with the polydispersity, and the position of the first peak moves to smaller q ; Moreover, the oscillations after the first peak vanish very fast.

Specially, for polydisperse charged discs, the *multicomponent interaction site model* [Harnau, 2001], which is used in this work to compare the experimental structure factor of Laponite particles, will be introduced as follows.

Multicomponent interaction site model:

This model comes from the polymer reference interaction site model (PRISM), but is developed for polydisperse charged discs system.

Consider a multicomponent system involving s species of charged platelet with radius R_i and number density n_i , each platelet of species i contains N_i equivalent interaction sites. The interaction potential between sites on particles of species i and j , carrying the charges $z_i e$ and $z_j e$, will be of the form

$$u_{ij}(r) = \frac{z_i z_j e^2}{\epsilon r} \exp(-\kappa_D r) \quad (2.63)$$

where $\lambda_D = \kappa_D^{-1}$ is the usual Debye screening length and the solvent is assumed to be a dielectric continuum of permittivity ϵ .

The form factor of randomly oriented platelets of species i is expressed as

$$P_i(q) = \int_0^{\pi/2} \sin \theta \left[\frac{2qL \cos \theta \cdot J_1(qR_i \sin \theta)}{q^2 R_i L \cos \theta \sin \theta} \right]^2 d\theta \quad (2.64)$$

where J_1 denotes the cylindrical Bessel function of first order and $P(0) = 1$.

PRISM is based on the assumption that all direct correlation functions between sites on pairs of different platelets are identical. This leaves a total $s(s+1)/2$ independent direct correlation functions $c_{ij}(q)$. The total correlation functions $h_{ij}(q)$ are defined by averaging over the $N_i N_j$ correlation functions between all pairs of sites i and j on two platelets of the same or different species. The two sets of correlation functions are related by the generalized Ornstein-Zernike equations of the PRISM, which in Fourier space is given as

$$h_{ij}(q) = \omega_i(q) c_{ij}(q) \omega_j(q) + \omega_i(q) \sum_{l=1}^s c_{il}(q) \rho_l h_{lj}(q) \quad (3.65)$$

where $\rho_i = N_i n_i$ is the number density of interaction sites of platelets of specie i and $\omega_i(q) = N_i P_i(q)$. The set of $s(s+1)/2$ independent Ornstein-Zernike relations must be supplemented by as many closure relations between each pair of total and direct correlation functions. Here the Laria-Wu-Chandler closure which has recently been used for charged polymers and colloids is adopted

$$h_{ij}(r) = \ln[h_{ij}(r) + 1] + \omega_i * [c_{ij} + (\kappa_B T)^{-1} u_{ij}] \cdot \omega_j \quad (2.66)$$

where the star * denotes a convolution product.

The closed set of equation (2.65) and (2.66) are solved numerically by a standard iterative procedure to obtain partial structure factors

$$S_{ij}(q) = \rho_i \omega_i(q) + \rho_i \rho_j h_{ij}(q) \quad (2.67)$$

Then the static structure factor is given by

$$S(q) = \frac{\sum_{i,j=1}^s S_{ij}(q)}{\sum_{i=1}^s \rho_i \omega_i(q)} \quad (2.68)$$

which is the function used to compare to experimental data.

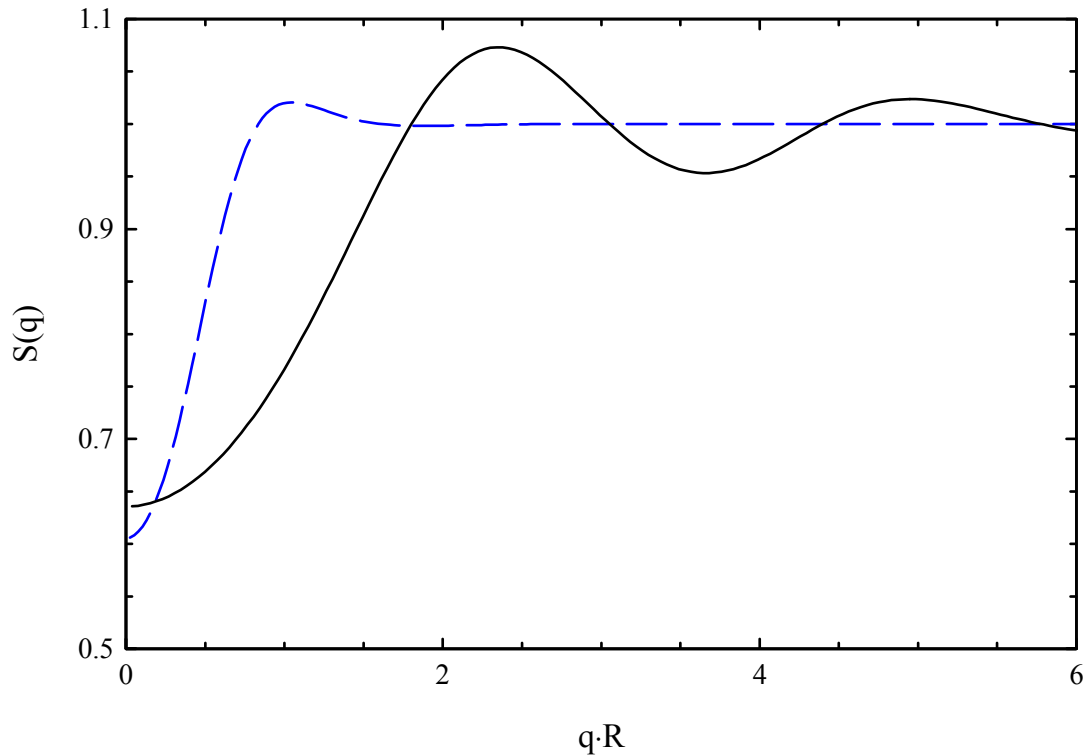


Fig. 2.16 Structure factors of charged discs at volume fraction of 0.16%. The x-axis is multiplied with the radius of discs. Ionic strength of solution $I_S = 1$ mM, effective charges supposed for each particle $Z = 100 e^-$. Solid line: monodisperse; dashed lines: polydisperse in radius with $R_W/R_N = 1.5$ in Schulz-Zimm distribution [Calculated by Harnau using the multicomponent interaction site model].

By using this multicomponent interaction site model, Fig. 2.16 shows the influence of polydispersity in radius of discs on the structure factor. Except for the fact that $S(0)_{\text{poly}} > S(0)_{\text{mono}}$ in this case, which is opposite to hard spheres [cf. Dingenouts, 1999 (dissertation), Pg. 35], the height of the first peak of $\bar{S}(q)$ decreases with the polydispersity and vanishes very fast with q , and the position of the first peak moves to smaller q , as expected.

2.4 Interpretation of scattering functions

Above all, from an experimental point of view, the procedure of interpretation of scattering function may be summarized in Fig. 2.17:

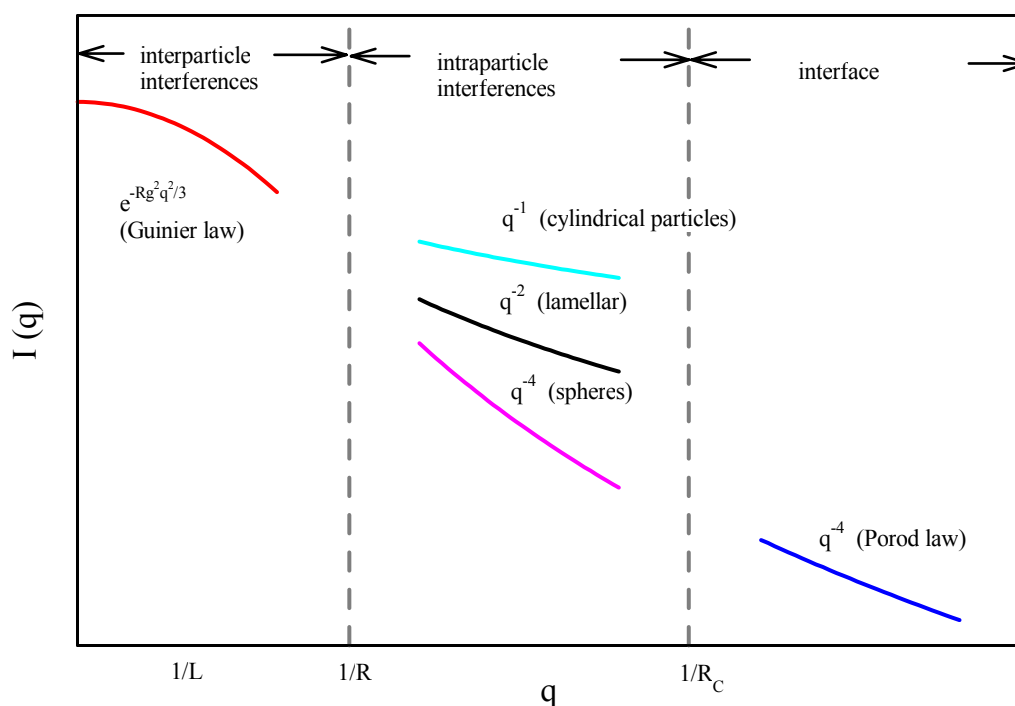


Fig. 2.17 Scaling law of scattering intensity at different scattering vector region, where L denotes the length of a rod, R the radius of a sphere or a platelet and R_C the diameter of a rod perpendicular to the length direction.

- (1) In the Guinier range, i.e., the smallest q range, the inter-particle interference is in most cases not negligible for experimental measurable solutions, even for dilute solutions. The strategy to exclude the inter-particle interactions is the extrapolation of concentration which will be discussed in more detail in chapter 4 and 5. The

resulted scattering intensity of single particles can then be used to determine the radius of gyration R_g of particles in solvent and its molecular weight M_W . For polymer chains, moreover, some details about the chain statistics can be obtained by studying R_g^2 as a function of the molecular weight M_W . Flory [Flory, 1953] has given an universal relationship between the mean square radius of gyration and the molecular weight:

$$R_g^2 = K_{r,\varepsilon} \cdot M^{1+\varepsilon} \quad (2.69)$$

where $K_{r,\varepsilon}$ is a characteristic parameter of the individual polymer and ε represents interactions between polymer chains and solvent which equals to zero for Gaussian chain and approaches a limiting value of 0.2 with increasing A_2 [Schulz and Kirste, 1961].

- (2) In the intermediate q range, the spatial resolution is improved, and the correlations inside particles are observed, i.e., the scattering function is form factor of particles in this range. As shown in Fig. 2.19, e.g., a decay of q^{-1} implies a cylindrical particle shape and q^{-2} for a flat are distinguish characteristics which have been discussed above. Of course, the effect of radius in cross-section for cylindrical particles and the thickness for flat particles should be corrected.
- (3) In highest q range, i.e., the tail of the scattering function, the structure of interface should be observed, provided that there exists a well defined internal surface. Debye [Debye, 1957] and Porod [Porod, 1951] derived independently the fourth power law of scattering functions for the final slope:

$$I_0 = (\Delta\rho)^2 \cdot \frac{2\pi}{q^4} \cdot S \quad (2.70)$$

where S denotes the specific surface of particles in solution and can be determined by eq. (2.70).

Finally, the most critical approach for the above analysis procedure is the comparison of experimental data with predicted model calculation over all experimental reached q range which maybe cost most time of the SAXS work, however, provide proof for accurate experimental data and suitable model descriptions.

3 Experimental techniques

Since most of the SAXS data of the present work were obtained by a modified Kratky-Compact-Camera, the construction and set-up of this camera as well as the data evaluation procedure will be introduced in detail. In addition, the techniques of SAXS by synchrotron radiation and static light scattering, which are also performed to analyse Laponite in combination with Kratky-Compact-Camera, are described briefly at the end of this chapter.

3.1 SAXS by a modified Kratky-Compact-Camera

3.1.1 Construction and set-up of Kratky-Compact-Camera

The Kratky-Compact-Camera [Kratky, 1958; 1982] is available since 1954. A modified camera, as shown in Fig. 3.1 [Dingenouts et al., 1999], differs from the conventional design mainly on the enhanced distance of sample-to-detector. This device is capable of measuring particles up to a diameter of 200 nm. It consists of an X-ray generator (1), a block collimation system (2), a sample holder (3), a primary beam-stop (4) and a linear position-sensitive detector (5). The characteristic of the camera is its block collimation system (Fig. 3.2). Collimation of the beam is achieved by three construction elements: two blocks B_1 , B_2 and the edge E. The upward surface of B_1 coincides exactly with the downward surface of B_2 . This defined plane is called main section. The width of the entering beam is determined by the distance between the edge E and the main section. The advantage of this block collimation system is that there is no obvious parasitic scattering due to the asymmetric design. The reduced background permits experiments with very weakly scattered samples, e.g. polymers in solution. Of course, the finite dimensions of the primary beam lead to a smearing of the measured intensity, which should be desmeared and give out scattering result as that would be when measuring in point collimation.

The set-up of the Kratky-Compact-Camera is as follows: The X-ray generator (Kristalloflex 710H) is manufactured by Siemens containing a sealed X-ray tube (AEG FK60-04/12) with copper anode. The operating voltage is 35 kV with an anode current of 30 mA. A nickel filter is used to mask the Cu-K_β line so that only a monochromatic X-ray

source with wave length of 0.154 nm (Cu- K_{α} line) is used throughout all experiments . The X-ray tube is cooled by circulating water with temperature of $20 \pm 0.2^{\circ}\text{C}$ to ensure a stable primary intensity. Samples are filled in a quartz glass capillary with a diameter of 1 mm and wall thickness of 0.01 mm. The inner of the camera is evacuated using an oil vacuum pump. The primary beam intensity profile is determined by a moving device [Stabinger and Kratky, 1978]. The scattering intensity and position are recorded by a linear position-sensitive detector (Braun OED-50m), which works under mixed gas of argon and methane (90:10). Since the detector is very sensitive to the pressure of gas which strongly depends on temperature, the room temperature is controlled within $\pm 2^{\circ}\text{C}$ by the air conditioner.

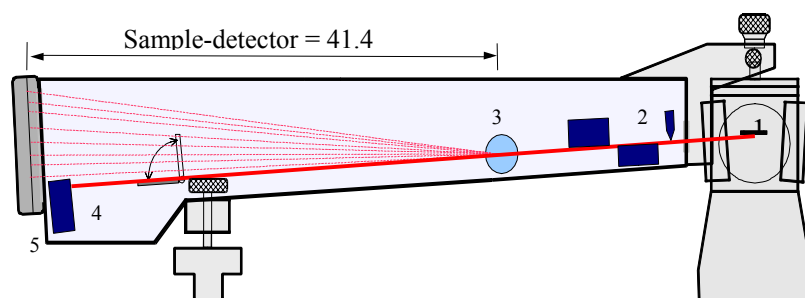


Fig. 3.1 Schematic description of the Kratky-Compact-Camera. 1 represents the X-ray quill, 2 the block collimation system, 3 sample holder, 4 primary beam-stop to catch the direct beam, and 5 linear position-sensitive detector.

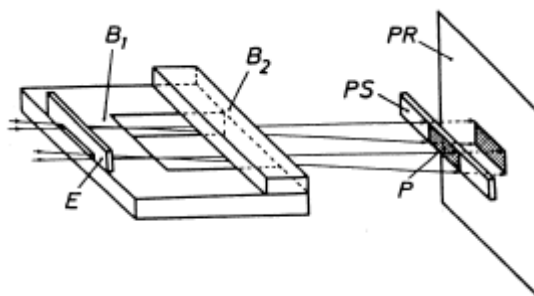


Fig. 3.2 Schematic description of the block collimation system (B_1 , B_2 and E) [Kratky, 1982]. (P) primary beam profile; (PS) primary beam-stop; (PR) plane of registration.

3.1.2 Smearing

The effect of the finite dimension of the primary beam on the scattering intensity, defined as commonly smearing, leads to some loss of the structure information in scattering function. This smearing effect is geometrically described in Fig. 3.3. The smeared scattering intensity $\tilde{I}(m)$ in registration plane with height m may be expressed as [Glatter & Zipper, 1975]:

$$\tilde{I}(m) = \int \int_{-\infty}^{\infty} I_0(x,t) \cdot I(\sqrt{(m-x)^2 + t^2}) dx dt \quad (3.1)$$

where $I_0(x,t)$ is the two dimensional primary intensity distribution in sample plane, and $I(m)$ is the scattering intensity which would result when measuring in point collimation.

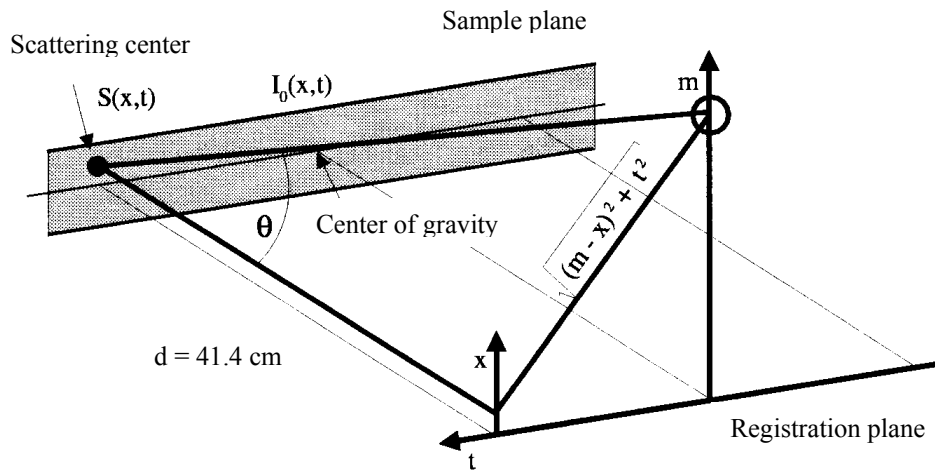


Fig. 3.3 Geometrical description of the two dimensional smearing effect: In isotropic system each scattering center $S(x,t)$ in sample plane yields a cone-shaped scattering, whose intensity depends only on the angle of the cone θ and the primary intensity $I_0(x,t)$. So the from detector registrant scattering intensity at height m corresponds to the angle θ or the length $\sqrt{(m-x)^2 + t^2}$.

Because the length (t-direction) of primary beam is very large compared to the width (x-direction) and the two distribution $P(t)$ and $Q(x)$ are independent, the intensity distribution $I_0(x,t)$ can be written as a product of two independent distributions as [Glatter & Zipper, 1975]

$$I_0(x,t) = P(t) \cdot Q(x) \quad (3.2)$$

The smeared intensity $\tilde{I}(m)$ can then be separated to two parts, related to length effect and width effect, respectively:

$$\tilde{I}(m) = \int_{-\infty}^{\infty} P(t) \cdot I(\sqrt{m^2 + t^2}) dt \quad (3.3)$$

$$\tilde{I}(m) = \int_{-\infty}^{\infty} Q(x) \cdot I(m-x) dx \quad (3.4)$$

The sequence of the integral can not be changed, i.e., the length effect must be considered before width effect.

To correct experimental scattering intensity for the finite dimension of the primary beam the integral of eq. (3.3) and (3.4) must be solved inversely, i.e. $I(m)$ should be obtained from $\tilde{I}(m)$. As a result, the integral for the width effect in this case should be done at first. This so-called desmearing procedure will be discussed in detail in the following section.

3.1.3 Data treatment

In order to obtain the absolute scattering intensity $I(q)$ as a function of scattering vector q , the experimental data have to be treated in following steps:

- (1) Measurements (capillary, solvent, solutions separately);
- (2) Scattering intensity normalized to the exposure time and the primary beam intensity;
- (3) Subtraction of the scattering intensity of sample from background (capillary and solvent);
- (4) Desmearing of the scattering intensity for the finite dimension of the primary beam;
- (5) Correction of the scattering intensity to the absolute height.

Measurements and normalization:

The experimental raw data (including scattering intensities of empty capillary, solvent filled capillary and solution filled capillary) should be at first normalized to the exposure time t_0 and primary beam intensity I_0 . To protect the detector a moving device (in front of the block collimation system with a slit of 34 μm width) and a fest block (before detector with a slit of 100 μm width) are performed to measure the primary beam intensity before and after each measurement. The exposure time of each measurement is set to 1-24 hours, depending on the scattering power and concentration of the sample. $I_0 = 10000$ and $t_0 = 600$ sec are taken as referent values for the primary beam intensity and exposure time, respectively, so that different measurements are comparable.

Background Subtraction:

The scattering intensity of particles $I_P(h)$ is then obtained by

$$I_P(h) = I_S(h) - (1 - \phi)I_B(h) - \phi I_C(h) \quad (3.5)$$

where ϕ denotes the volume fraction of the particles; $I_S(h)$, $I_B(h)$ and $I_C(h)$ represent the scattering intensities of solution, background and empty capillary, respectively.

As an example, the data measured from a model latex sample polymethylmethacrylate (PMMA) with volume fraction $\phi = 0.023$, radius $R = 39$ nm and polydispersity $\sigma/R = 7\%$ are used to describe the procedure of data analysis in detail.

Fig. 3.4 shows the effect of background subtraction, according to eq. (3.5) by using the sample descried above. Obviously, the scattering intensity after the subtraction decrease more rapidly than original data from $h = 1$ mm and the accuracy of data decreases with increasing h due to the reduced difference between the scattering intensity of sample and background (see inset of Fig. 3.7).

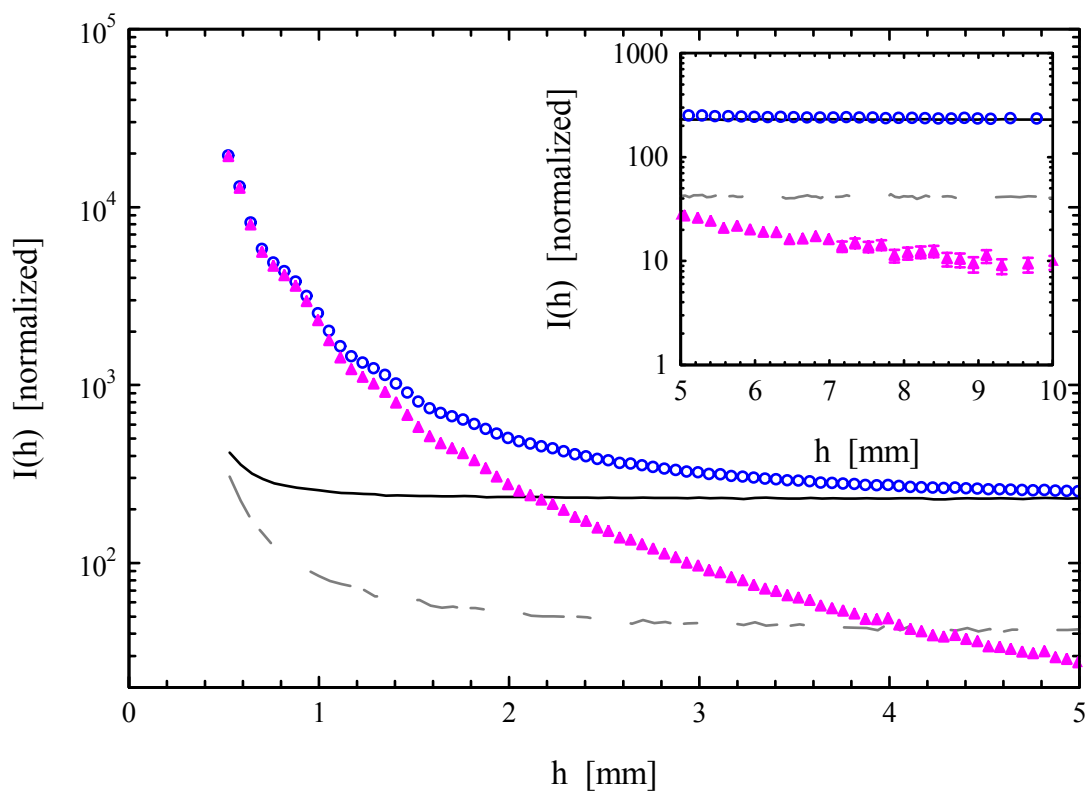


Fig. 3.4 Scattering intensities of a latex sample (PMMA, $\phi = 0.023$ with radius $R = 39$ nm and polydispersity $\sigma/R = 7\%$) before (circles)/after (filled triangles) background subtraction as a function of h (distance to center of primary beam). Dashed line: scattering intensity of empty capillary; Solid line: scattering intensity of solvent (water) filled capillary. The inset shows all the curves at higher q , where the background subtracted data have bigger error than those at low q because of the reduced difference between the scattering intensity of sample and that of background.

Smoothing and Desmearing:

For Kratky camera, the key step of data treatment lies in the desmearing for the finite dimensions of the primary beam. Because of the relative big statistic error at high q range, smoothing of data before desmearing or thereafter is in most cases necessary. However, this smoothing should not add any artificial structures to the scattering function. To be sure about that, a comparison between the desmeared data with smoothing and those without any smoothing should always be done.

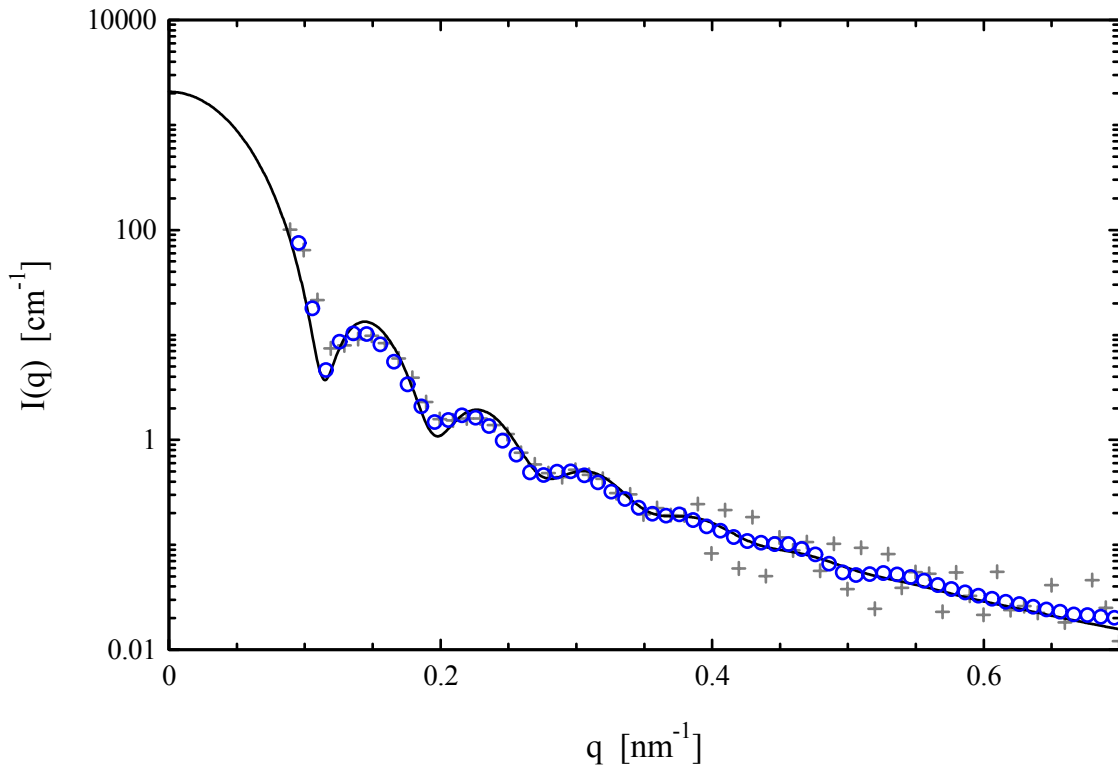


Fig. 3.5 Desmeared scattering intensities of a latex sample (PMMA, $\phi = 0.023$ with radius $R = 39$ nm and polydispersity $\sigma/R = 7\%$) with (circles)/without (crosses) preliminary smoothing. Solid line: theoretical scattering intensity.

For spherical systems, since the scattering function has several maximums and minimums and it falls down rapidly with q^{-4} , the smoothing procedure is always necessary for data at high q range and should be performed before desmearing. Fig. 3.5 compares the desmeared scattering intensities of the sample described above with /without preliminary smoothing to the theoretical curve. At least for data at high q range the desmeared data with preliminary smoothing approaches the theoretical curve better than those without any smoothing.

For non-oscillated scattering functions (e.g. polymer chains) the smoothing procedure can be performed also after the desmearing. There are two ways of smoothing: one is averaging data with cubic spline and the other is averaging data with neighbours. The former is performed by a piecewise approximation by polynomials, which are controlled by the

performer and hence needs more practical experience. The latter is easier to handle for the performer but can be only applied to non-oscillated scattering functions.

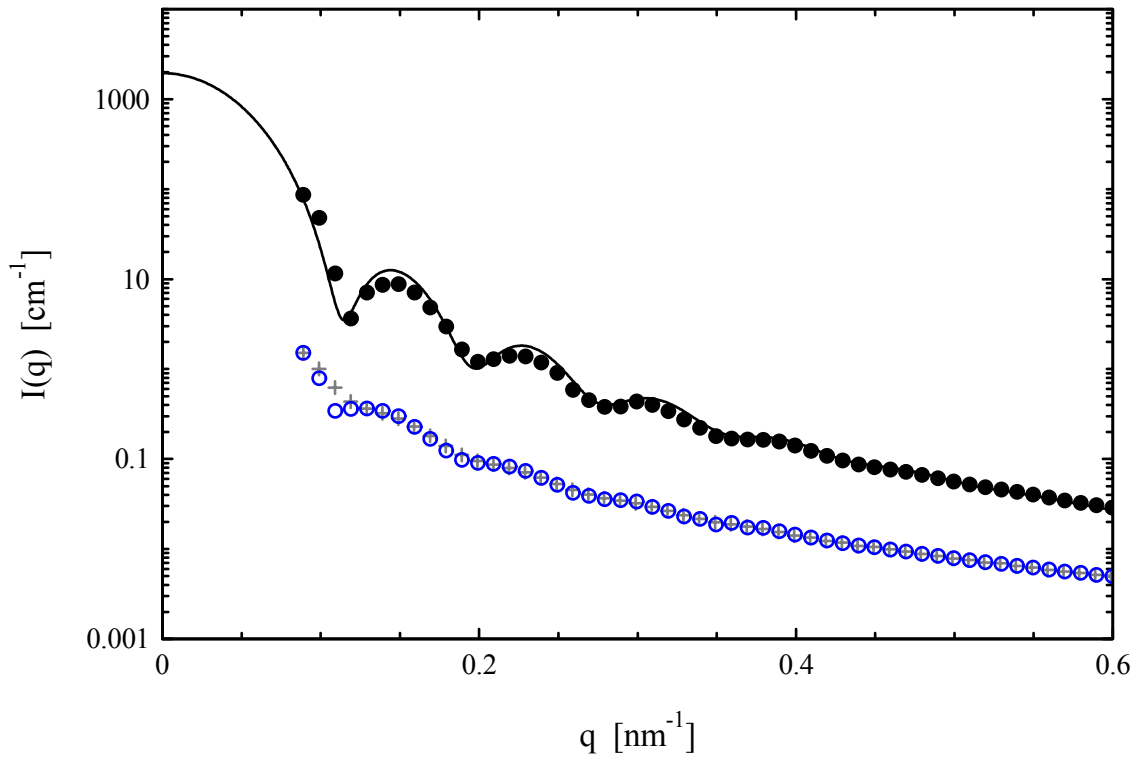


Fig. 3.6 Effects of the width and length desmearing on the scattering function of a spherical system (PMMA at $\phi = 0.023$ with $R = 39$ nm, $\sigma/R = 7\%$). Crosses: smeared scattering intensity; Circles: width desmeared scattering intensity; Filled circles: width and length desmeared scattering intensity; Solid line: theoretical scattering function for this system.

Following Glatter and Zipper [1975], the effect of $Q(x)$ (width effect) must be corrected before the effect of $P(t)$ (length effect). As an example, Fig. 3.6 shows the effects of both width and length desmearing for the spherical system. The width effect on the first minimum is significant. For non-oscillated data, however, the width effect is negligible (conf. Fig. 3.7).

Compared to the width effect, the length effect is in no case negligible. It is easy to understand because the length scale is much larger than the width scale. Fig. 3.6-3.7 show clearly how significant the length effect is on the experimental data. For spherical system, the length desmearing affects strongly not only the slope of the scattering function but also the distinction of the oscillation, while for non-oscillated data it only increases the slope and the absolute scattering intensity.

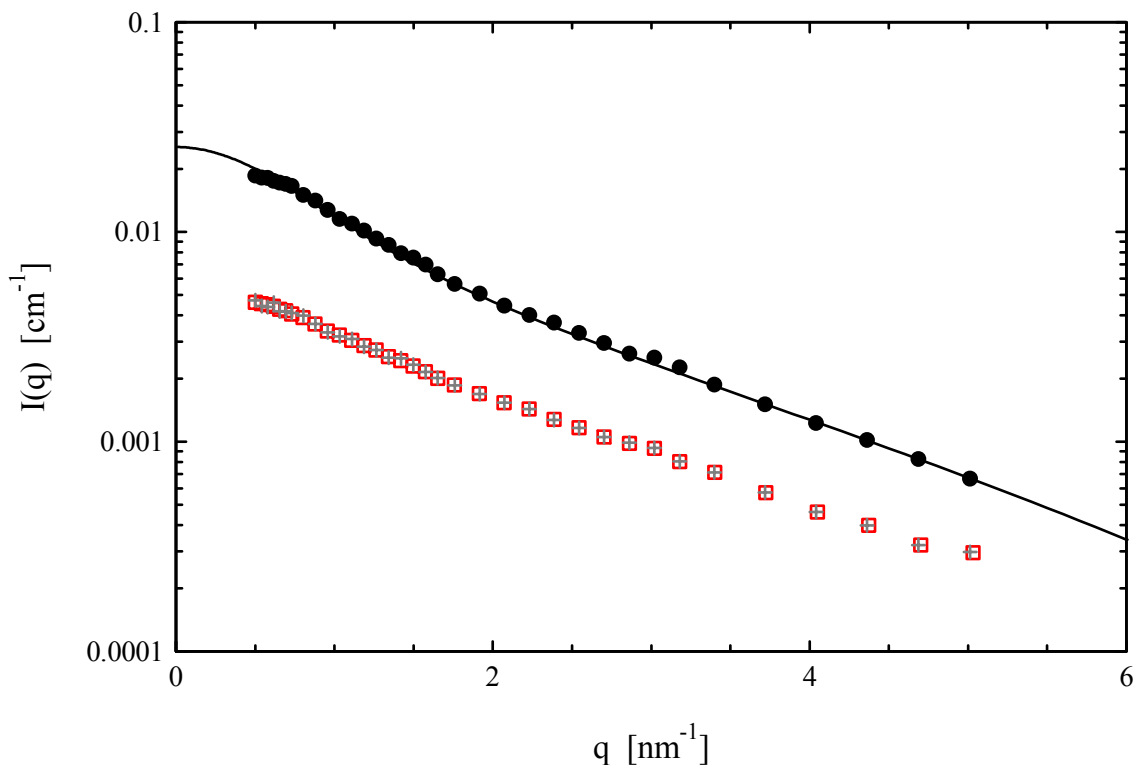


Fig. 3.7 Effects of the width and length desmearing on the scattering function of polymer chains (polymer carbon suboxide). Crosses: smeared scattering intensity; Squares: width desmeared scattering intensity; Filled circles: width and length desmeared scattering intensity. The polymer chains have structure parameters of: contour length $L_C = 7$ nm, Kuhn length $b = 3$ nm and radius of gyration in cross-section $R_C = 0.3$ nm. The solid line is theoretical curve for this system.

For method of desmearing we discuss mainly the two widely used ones: Gaussian [Schmidt, 1965] and iterative [Lake, 1967] methods. The former assumes Gaussian $P(t)$ and $Q(x)$ functions, which allows partial integration and avoids the computation of the first derivation, whereas the latter method allows arbitrary slit functions of $P(t)$ and $Q(x)$. For spherical systems, Gaussian desmearing is preferred for giving the oscillation structure better than iterative, moreover, because in this case the scattering intensity decays rapidly with q^{-4} , the Gaussian approximation of $P(t)$ does not cause significant derivation at high q as it does for slowly decayed scattering functions (e.g. polymer chains). For non-oscillated scattering functions the results from both methods are identical at low q provided that the number of necessary iterative steps is correctly estimated. However, at high q the desmeared intensity

by iterative method is closer to theoretical curve, and it is therefore suggested for treating slowly decayed scattering functions. This discussion is observable in Fig. 3.8, which shows the desmeared scattering intensities of poly(carbon suboxide) chains (with contour length $L_C = 8$ nm, Kuhn length $b = 3$ nm and radius in cross-section $R_C = 0.3$ nm) by both methods.

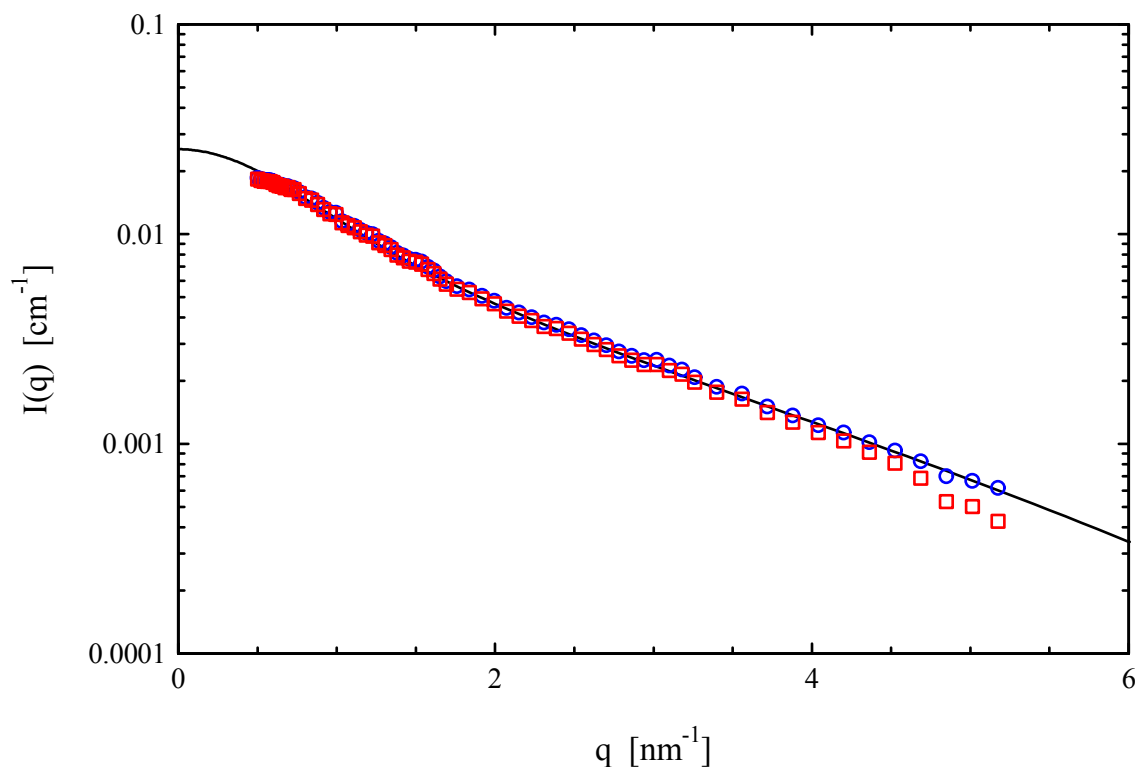


Fig. 3.8 Scattering intensities of polymer carbon suboxide at volume fraction of 0.37% (interparticle interaction is excluded), desmeared by iterative method (circles) and Gaussian method (squares). The polymer chains have structure parameters of: contour length $L_C = 7$ nm, Kuhn length $b = 3$ nm and radius of gyration in cross-section $R_C = 0.3$ nm. The solid line is theoretical curve for this system.

Correction to absolute intensity:

The desmeared scattering intensity should be then corrected to the absolute height of intensity. The main error when determining absolute scattering intensities by the moving slit device arises from the insecure determination of the resolution function of the position-sensitive counter [Dingenouts, 1999]. In our experiment, a width of 80 μm has been used which is supplied by the manufacturer. The correction factor can be taken from the ratio of scattering intensity $I(0)$ of some simple liquids, e.g. water, toluene or ethanol, measured

under the same camera set-up at $q = 0$ to its theoretical value $I(0)_T$, which can be calculated by [Guinier & Fournet, 1955]

$$I(0)_T = \rho_{e^-}^2 \cdot k_B \cdot T \cdot \kappa_T \quad (3.6)$$

where ρ_{e^-} denotes the electron density and κ_T the isotherm compressibility of the simple liquid, which are listed in Table 3.1 for some widely used chemicals at 298 K [Lide, 1995-6]

Table 3.1 Theoretical scattering intensity of some simple liquids at $q = 0$ and $T = 298\text{K}$

| <i>Parameter</i> | <i>Water</i> | <i>Toluene</i> | <i>Ethanol</i> |
|-----------------------------------|--------------|----------------|----------------|
| ρ_{e^-} [e/nm ³] | 333.3 | 283.1 | 266.9 |
| κ_T [Pa] | 4.57 | 8.96 | 11.19 |
| $I(0)_T$ [cm ⁻¹] | 0.016 | 0.023 | 0.025 |

3.1.6 Sources of error

The statistic error from the counting rate measurement and the error propagation can be quantitatively estimated by the evaluation program. For example, Fig. 3.12 shows the scattering intensities as well as the statistic error for two samples of the same polymer chains (polymer carbon suboxide) with different volume fractions (0.4% and 1.2%, respectively). On one hand, both curves have a relative bigger error at high q region than the low q one due to the weaker scattering intensities at high q . On the other hand, the scattering intensity of the sample with higher volume fraction shows smaller error than others at all q region. So, this kind of error can be reduced through long time exposure and combined with measurements at high concentration.

Other possible sources of error, e.g. intensity fluctuation of the X-ray source, fluctuation of room temperature, the different count-rate capability along the metal wire etc. can only be estimated roughly. To avoid or minimise these kinds of errors, the best way is to repeat the measurements and to perform them with different exposure times. Data from long time

exposure can be accepted only when they lie in the average positions of those from short time exposure, if the sample shows no time dependence.

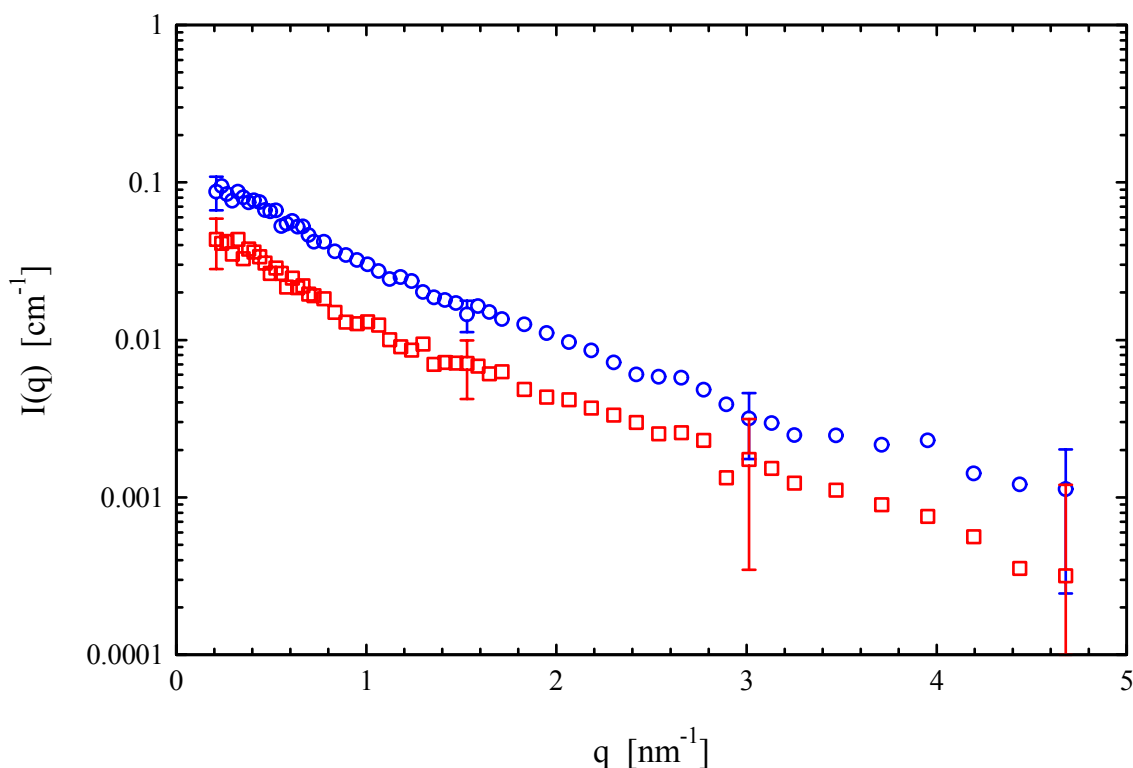


Fig. 3.9 Scattering intensity of a polymer system (polymer carbon suboxide in aqueous solution) at concentrations of 0.4 wt% (squares) and 1.2 wt% (circles) with error bars.

Too strong smoothing can also give rise to extra error. A general way to avoid this problem is to compare the desmeared curves with the preliminary or afterwards smoothing to those without any smoothing. The former points should lie always in the average position of the latter and never create artificial structures. As an example Fig 3.10 shows a set of desmeared scattering data of dissolved polymer carbon suboxide with very limited contrast to the background. The smoothed data (solid line) give a good approach to the non-smoothed ones (open squares).

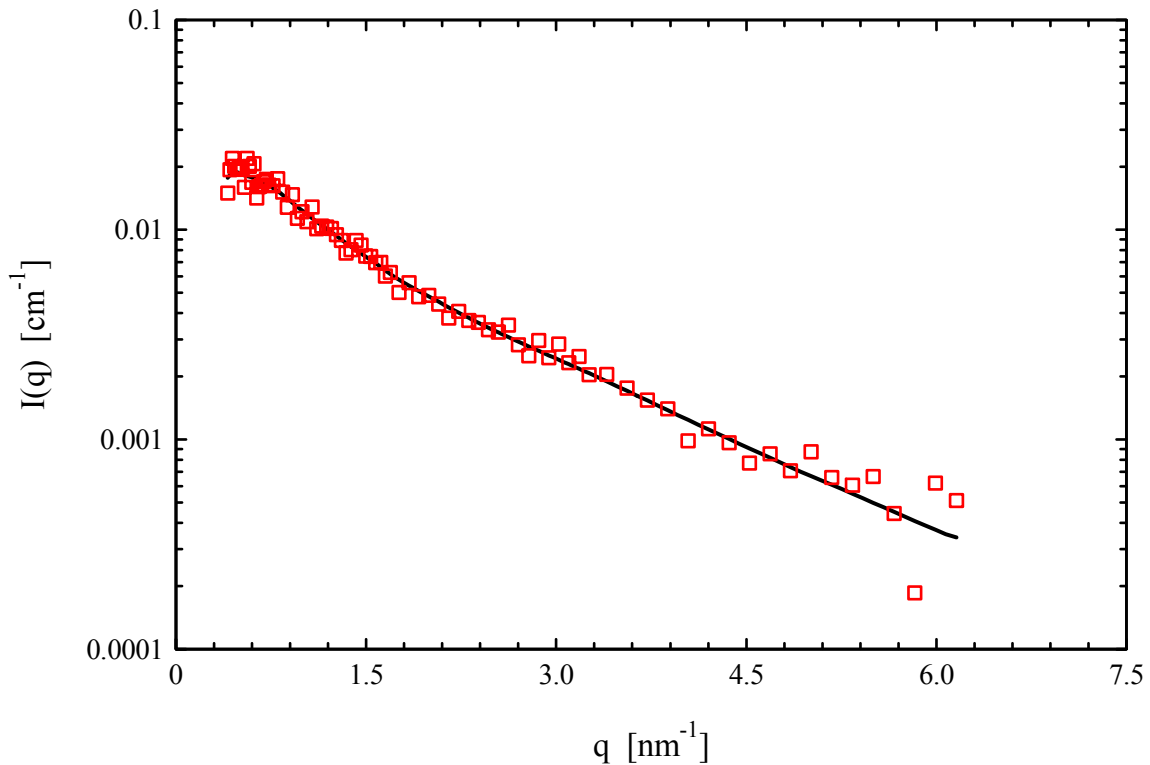


Fig. 3.10 Effect of smoothing: Desmeared scattering intensities of dissolved polymer carbon suboxide at volume fractions of 0.40% without smoothing (open squares) and with preliminary smoothing (solid line).

3.2 SAXS by synchrotron radiation

The synchrotron experiments were performed at the European Synchrotron Radiation Facility (ESRF) in Grenoble on the high brilliance beam line ID2 (Fig. 3.11). The instrument has been introduced by Bösecke [1992]. The instrumental set up for the present work (chapter 4) is: wavelength $\lambda = 0.0995$ nm with energy 12460 e.V, sample-detector distance $d = 10$ m which covers an experimental range in q at $2.15 \times 10^{-2} - 0.67 \times 10^{-1}$ nm $^{-1}$. A two-dimensional image-intensified charge-coupled device (CCD) is employed as the detector, which allows the study of the isotropy and anisotropy of the scattering. The CCD detector has several advantages in comparison to the existing gas detectors [Pontoni, 2002], such as

quantum-limited efficiency, high spatial resolution, not restricted by the count rate but the pixel well capacity.

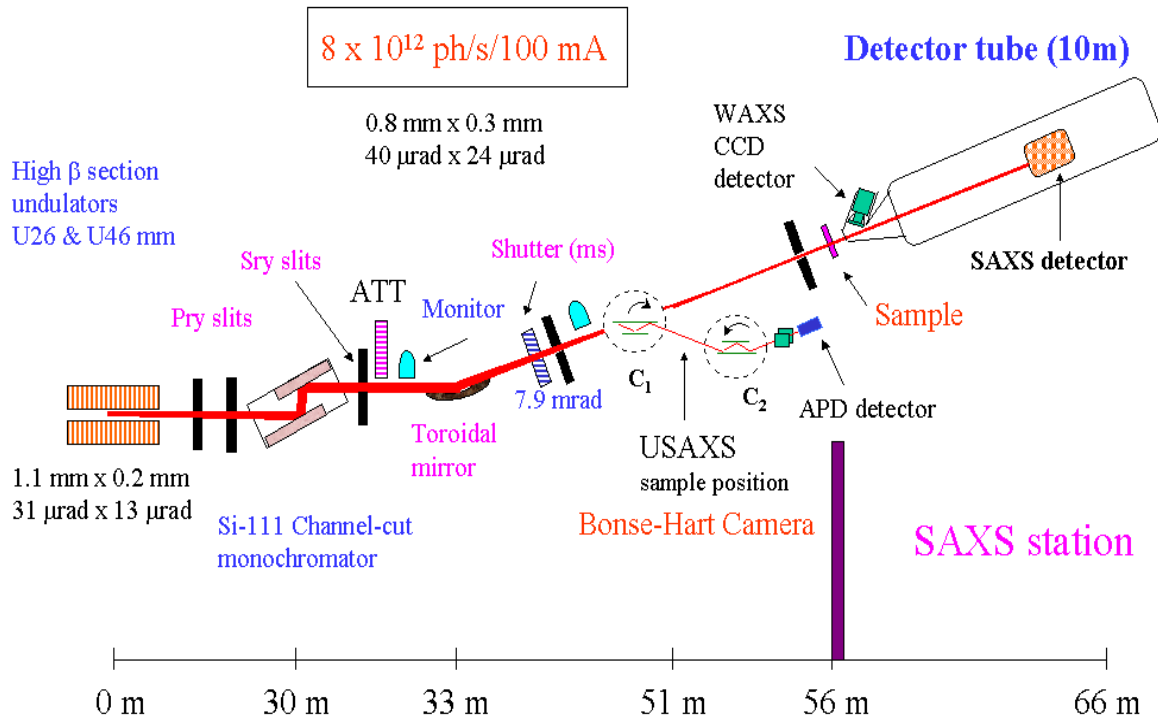


Fig. 3.11 ID2 beamline layout [http://www.esrf.fr/exp_facilities/ID2]

In comparison to the SAXS experiments by Kratky-camera in laboratory, the main advantages of synchrotron radiation lie in the fact that:

- High-brilliance \rightarrow exposure time limited (millisecond), high efficiency and allow time-resolved investigations \rightarrow low statistic error of data.
- Two dimensional CCD detector \rightarrow advantages described above.
- Point collimation \rightarrow high angular resolution down to very low scattering vectors \rightarrow simple data evaluation, no desmearing needed.
- Distance of sample-detector adjustable \rightarrow flexible q range.

3.3 Static light scattering

For static light scattering the light source is a 10 mW He-Ne laser with vertical polarization at a wave length $\lambda = 632.8$ nm. The sample is contained in a cylindrical 10 mm diameter quartz cuvette, which is immersed in an index-matching toluene bath of 80 mm diameter. Scattered light with vertical polarization is detected by a photomultiplier that is mounted on a goniometer arm. The angle range is 35-125 °C, corresponding to q range of $7.9 \times 10^{-3} - 2.3 \times 10^{-2} \text{ nm}^{-1}$.

Scattering intensities on an absolute basis (Rayleigh ratios R_θ) were obtained using a benzene standard for calibration. For polymer chains the scattering results were treated using the scattering equation based on the Rayleigh-Debye theory [Zimm, 1948; Kerker, 1969]

$$\frac{Kc}{R_\theta} = \frac{1}{M_w P(\theta)} + A_2 c \quad (3.7)$$

where $P(\theta)$ is form factor of the dissolved polymer chains, which is almost unity for colloidal sized chains at the covered θ or q range. A_2 is the second osmotic virial coefficient which is determined by the chemical structures of both polymer and solvent molecules. If $A_2 = 0$, i.e., the repulsion between the atoms of approaching polymer segments is compensated by attractional van-der-Waals forces, the polymer solution shows a pseudo-ideal behavior which is the so-called theta-point of polymer solutions. M_w denotes the weight average molecular weight of measured particles. K is an optical constant, given by

$$K = \frac{4\pi^2 \cdot n_0^2 \cdot \left(\frac{dn}{dc}\right)^2}{\lambda^4 \cdot N_A} \quad \left[\frac{\text{cm}^2 \cdot \text{mol}}{\text{g}^2} \right] \quad (3.8)$$

where n_0 is the refractive index of the dispersion medium (for water $n_0 = 1.3314$), λ the wavelength of light, dn/dc the refractive index increment and N_A Avogadro constant.

The first term on the right of eq. (3.7) is due to intra-molecular interference, whereas the higher term relates to the inter-molecular interferences. Eq. (3.7) may be performed to determine the weight average molecular weight M_w and radius of gyration R_g of dissolved

polymer chains by the so-called Zimm-plot, i.e., the plot of $Kc/R(q,c)$ versus $q^2 + \text{constant} \cdot c$, which allows a simultaneous extrapolation to $q = 0$ and $c = 0$.

The line at $q = 0$ has the equation

$$\lim_{q \rightarrow 0} \frac{K \cdot c}{I(q,c)} = \frac{1}{M_w} + 2A_2 \cdot c + \dots \quad (3.9)$$

And the line at $c = 0$ has the equation

$$\lim_{c \rightarrow 0} \frac{K \cdot c}{I(q,c)} = \frac{1}{M_w \cdot P(q)} = \frac{1}{M_w} \left(1 + \frac{R_g^2}{3} \cdot q^2 \pm \dots\right) \quad (3.10)$$

from which M_w , A_2 and R_g can be obtained simultaneously.

3.4 Mass density measurement

For the evaluation of the SAXS data, the determination of the mass density ρ_p of the polymer in solvent is necessary, especially for the determination of the molecular weight M_w . A density meter (DMA 60, Paar) was used to measure the densities ρ of solutions at 298 K. In the diluted regime the density ρ of the solution is proportional to the concentration c of the solute. From the slope (density increment $d\rho/dc$) and the intercept (density of medium ρ_0) of the linear regression ρ_m can be obtained as follows:

$$\rho_m = \rho_0 / \left(1 - \frac{d\rho}{dc}\right) \quad (3.11)$$

and its partial specific volume \bar{v}_2 is given by:

$$\bar{v}_2 = \left(1 - \frac{d\rho}{dc}\right) / \rho_0 \quad (3.12)$$

The determination of mass density for the system of poly(carbon suboxide) in aqueous solution is shown in Fig 3.12. From the linear regression the mass density of poly(carbon

3 Experimental techniques

suboxide) is determined to be $1.64 \pm 0.02 \text{ g/cm}^3$, which agrees well with literature value [1.65 g/cm^3 from Snow, 1978].

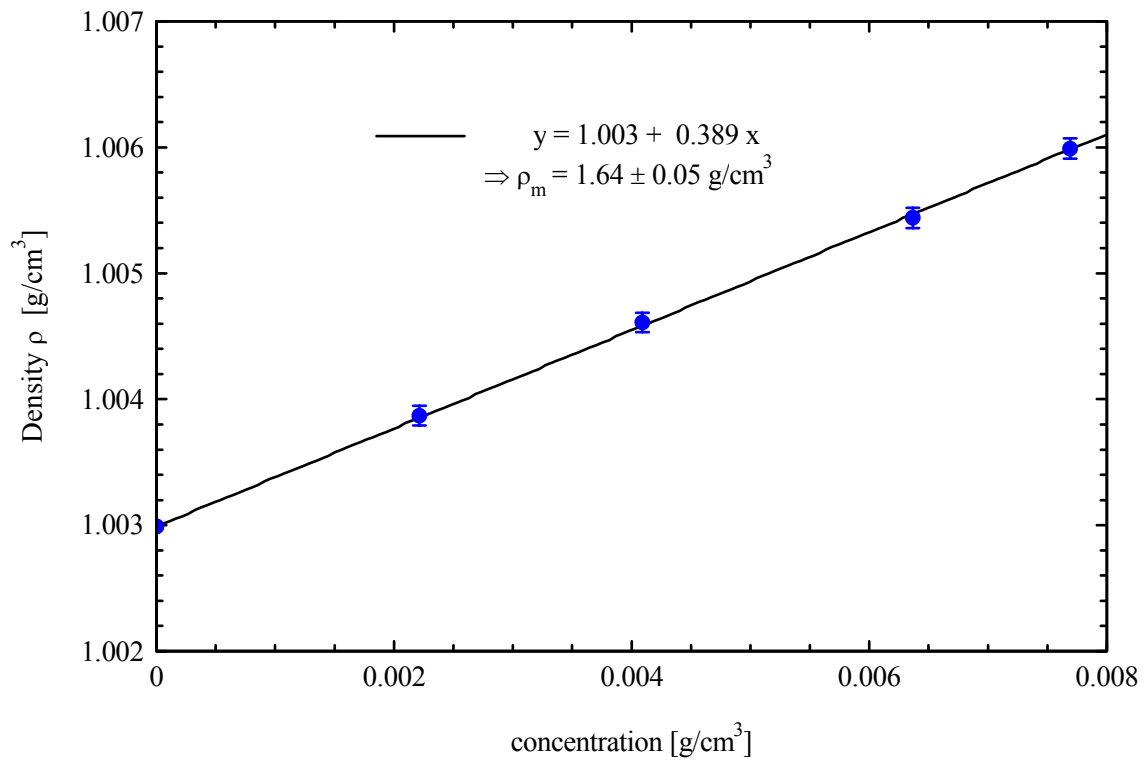
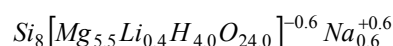


Figure 3.12 Density determination of poly(carbon suboxide) dispersions in aqueous solution at 298 K.

4 Structural analysis and interaction of Laponite particles in aqueous solutions

4.1 Introduction

Laponite, an entirely synthetic clay of smectite type, is formed by combining salts of sodium magnesium and lithium with sodium silicate at carefully controlled rates and temperature [www.laponite.com]. This obtained amorphous precipitate is then partially crystallized at high temperature. The resulting product is filtered, washed, dried and milled to give a fine white powder. The chemical composition of a typical Sodium Laponite (Laponite RD) is given by: 66.2% of SiO₂, 30.2% of MgO, 2.9% of Na₂O and 0.7% of Li₂O, which corresponds to an empirical formula as:



The unit cell of Laponite crystal is comprised of six octahedral magnesium ions sandwiched between two layers of tetrahedral silicon atoms, with these groups balanced by twenty oxygen atoms and four hydroxyl groups (Fig. 4.1a).

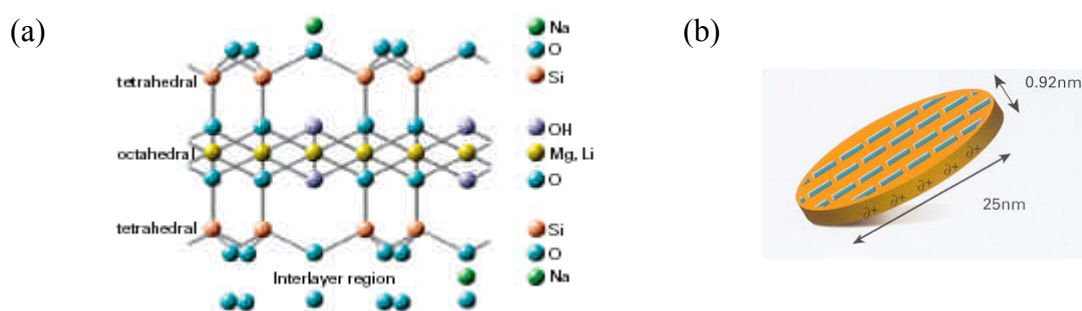


Fig. 4.1 (a) Chemical structure of the primary Laponite particle, as seen from aside (facing the rim). The legend on the right in displays the elements present in this structure in a horizontal fashion [www.laponite.com]; (b) Disk-shaped Laponite particle in aqueous solution, with size of 25 nm in diameter and 0.92 nm in thickness [www.laponite.com]. It has negative charges in face and small amount of positive charges in the edge.

When Laponite powder is dispersed in water, it may form disc-shaped particles with size of 25 nm in diameter and 0.92 nm in thickness (Fig. 4.1b from www.laponite.com). The crystal surface has negative charges of 70-100 mmol/100g, whereas the edge has small localized positive charges of 4-5 mmol/100g generated by absorption of hydroxyl groups where the crystal structure terminates. The sodium ions are held in a diffuse region on both sides of the dispersed Laponite crystal, which are known as electrical double layers (Fig. 4.1a). The addition of polar compounds in solution (e.g., simple salts, surfactants or additives etc.) will reduce the osmotic pressure, which causes the electrical double layer thinner and allows the weaker positive charges on the edge of the crystals to interact with the negative surfaces of adjacent crystals. This process may continue to form a “house of cards” structure, as shown in Fig. 4.2 [Dijkstra, Hansen and Madden, 1997; 1995].

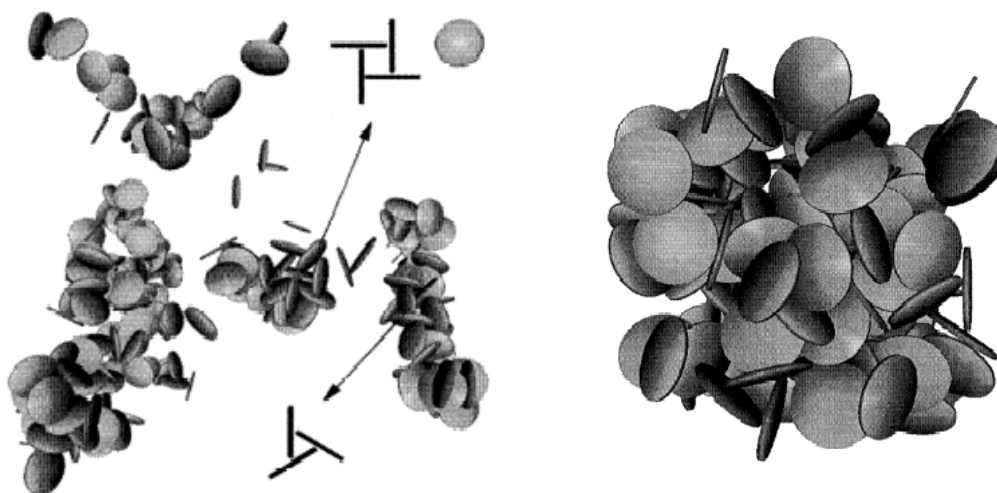


Fig. 4.2 Typical configurations of “house of cards” with increased concentration from left to right. Typical three- and four-platelet rings are schematically shown as insets; arrows point to such rings occurring within the clusters [Dijkstra, Hansen and Madden, 1997; 1995].

Besides of the effect of electrolytes, Laponite suspensions show also dependences on concentration and time [e.g., Nicolai et al., 2001; Kroon et al., 1998]. They are stable up to volume fraction of 0.4 %, above which they age slowly in time, ultimately forming thixotropic gels [Martin, 2002; Pignon, 2000; 1998; 1997; 1996]. Laponite suspensions are of great importance in many industrial applications because of the gelation [Mori, 2001].

Owing to its high purity, small size and unique shape, Laponite, as a nano-sized rigid disc-shaped model system, received great interests of experimental and theoretical

investigations in the last few years. Experimentally, several different analytical techniques are employed to explore Laponite properties in aqueous solution. Among them, small angle X-ray (neutron) scattering and static light scattering are proved to be the most suitable and powerful methods to characterize the structure of single Laponite particles and the correlation state. Ramsay et al. [1993; 1990; 1986] investigated the particle structure in aqueous solutions at low ionic strength ($I_S = 1$ mM) by means of static and dynamic light scattering and small angle neutron scattering. The weight average molecular weight $M_W = 7.1 \times 10^5$ g/mol and hydrodynamic radius $R_H = 11$ nm were determined, which lead to qualitatively the diameter of circular discs of about 30 nm and thickness of 1 nm. Kroon and Vos et al. [1998, 1996] reported a more quantitatively description of the structure of single particles by fitting the experimental scattering function with platelet model. A polydispersity for the radius of platelet was assumed to be 32% in Gaussian distribution function. This is the first time that a high polydispersity for Laponite particles in radius is supposed, before that the synthesized clay particles are believed to be almost monodispersed. However, the treatment of scattering intensity measured at volume fraction of 0.39% as form factor of Laponite particles seems too rough. Very recently atomic force microscopy (AFM) was employed to view directly the local size and shape information of Laponite colloids by Balnois and Levitz et al. [2003]. Images of laponite particles deposited on mica reveal that the particles are mainly present as individual particles. The important result deduced from AFM is that individual Laponite particles are concluded not circular discs but quite like ellipses with a height of 1 nm and major lateral dimensions of 23.5 nm. The obtained structure parameters are simulated and compared with experimental data from SANS, and show relatively good agreement between them.

The correlation state of Laponite particles in aqueous solution, including of both concentration effect and salt effect, has been studied at low q range by light scattering experiments. A strong increase of the scattering intensity at low q values are observed in many experimental investigations [e.g., Kroon, 1998; Morvan, 1994; Pignon, 1997; Mouchid, 1995], which has been attributed to the presence of large structures. For dilute solutions the strong upturn of intensity at low q values has been found to disappear after filtration through 0.45 μm or 0.22 μm pore size filters, without changing the scattering intensity significantly [Nicolai and Cocard, 2000; Bonn et al., 1999; Rosta and von Gunter, 1990]. The origin of the strong upturn at low q is therefore due to the presence of small amount of very large particles which come from the non-complete dispersion of Laponite particles but can be filtered out. These phenomenon implies that the observed “fractal

structure” is in fact an artifact, which leads to the conclusion that Laponite solutions form colloidal glasses instead of gels, according to the opinion of Bonn et al. [Abou et al., 2001; Bonn et al., 1999; 1998], since the characteristic for a gel state is its appearance at low volume fractions due to the presence of a network that may be fractal. On the other hand, the glass state is obtained at high volume fractions of particles, and there is no network present.

With increase of particle concentration, although which is still very low for normal colloids, Laponite solutions undergo liquid-solid transitions. Despite of a lot of experimental and theoretical investigations, the status and the origin of these transitions (e.g., “house of cards” structure [Dijkstra, Hansen and Madden, 1997; 1995]; Wigner glass transition [Abou et al., 2001; Bonn et al., 1999; 1998], nematic transition [Lamaire and Davidson et al., 2002; Rowan and Hansen, 2002; Porion and Delvilli et al., 2001; 1998]) are still matter of controversy.

The motivation of this study is using a combination of light scattering and small angle X-ray scattering techniques to investigate the size, shape and correlation state of Laponite particles in a large magnitude of q value. The difference of the present work from literature lies in that it focused on very dilute Laponite solutions where, the form factor $P(q)$ of Laponite particles is allowed to be yielded more accurately. In addition, the experimental structure factors $S(q,c)$ as function of concentration and scattering vector q ($S(q,c)=I(q,c)/P(q)$) were obtained, from which the effective diameter d_{eff} of interaction of Laponite particles was obtained for the first time which represents the strength of interparticle interaction. Another aim of the present work is the comparison of the experimental structure factor with the newly developed theory of Harnau et al. [Harnau et al., 2002; 2001; Kutter, Hansen et al., 2000], which has been demonstrated to be successful in explaining neutron scattering measurements on an isotropic suspension of Laponite platelets at 6.5% w/w [Ramsay, 1993], although it is still under debate if the suspension can be treated as isotropic at such a high weight percentage. Only based on the correctly evaluated form factor and structure factor for Laponite suspensions in dilute particle density, the perspective experimental and theoretical investigations on more concentrated suspensions for study of the origin of sol-gel transition could be meaningful.

4.2 Sample preparation

Laponite RD with a structure as shown in Fig. 4.1 is obtained from Laporte Industries Ltd. The dispersions are prepared as follows: The Laponite powder is added to a 10^{-3} mol/l NaCl solution in distilled water and mixed at high speed with a magnet stirrer for 4 hours. Laponite dispersed rapidly in water without heating. The solution is initially turbid, but becomes clear in 15-20 minutes, indicating that the particles are fully hydrated. The primary high speed is necessary for dispersing particles homogeneously and to avoid aggregation. The SAXS data of samples prepared in different ways were compared in Fig. 4.2. The relative higher scattering intensity at low q obtained from sample by gentle shaking may due to some large-sized clusters. The pH values of all the samples were adjusted to 10 by using NaOH in order to avoid degradation or dissolution of Laponite particles. Thomson and Butterworth [1992] reported that a significant dissolution of magnesium silicate happened at pH value lower than 7 but not at pH above 9.

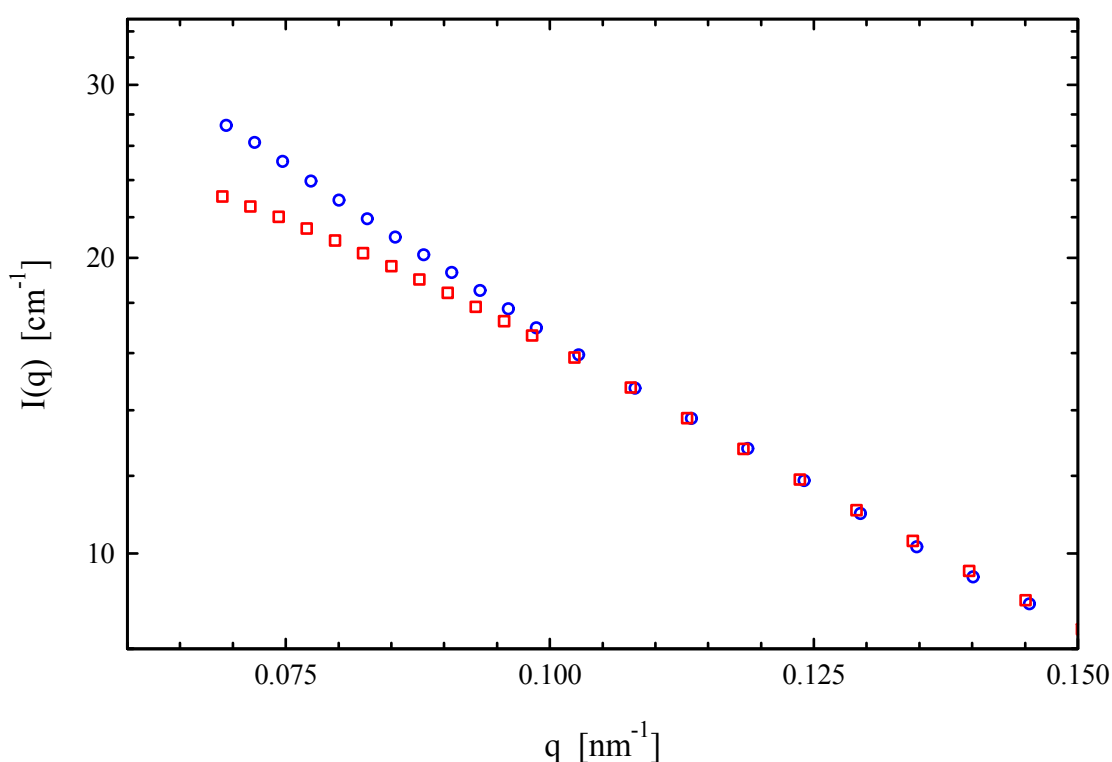


Fig. 4.3 Comparison of scattering intensities of samples prepared by different ways. Squares: vigorous stirring; circles: gentle shaking.

Dispersions were kept still overnight before any use in order to achieve equilibrated state. Dispersion samples were measured by SAXS without further treatment since no difference is observed between the scattering intensities of unfiltered dispersion and filtered one by using 0.22 μm filters (Millipore). The volume fractions ϕ of measured Laponite dispersions range from 0.02% to 0.16%, is dilute enough to allow performing concentration extrapolation. SAXS measurements were performed using both ID2 in ESRF, Grenoble, France and Kratky camera in our lab to get scattering intensity in a q range from 0.02 to 6 nm^{-1} . Static light scattering were performed by a Sofica SLS-Spectrophotometer, using vertically polarized light with a wavelength of 633 nm. Dispersions were filtered by using 0.22 μm filters (Millipore) into quartz cuvettes to eliminate dusts. Both Bonn et al. [1999] and Nicolai [2000] observed big difference of light scattering intensity of samples with and without preliminary filtration by using Millipore filters. A power law dependence of scattering intensity with slope between -1 and -3 was shown for not filtered sample which was attributed to the small amount of large size aggregations, whereas for filtered sample no q dependence was observed.

The mass density of the particles in aqueous solution was measured to be $2.42 \pm 0.12 \text{ g/cm}^3$, which is some smaller literature value of 2.57 g/cm^3 for Laponite powder [e.g. Pignon, 1997; Nicolai, 2001], is however easily to be understood because of the solvent effect.

4.3 Experimental form factor and determination of size and shape of Laponite particles

In order to get experimental form factor, the scattering intensities of samples with a concentration serial in dilute region were measured. They were then normalized to their concentration and the effect of concentration exists in low q region, which can be illuminated by extrapolation of concentration according to eq. (2.28). By combination of scattering data from static light scattering and small angle X-ray scattering (synchrotron and Kratky camera), the experimental form factor $P(q)$ of Laponite particles has been obtained in almost three orders of magnitude of the scattering vector q ($0.009 - 6 \text{ nm}^{-1}$).

As results from static light scattering, Fig. 4.4 shows the Rayleigh ratios $R_\theta(q, \phi)$ as a function of θ (35-125 $^\circ\text{C}$) or q ($0.009-0.024 \text{ nm}^{-1}$) (eq. (2.1)) at five different volume fractions, which show no obvious dependence on q , i.e., $P(q) \approx 1$.

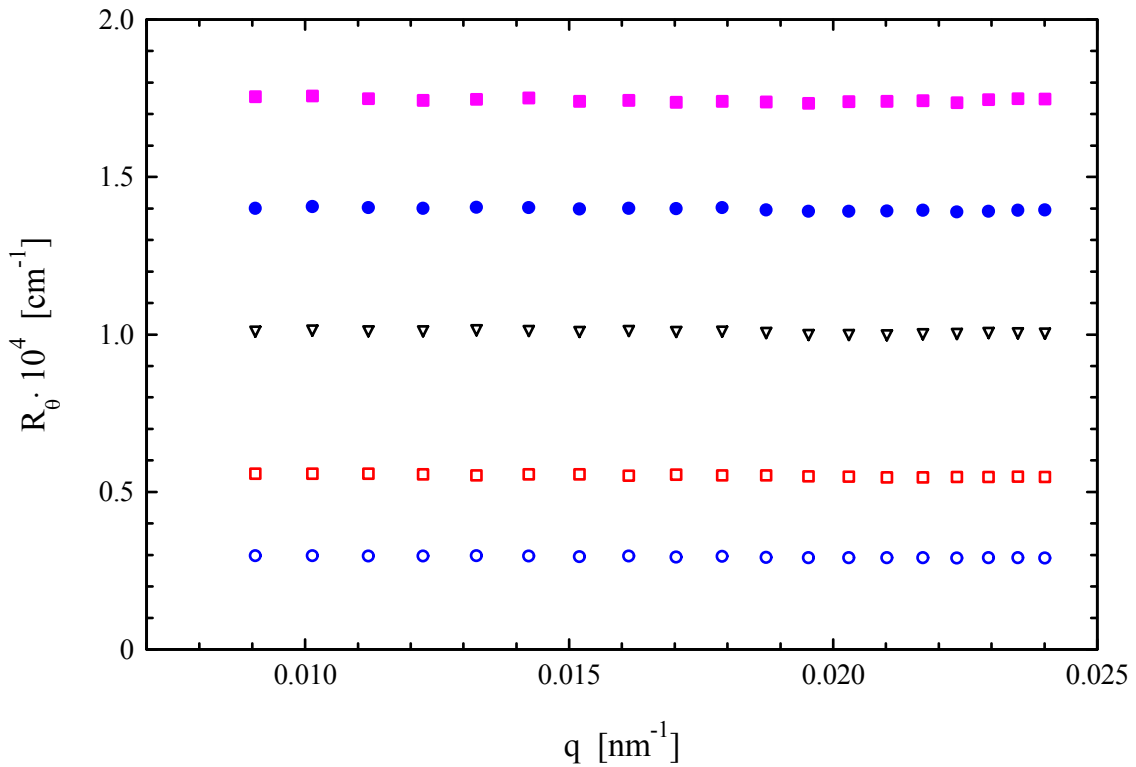


Fig. 4.4 Rayleigh ratio $R_{\theta}(q)$ as function of the scattering vector q for Laponite dispersions at volume fractions of 0.02 % (circles), 0.04% (squares), 0,08% (triangles), 0.12% (filled circles) and 0.16% (filled squares).

The term $Kc/R_{\theta}(q)$ were extrapolated to vanishing concentration for every q , according to Rayleigh-Debye function (eq. 3.7). The extrapolated scattering intensities are shown in Fig. 4.6 for the SLS part, after corrected by a factor of K_{SAXS}/K_{LS} . K_{SAXS} and K_{LS} are optical constants for SAXS and light scattering, respectively. For the investigated samples, the refractive index increment dn/dc was experimentally obtained to 0.083 ± 0.008 ml/g which yields a value of $(4.99 \pm 1.00) \times 10^{-8}$ $\text{cm}^2 \cdot \text{mol}/\text{g}^2$ for the optical constant K_{LS} (eq. (3.8)), whereas K_{SAXS} is calculated to be 0.04454 mol/g^2 (eq. (2.23)).

For synchrotron SAXS experiments the scattering intensities have been at first normalized to the volume fractions, as shown in Fig. 4.5. The inset there shows the extrapolation of concentration for q from 0.025 to 0.180 nm^{-1} , where the effect of interparticle interaction exists. For q higher than 0.180 nm^{-1} , the scattering intensity of sample with different volume fraction has no concentration dependence which means that the structure of one single particle does not change with concentration. The extrapolated

scattering intensity (solid chain) is then shown also in Fig. 4.5 for the SAXS part from synchrotron (q : 0.025-0.6 nm^{-1}).

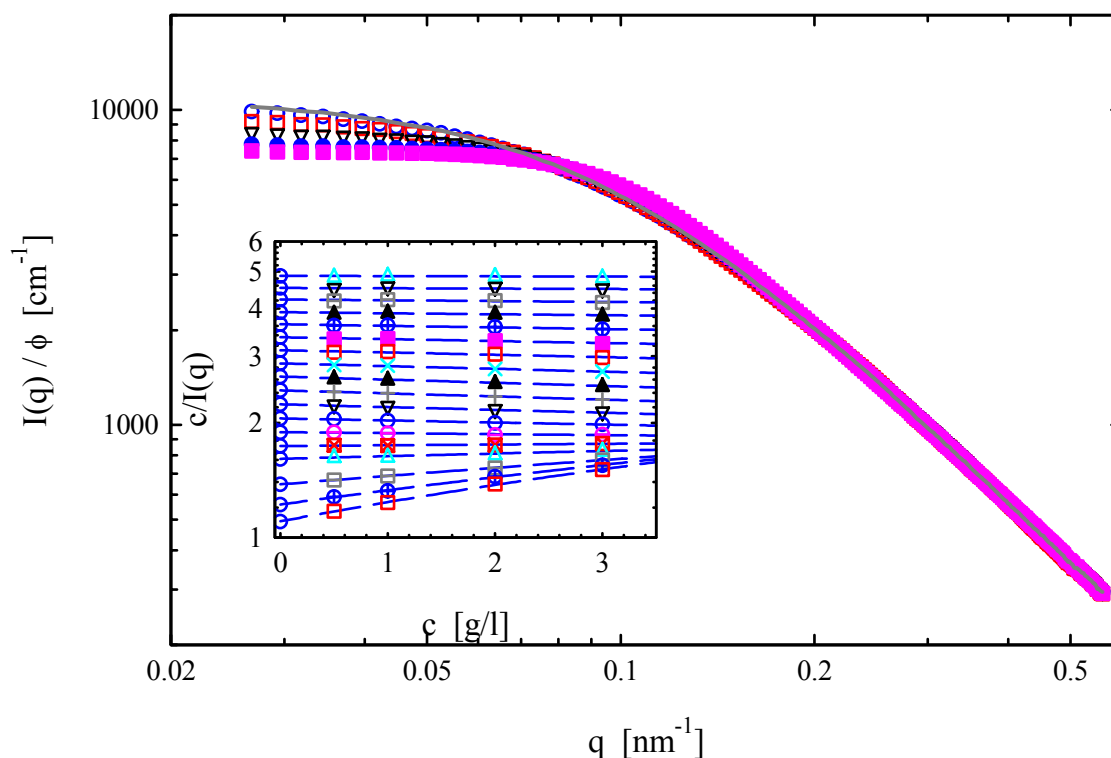


Fig. 4.5 Absolute scattering intensities of Laponite dispersions normalized to their volume fractions at 0.02 % (circles), 0.04% (squares), 0.08% (triangles), 0.12% (filled circles) and 0.16% (filled squares). Solid line: extrapolated data ($\phi \rightarrow 0$) as obtained shown in inset.

The last part of data in Fig. 4.6 were obtained by performing Kratky-Compact-Camera. In this q region (0.2-6 nm^{-1}) the scattering intensities are identical for different volume fractions, after normalized to the concentrations, i.e., the obtained scattering intensity is already form factor for this part.

The form factor in all experimental q range (0.009-6 nm^{-1}) is thus obtained and shown in Fig. 4.6. From the form factor the following conclusion can be achieved: First, the absolute scattering intensities obtained from three different techniques are coincide with each other in the limit of experimental error of $\pm 5\%$, which demonstrates that the experimental and data treatments have been successful. As second, in low q region (0.009-0.025 nm^{-1}) the scattering intensity is independent of the scattering vector, showing no power law decay, which implies a good dispersion of particles without aggregation or clusters in large scale (this q region corresponds to scale of 250-700 nm, according to factor of $2\pi/q$). Thirdly, in

the intermediate q region the scattering intensity follows a q^{-2} power law decay (see inset in Fig. 4.6), which demonstrates that the investigated particles are platelets [Glatter & Kratky, 1982], the thickness of platelets can be therefore determined to be 0.9 nm by the slope of the linear regression shown in inset of Fig. 4.6, according to eq. (2.26). Finally, the average molecular weight M_W and radius of gyration R_g of Laponite particles in aqueous solution may be determined by applying Guinier-law to the form factor, which is resulted to 930 ± 190 kg/mol and 13.4 nm, respectively. The obtained M_W is greater than 710 kg/mol by Avery and Ramsay [Avery, 1986], 640 kg/mol by Bhatia [2003]. This point will be discussed below with fitting parameters.

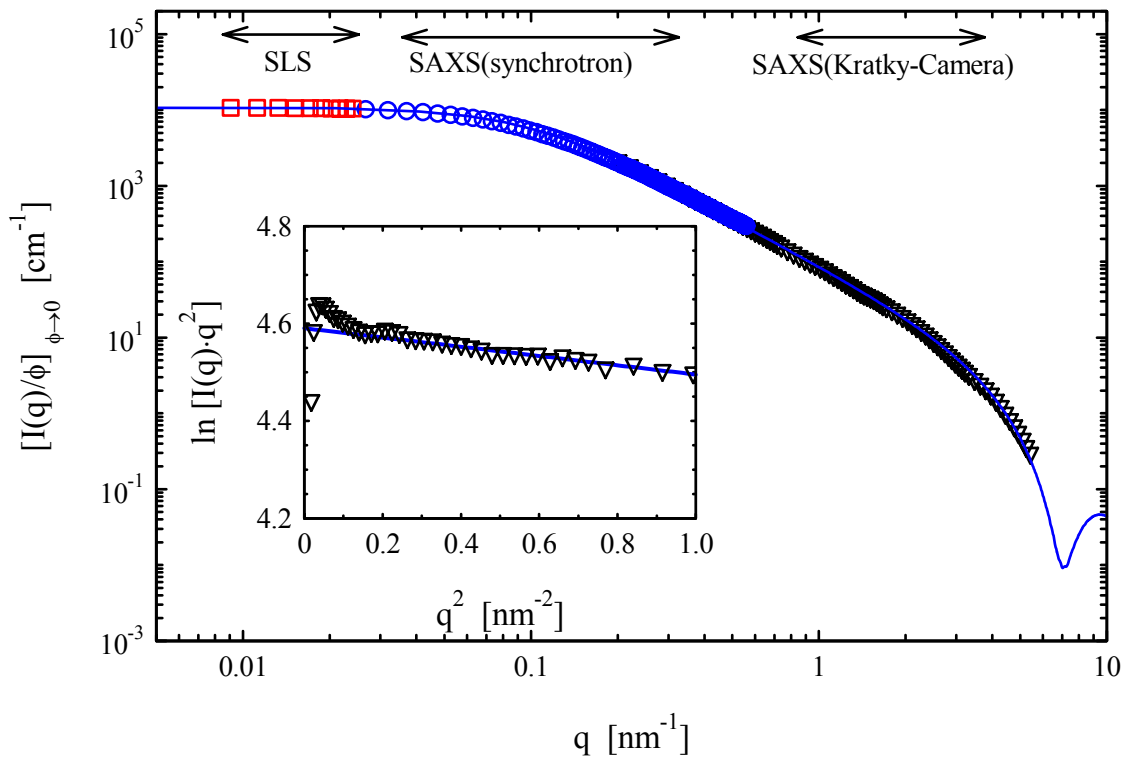


Fig. 4.6 Form factor of Laponite particles in aqueous solution (ionic strength $I_S = 1$ mM) at full experimental q region, which is composed of: static light scattering (squares), small angle X-ray scattering (SAXS) from synchrotron (circles) and Kratky camera (triangles). The scattering intensity at intermediate region obeys a q^{-2} scaling law, which demonstrates that the investigated particles have disc shape. The solid line is the model curve of discs with diameter of 21 nm and thickness of 0.9 nm. The polydispersity in diameter is not negligible, which is set to 1.5 ($= D_W/D_N$) in Schulz-Zimm distribution function. The inset represents $I(q)$ in the way of $\ln[I(q) \cdot q^2]$ vs. q^2 , from the linear regression the thickness of discs was determined to be 0.9 nm.

A more quantitative description about the size and shape of single Laponite particles is performed by comparing the experimental form factor with disc-shaped model. As shown in Fig. 4.6 by solid line, the model curve describes the experimental form factor in good agreement, by applying $R_W = 10.5$ nm and a polydispersity $R_W/R_N = 1.5$ in Schulz-Zimm distribution function, where R_W and R_N denote weight and number average radius of discs. It should be noted that neither monodisperse model nor polydisperse model by using Gaussian distribution function lead to an exactly agreement with the experimental form factor.

With knowledge of mass density ρ_m of Laponite particles in aqueous solution and size parameters obtained above, the weight average molecular weight for such a polydisperse discs system is calculated to be 1000 kg/mol, according to

$$\langle M_w \rangle = \frac{\sum n_i M_i^2}{\sum n_i M_i} = \rho_m V_A \pi H \frac{\sum W_i R_i^4}{\sum W_i R_i^2} \quad (4.1)$$

The calculated value is in agreement with the experimentally determined value of 930 ± 190 kg/mol, which provides another proof for the successful data treatment.

The effect of ionic strength on the correlation state of particles was studied as well. The ionic strength was set higher to 5 mM by adding NaCl. The experimental form factor, as shown in Fig. 4.7, is determined by the same way as that for $I_S = 1$ mM. For reference the form factor at ionic strength of 1 mM is plotted in the same graph as well. Obviously in this case there exists large scale structure - a network probably, which can not be filtered out any more. The power-law decay in this case are $q^{-0.5}$ and $q^{-1.5}$ instead of q^0 for $I_S = 1$ mM at the same low q region. It should be noted that the procedure of sample preparation and SLS and SAXS measurements were performed exactly the same as those at ionic strength of 1 mM.

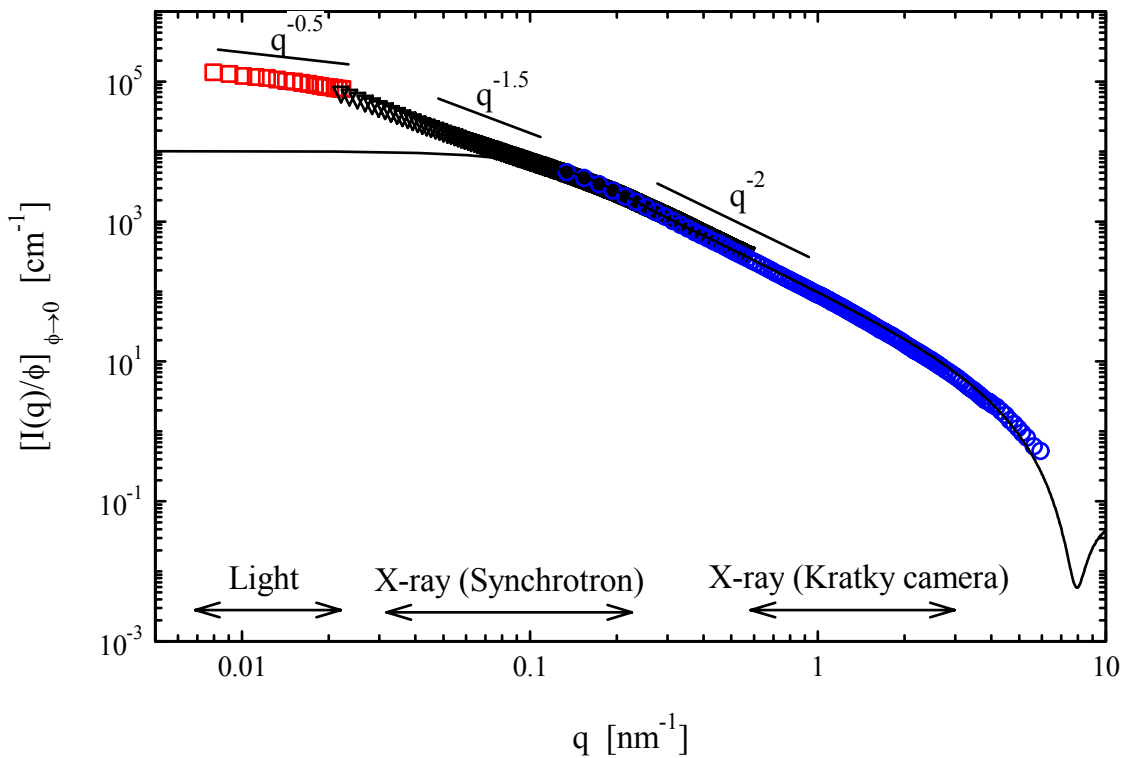


Fig. 4.7 Form factor of Laponite particles in aqueous solution (ionic strength $I_S = 5$ mM) at full experimental region, which is composed of: static light scattering (squares), small angle x-ray scattering (SAXS) from synchrotron (circles) and Kratky camera (triangles). Instead of the non-correlated state of particles at vanishing concentration at $I_S = 1$ mM, as indicated by dashed line, the particles in aqueous solution at $I_S = 5$ mM form aggregates, which is indicated by the scaling law of $q^{-0.5}$ and $q^{-1.5}$ instead of q^0 at low q range.

The appearance of large scale supramolecular structure or network shifts to lower concentration with increasing of ionic strength seems to be contrary to the classical DLVO theory [Delville et al., 1992; 1994; Israelachvili, 1985] - adding salt reduces the screening length and thus reduces the swelling pressure (Debye length $\lambda_D = 0.304/\sqrt{[NaCl]}$ nm). One explanation is based on the “house of cards” model [Mourchid and Levitz et al., 1995; Kutter et al., 2000]. With increasing of salt concentration, the positive charges in edges play a more and more important role in forming T-shaped configuration, as shown in Fig. 4.2. This T-shaped large structures are quite reversible, i.e., they can deform under pressure to pass through filter and build again very quickly in cuvette or capillary. This finding of large scale

structure for Laponite dispersion at low concentration e.g. 1 g/l and ionic strength of 5 mM is supported by the light scattering result from Nicolai et al. [Nicolai et al., 2000; 2001]. However, according to Kutter's calculation [Kutter et al., 2000] of site-site radial distribution, orientational correlation function and center-of-mass structure factor, the effect of the positive rim charges is considerably strong only at ionic strength $I_S \geq 100$ mM ($\lambda_D \leq 1$ nm).

The tendency that aggregation of Laponite Particles in aqueous solution appears at lower concentration with increasing ionic strength is in agreement with the phase diagram described by Mourchid et al. [1995], as shown in Fig. 4.8, which are detected by rheological and osmometric measurements. In reference for spherical colloids the corresponding diagram would exhibit a fluid/solid line of opposite (positive) slope [Monovoukas, 1989].

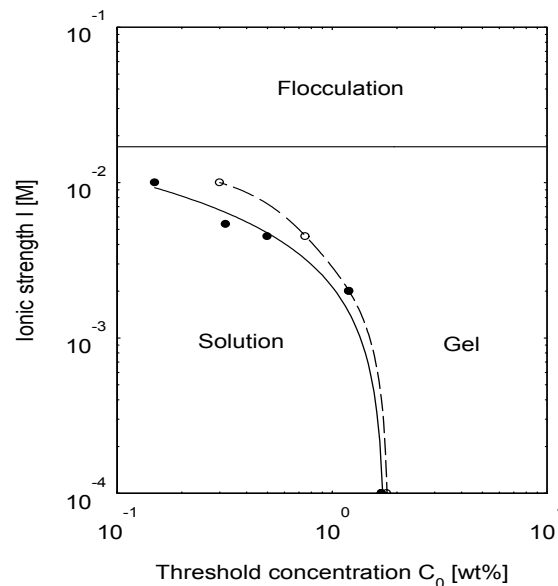


Fig. 4.8 Schematic phase behavior of Laponite suspensions, reproduced from Mourchid et al. [1995], which describes the sol/gel transition as detected by rheological (●) and osmometric (○) measurements.

4.4 Influence of finite concentration: Structure factor $S(q,c)$

4.4.1 Apparent virial coefficient B_{app}

The apparent virial coefficient B_{app} , which reflects the interparticle interactions, as represented in eq. (2.51), will be discussed at first. According to eq. (2.54), B_{app} can be determined from the diagram of extrapolation of concentration (see inset of Fig. 4.5: $\phi/I(q) \sim \phi$) for each q value. Such resulted B_{app} is plotted in Fig. 4.9 as function of q^2 . According to eq. (2.55), this function should show a linear regression at low q region and it is does fulfilled, as shown in Fig. 4.9. From the linear fitting $d_{eff} = 46$ nm and $V_p = 1360$ nm³ were obtained.

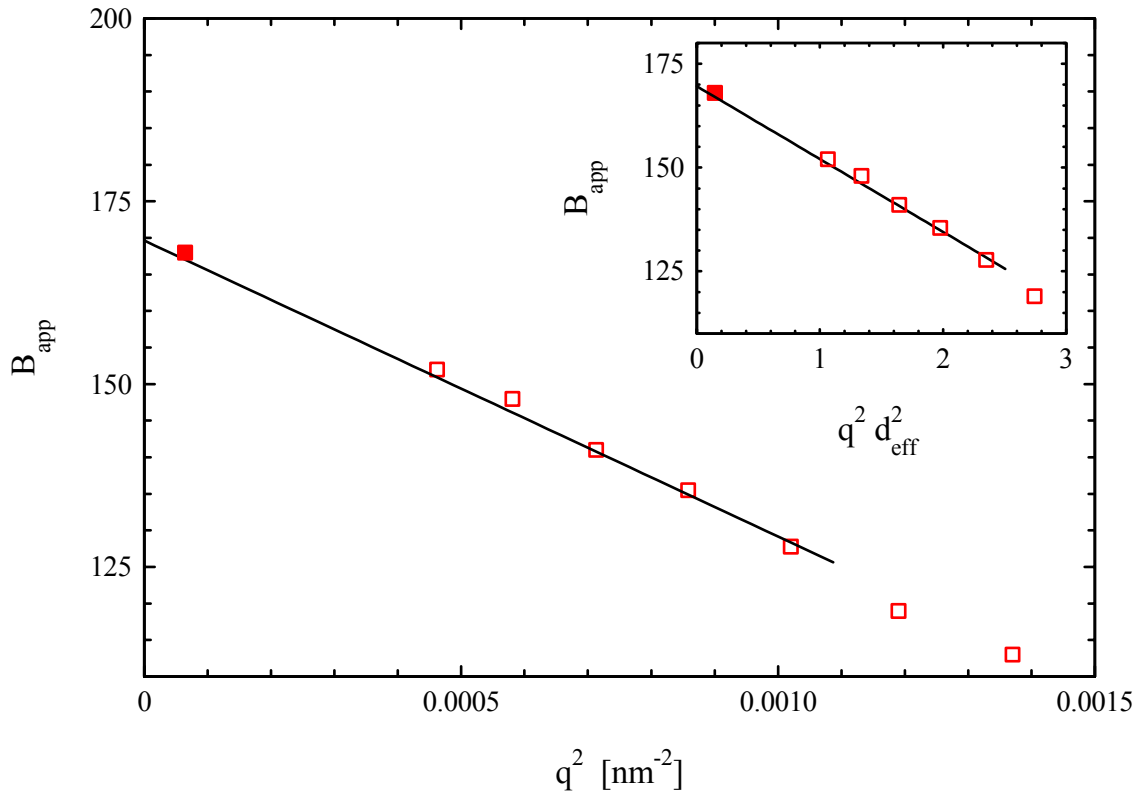


Fig. 4.9 B_{app} as function of q^2 obtained from diagram of extrapolation of concentration, according to eq. (2.54). The diamond point was obtained by SLS and the rest signals by SAXS. From the linear fitting d_{eff} and V_p were determined to be 48 nm and 1360 nm³, respectively, according to eq. (2.55). The inset represents B_{app} as function of $q^2 d_{eff}^2$ to provide validity proof for eq. (2.55). In this case the second term in eq. (2.55) equals to 0.2, which is smaller than unity - the first term, so the higher term can be neglected.

As mentioned in chapter 2.3.1, d_{eff} corresponds to the minimum distance to which two particles may approach each other, which equals to $2R_g$ for hard spheres. Here the obtained d_{eff} is obviously much larger than the actual size of Laponite particles ($2R_g \approx 27$ nm) which may be due to the strong electrostatic repulsive interaction between charged particles. Rowan and Hansen [Rowan and Hansen, 2002] have discussed this parameter for charged rods and disc-shaped particles. According to them, d_{eff} should be the sum of the bare diameter plus a contribution from the double layer, which is roughly proportional to the Debye length λ_D . So if the electrostatic repulsion is the true reason for $d_{eff} \gg 2R_g$, this value should decrease with adding salt. However, it is unfortunately that this effect can not be checked experimentally since some kind of aggregations appear with the addition of salt. For instance, as shown in Fig. 4.7, the form factor of Laponite particles shows a strong upturn in low q region at $I_S = 5$ mM which implies the appearance of large scale structures. The simultaneously obtained V_P is therefore an effective particle volume, which should be termed in this case as V_{eff} , corresponding to the effective diameter d_{eff} ($V_{eff} = \pi(d_{eff}/2)^2 H = 1490$ nm³). The actual particle volume $V_P = 310$ nm³, calculated by platelet model with $D_W = 21$ nm and $H = 0.9$ nm.

4.4.2 Structure factor and consistency check

The structure factor $S(q,c)$ as function of concentration and scattering vector q were obtained from the scattering intensity at finite concentration divided by the scattering intensity at vanishing concentration (eq. (2.56)), as shown in Fig. 4.10. These experimental data are composed by two techniques: static light scattering (q : 0.008-0.024 nm⁻¹) and small angle X-ray scattering (q : 0.025-0.200) in synchrotron. The ionic strength of solutions is 1 mM. The data captured from the two techniques are coincide with each other. Since the deviation from unity represents the strength of inter particle interaction, it is obvious that at the investigated volume fraction range 0.02-0.16% the interparticle interactions in low q region must under no circumstances be neglected. In this case we may not agree with some literature work, e.g., Kroon and Vos et al. [1998] measured the scattering intensity of one Laponite dispersion at volume fraction of 0.39% and treated this data directly as form factor to get structural information of Laponite particles. Fig. 4.10 shows that the interaction becomes stronger with increasing concentration. In addition, a significant maximum in the experimental structure factors was observed at scattering vector of ca. 0.12 nm⁻¹ for samples of volume fraction larger than 0.12%.

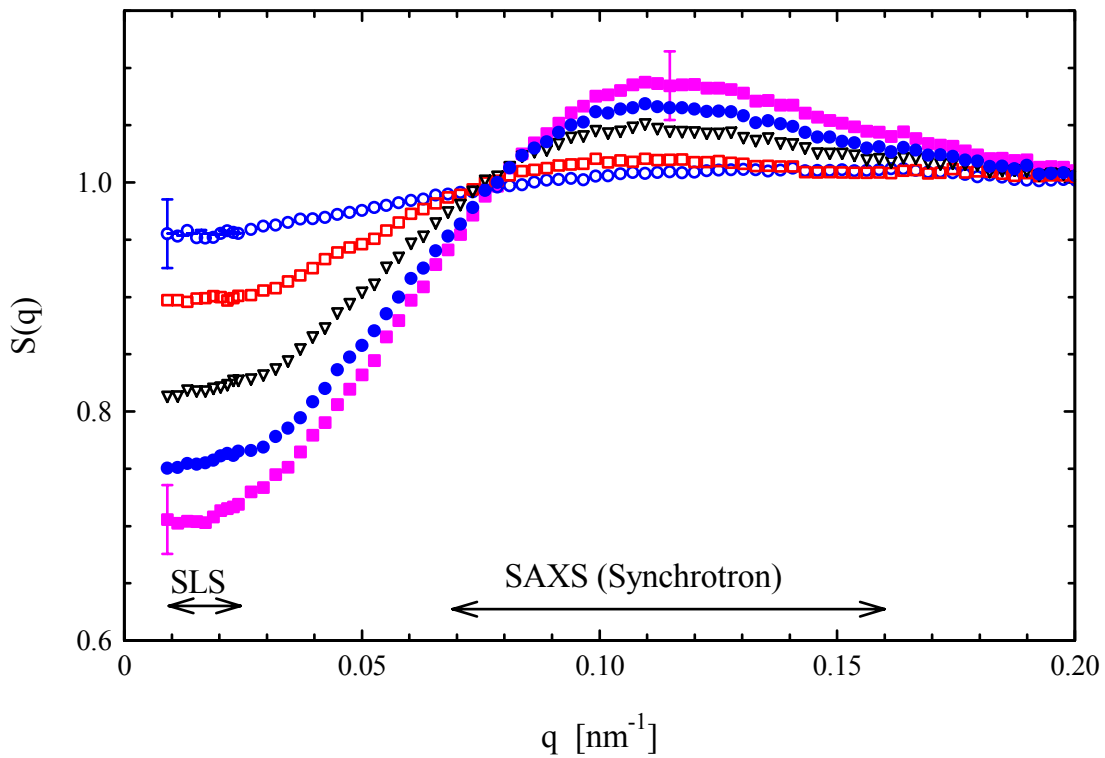


Fig. 4.10 Structure factor $S(q,c)$ of Laponite particles in aqueous dispersions as function of q at volume fraction of 0.02% (circles), 0.04% (squares), 0.08% (triangles), 0.12% (filled circles) and 0.16% (diamonds). Every curve is combined by experimental data from static light scattering and small angle X-ray scattering.

For the experimental determined structure factor $S(q,c)$ in the dilute regime, eq. (2.54) and (2.55) may be used to check whether these sets of data is consistent [Rosenfeldt, 2002]. Hence, plots of $1/S(q,c)$ versus q^2 for different volume fractions must be linear for low q and the effective diameter of interaction d_{eff} can be obtained from the slope of the linearly fit. This assumption is indeed the case for all volume fractions investigated in this study, as shown in Fig. 4.11, where $d_{eff} = 46 \pm 2$ nm and $V_P = 1430 \pm 80$ nm³ were obtained consistently for all the five volume fractions. These values agree well with the result from Fig 4.9, where $d_{eff} = 48$ nm and $V_P = 1360$ nm³.

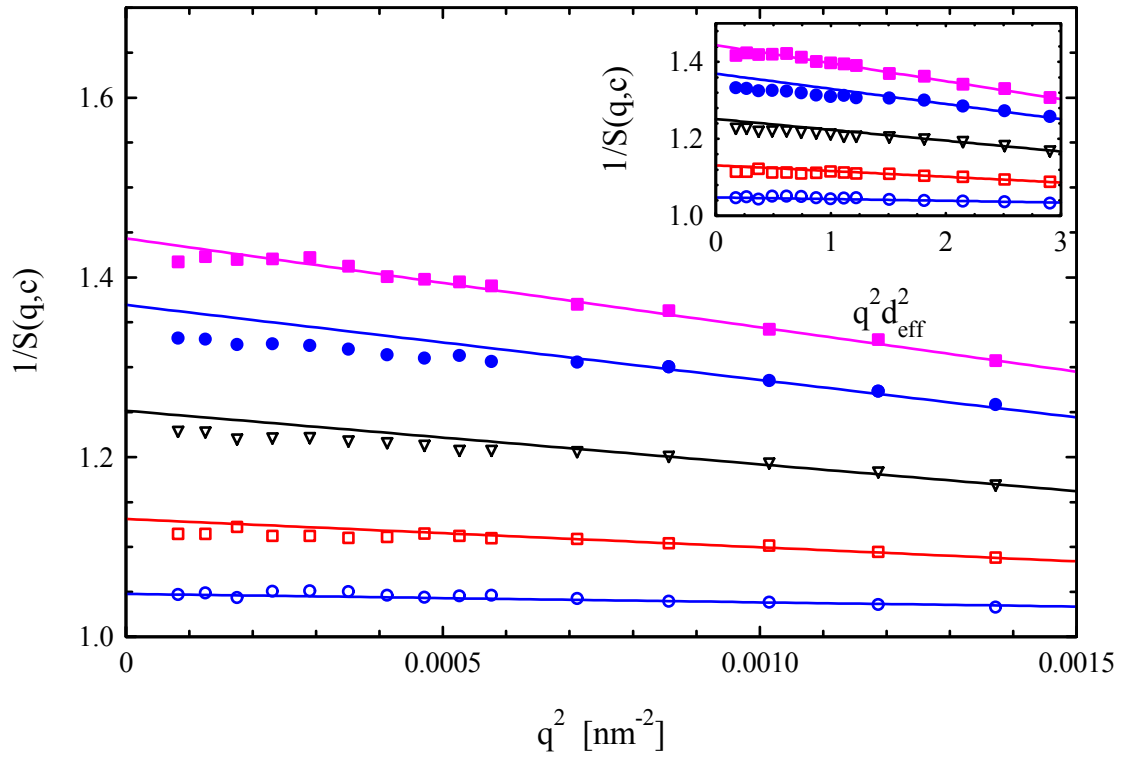


Fig. 4.11 Consistency check of structure factor $S(q)$ by plotting $1/S(q)$ vs. q^2 at volume fraction of 0.02% (circles), 0.04% (squares), 0.08% (triangles), 0.12% (filled circles) and 0.16% (diamonds). From the linearly regressions $d_{eff} = 46 \pm 2$ nm is obtained consistently from all five volume fractions, according to eq. (2.54) and (2.55). Volume of one particle V_p is resulted simultaneously to be 1430 ± 80 nm³, which is much larger than the actual volume of one particle (310 nm³) but equal to the volume of discs with effective diameter of d_{eff} ($V_{eff} = \pi(d_{eff}/2)^2 H = 1490$ nm³). The inset represents $1/S(q,c)$ as function of $q^2 d_{eff}^2$ to provide validity proof for eq. (2.55). In this case the second term in eq. (2.55) equals to 0.3, which is smaller than unity-the first term, so the higher term can be neglected.

With the obtained d_{eff} , one may describe the consistency check by plotting $1/S(q)$ versus $\phi d_{eff}^2 q^2$, shown in Fig. 4.12. As expected, this set of data follow with the same slope of $2\pi d_{eff}^3 / (15V_p)$, which shows an internal consistency of the data.

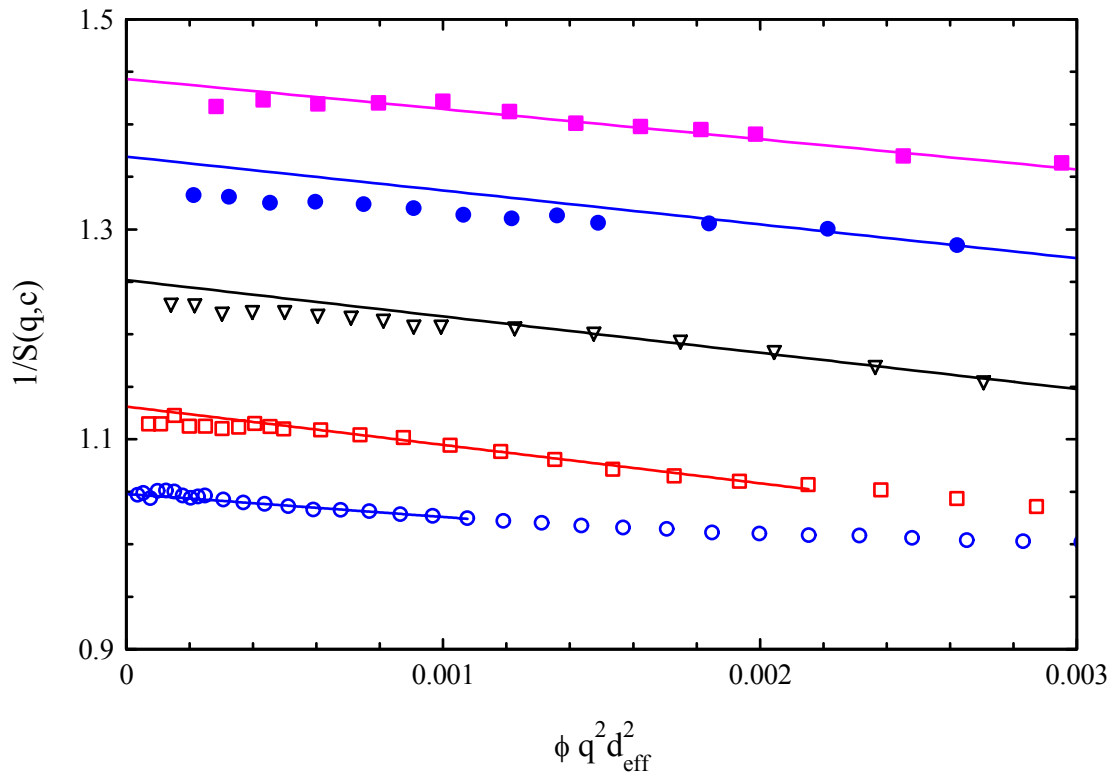


Fig. 4.12 Consistency check of structure factor $S(q,c)$ by plotting $1/S(q)$ vs. $\phi q^2 d_{\text{eff}}^2$ at volume fraction of 0.02% (circles), 0.04% (squares), 0.08% (triangles), 0.12% (filled circles) and 0.16% (diamonds). All the data sets follow a slope of $2\pi d_{\text{eff}}^3/(15V_P)$ which demonstrates an internal consistency of the data.

The other consistency check is based on the expanded formation of $S(q,c)$ [Jansen 1986; Apfel 1994]

$$S(q) = S(0) + \alpha q^2 + O(q^4) \quad (4.2)$$

where α is a coefficient which is related to the effective diameter of interaction d_{eff} and its volume fraction. This expansion is only valid at small αq^2 but allows $S(0,c)$ to be extrapolated in a model-free manner. For a system of hard spheres, α and $S(0,c)$ can be calculated in the frame of Percus-Yevick theory which is compared with experimental data from dissolved dendrimer in detail by Rosenfeldt et al. [Rosenfeldt, 2002]. However, here for charged discs system this procedure is not performable due to lack of a theoretical model.

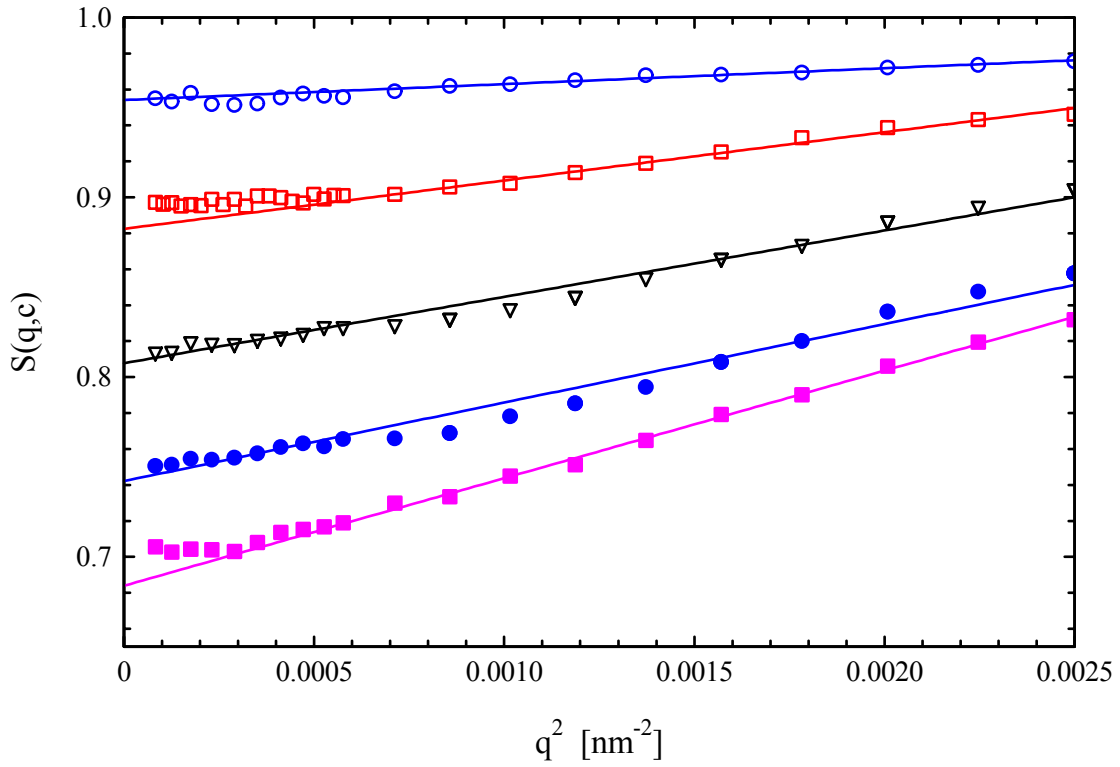


Fig. 4.13 Consistency check of $S(q,c)$ in the low- q regime according to eq. (4.2): $S(q,c)$ versus q^2 at volume fraction of 0.02% (circles), 0.04% (squares), 0.08% (triangles), 0.12% (filled circles) and 0.16% (diamonds). From the intercept and slope of the linear regressions fig. 4.14 is plotted.

Fig. 4.13 displays the dependence of $S(q,c)$ on q by plotting $S(q,c)$ versus q^2 , which shows linearly regression at low q for all the investigated volume fractions. Moreover, this expansion also suggests that all data should collapse on a single master curve if $S(q,c) - S(0,c)$ is plotted versus αq^2 . Such transformed data were represented in Fig. 4.14, all data fall on a universal line of $y = x$ if αq^2 is small enough.

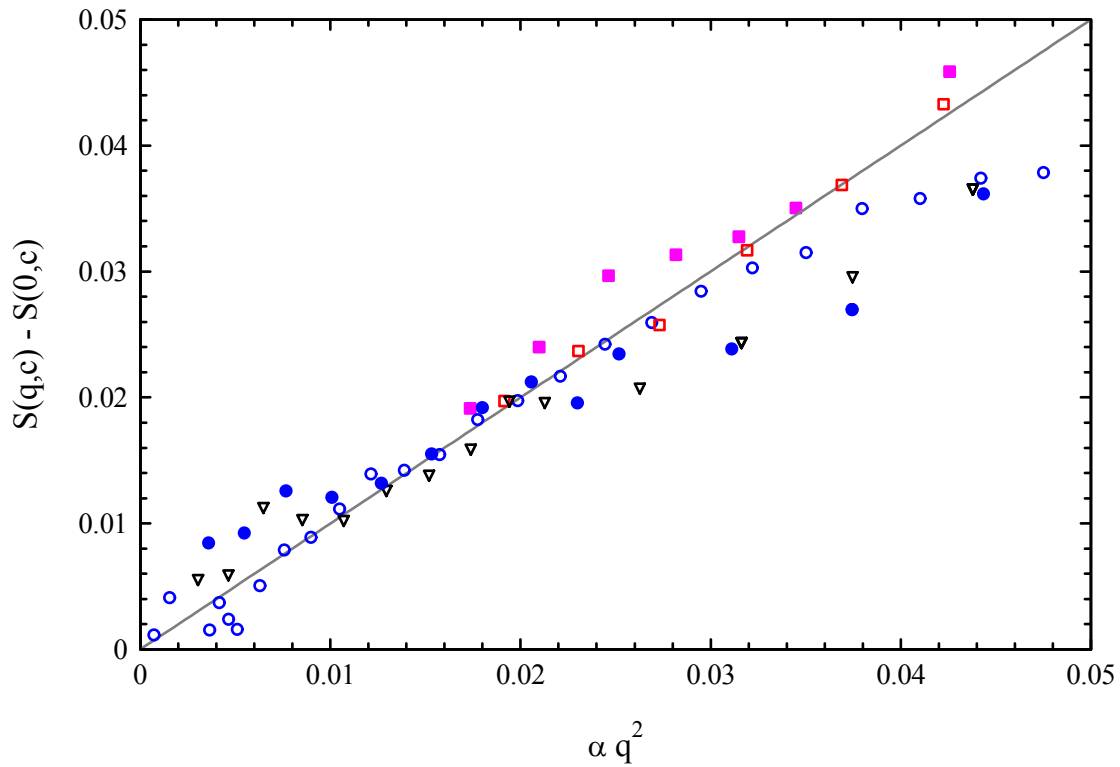


Fig. 4.14 Consistency check of $S(q,c)$ according to eq. (4.2): $S(q,c) - S(0,c)$ vs. αq^2 at volume fraction of 0.02% (circles), 0.04% (squares), 0.08% (triangles), 0.12% (filled circles) and 0.16% (diamonds). $S(0,c)$ and α for different volume fractions have been obtained from the linear regressions in fig. 4.13, respectively.

4.4.3 Comparison of experimental structure factor with multicomponent interaction site model

Besides of the above internal consistency check, the experimental determined structure factors were also compared with the multicomponent interaction site model. All the model calculations were performed by Harnau. The detail about the multicomponent interaction site model can be found in section 2.3.2 of this work or Harnau et al., 2001; Kutter et al., 2000.

In the model calculations three sets of parameters have been used, namely those related to the geometry of an individual platelet, those related to the polydispersity in the size of the platelet, and those related to the potential of interaction. The former two sets of parameters have been determined by fitting the experimental form factor (see section 4.3). The only

adjustable parameter is the potential of interaction, which has been varied in Harnau's simulation from a simple screened Coulomb interaction to the DLVO interaction, i.e., an attractive interaction is also paid attention.

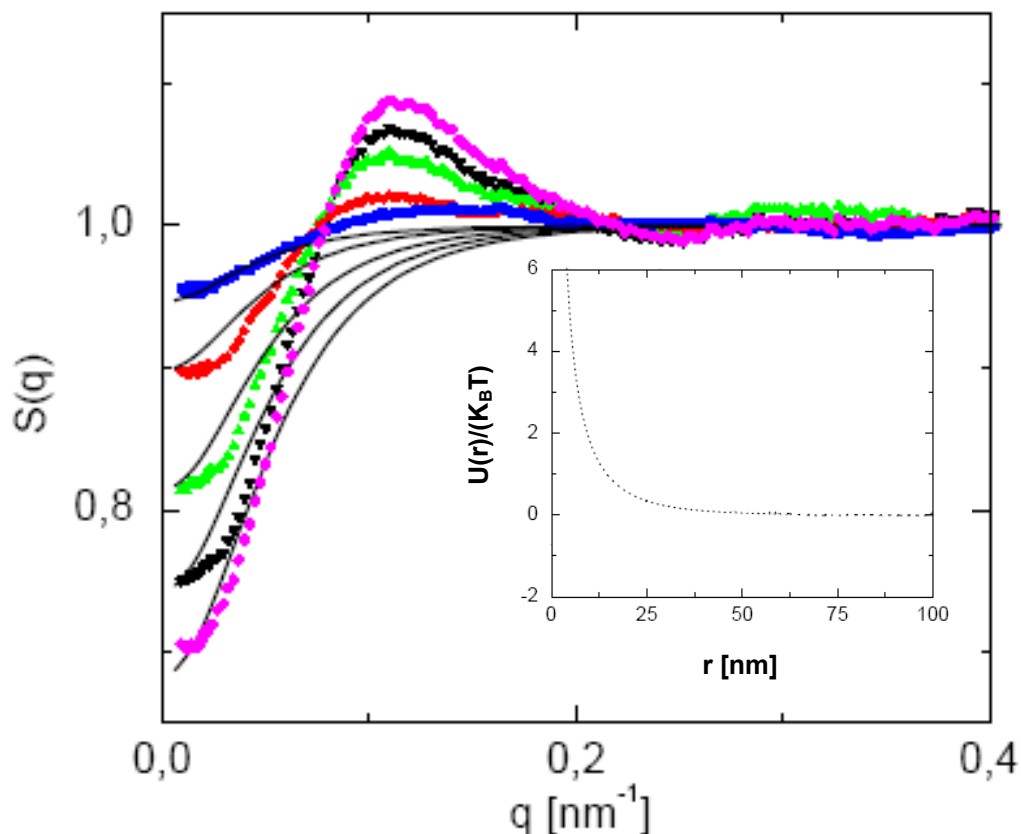


Fig. 4.15 Comparison of experimental structure factor $S(q,c)$ at volume fraction of 0.02% (blue), 0.04% (red), 0.08% (green), 0.12% (black) and 0.16% (purple) to theoretical predictions respectively (solid lines). The inset represents the profile of interaction potential, with whose help the structure factors were calculated.

From the comparison of the experimental data with model calculations, as shown in Fig. 4.15 and 4.16, it is obvious that the effective potential of interaction is the decided parameter. Besides of the screened Coulomb interaction, only when an attractive interaction is also paid attention, the experimental determined structure factors can be predicted successfully by the present multicomponent interaction site model. The attractive interaction may arise from the attractive van der Waals interaction or from the electrostatic attraction of negative charged surfaces and positive charged edges of Laponite platelets.

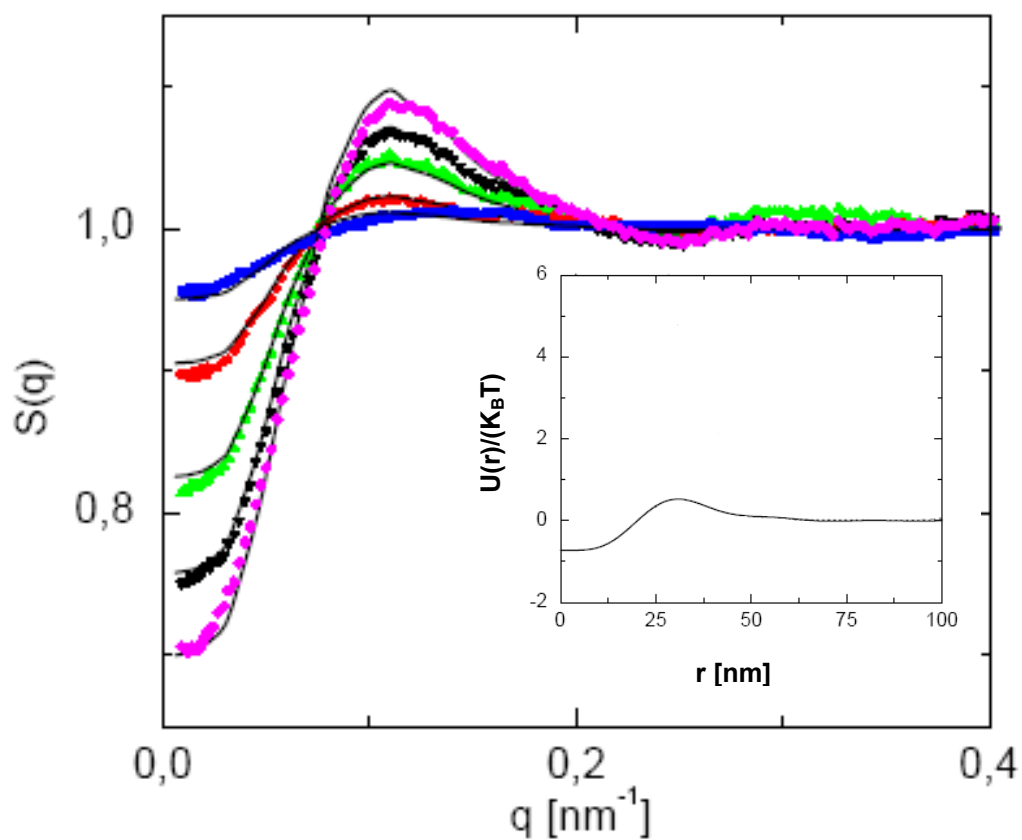


Fig. 4.16 Comparison of experimental structure factor $S(q,c)$ at volume fraction of 0.02% (blue), 0.04% (red), 0.08% (green), 0.12% (black) and 0.16% (purple) to theoretical predictions respectively (solid lines). The inset represents the profile of interaction potential, with whose help the structure factors were calculated.

4.5 Conclusion

With combination of static light scattering and small angle x-ray scattering the form factor $P(q)$ of Laponite particles in aqueous solution was obtained through extrapolation of concentration in a large q range from 0.007 to 6 nm⁻¹, which corresponds to characteristic distances ranging from a nanometer to almost a micrometer. In low q range the scattering intensity show no obvious dependence on q , i.e., $P(q) \approx 1$, which implies a good dispersion of particles without aggregation or clusters in large scale. In the intermediate q range, the scattering function falls down with a q^{-2} -scaling law which implies the shape of single Laponite particles in aqueous solution is platelet. From the Guinier thickness plot ($\ln[I(q) \cdot q^2] \sim q^2$) the thickness of one single platelet was determined to be 0.9 nm. The weight average molecular weight and radius of gyration were determined to be 930 ± 190 kg/mol and 13.4 nm, respectively, according to Guinier law. Through fitting with platelet model the weight average radius of an individual platelet R_W is resulted to be 10.5 nm with polydispersity $R_W/R_N = 1.5$ in Schulz-Zimm distribution function.

The structure factor $S(q,c)$ were obtained as function of q and volume fraction. Two consistency checks for the data indicate that for Laponite particles at volume fraction less than 0.16% the expansion forms of $S(q,c)$ (eq. (2.54), (2.55) and eq. (4.2)) are valid for low q values. From the consistency check an effective diameter d_{eff} of interaction was consistently obtained to be 46 ± 2 nm (Fig. 4.11). A similar value was determined from the plot of B_{app} versus q^2 (Fig. 4.9). The deviation from the actual size of platelets ($2R_g \approx 27$ nm) is due to the strong electrostatic repulsion between charged platelets.

In addition, the experimental determined structure factors $S(q,c)$ were compared with the multicomponent interaction site model. They are in agreement when both a screened Coulomb interaction and an attractive interaction are paid attention to the effective potential of interaction. The attractive interaction may be attributed to the van der Waals attraction or the electrostatic attraction of negative charged surfaces and positive charged edges of Laponite platelets.

5 Structural analysis of Poly(carbon suboxide) in binary water/DMF solutions

5.1 Introduction

There are three possible chemical combinations of carbon with oxide – carbon monoxide, carbon dioxide and carbon suboxide. The former two are classic chemicals which have a long history, while the last one has been prepared and investigated since about hundred years. Diels synthesized carbon suboxide for the first time in 1906 [Diels, 1906], by dehydrating malonic acid at the presence of P_2O_5 . The product can be easily purified by vacuum distillation. The totally linear bonding structure of carbon suboxide (Fig. 5.1(1)) was first proposed by Rix based on infrared spectrum [Rix, 1953], and later better described as quasilinear [Thorson, 1960]. Its crystal structure is newly analyzed by Ellern et al. [2001].

The most important property of carbon suboxide is its polymerization ability through thermal, photochemical or ionizing irradiation initiations [Diels, 1906; Kybett, 1965; Birkofer, 1976]. The obtained polymer is a powdery solid with color ranging from yellow to dark red, thus is also called “red coal”. The red color of the planet Mars has been attributed to the presence of this polymer [Plummer, 1969]. Polymer carbon suboxide was found to have peculiar paramagnetic properties, including its high spin density and photosensitivity [Snow, 1978]. The paramagnetism follows the Curie-Weiss law. The spin concentration of polymer increases with reaction temperature, and can reach 2×10^{19} spin/g at a polymerization temperature of 105°C [Snow, 1978].

A poly- α -pyrone as shown in Fig. 5.1(2) was proposed to be the most possible structure for the polymer, with identical elemental composition as the monomer [Ziegler, 1960]. The structure assignment is based on the results of spectroscopic, chemical and X-ray diffraction analysis [Blake, 1964; Schmidt, 1955; Smith, 1963; Ziegler, 1960; Yang, 1981]. The ladder structure permits different end groups, e.g., the hydroxy- α -pyronic group on exposure to water or the ketenyl group ($\text{C}=\text{C}=\text{O}$), whose existence was proven independent on the polymerization conditions [Carrofiglio, 1982]. The polymer is soluble in water, dimethylsulfoxide (DMSO) or dimethylformamide (DMF), if the polymerization temperature is under 100°C . The molecular weight of the polymer increases with the polymerization

temperature, determined to be 311 to 358 g/mol by vapor pressure osmometry in DMF solution at 75°C [Snow, 1978], which yields the degree of polymerization of 5-6, supported by the result of X-ray diffraction experiment [Blake, 1964]. However, all the researchers can not explain the very low degree of polymerization, with respecting to the active chemical structure (Fig. 5.1(2)).

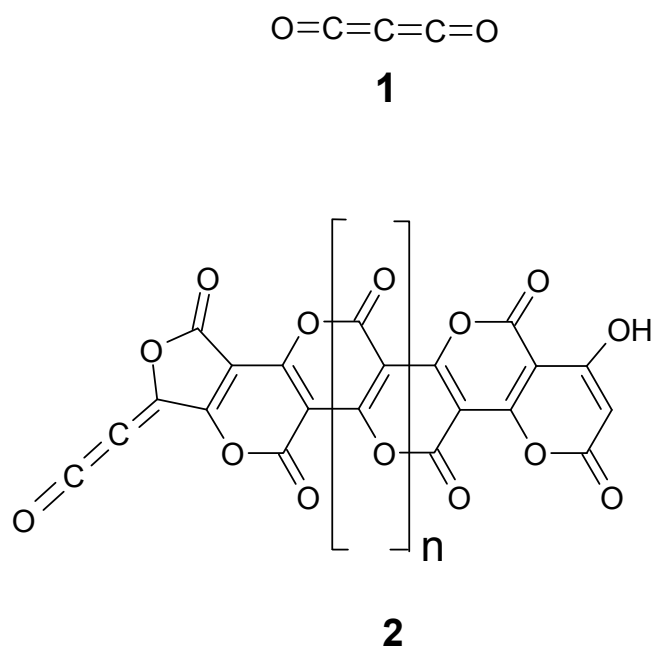


Fig. 5.1 Chemical structure of carbon suboxide (1) and poly(carbon suboxide) (2).

To our knowledge, no report on characterization of poly(carbon suboxide) by small angle X-ray scattering has been found, although it is a suitable method to investigate the shape and structure of poly(carbon suboxide) in solution. The molecular weight and thus the degree of polymerization can be determined through the absolute scattering intensity, with the help of mass density measurement of the polymer in solvent. In this chapter, the structural analysis of poly(carbon suboxide) in binary water/DMF solutions will be executed in detail for the first time.

5.2 Investigated samples

All the investigated samples were prepared by Prof. Beck's group at the university of Bonn. Table 5.1 summarized all the investigated samples with different composition of solvents, measured mass densities, contrast factors calculated according to equation (2.23), and the investigated concentration range.

Table 5.1 Description of investigated samples

| <i>Solvent</i> | | <i>Density of (C₃O₂)_x</i> [g/cm ³] | <i>Contrast factor (SAXS)</i> [mol·l/g ² ·nm ³] | <i>Volume fraction [%]</i> |
|-------------------|-----------------|--|---|----------------------------|
| <i>Water[wt%]</i> | <i>DMF[wt%]</i> | | | |
| 5 | 95 | 1.63 | 0.0204 | 0.22 - 1.10 |
| 10 | 90 | 1.64 | 0.0203 | 0.27 - 0.50 |
| 30 | 70 | 1.47 | 0.0192 | 0.24 - 1.21 |
| 60 | 40 | 1.47 | 0.0178 | 0.25 - 1.18 |
| 100 | 0 | 1.64 | 0.0159 | 0.14 - 0.47 |

5.3 Scattering results and structural analysis for polymer dissolved in water/DMF of 10/90

The scattering result and data treatment will be shown here in detail for polymer dissolved in water/DMF with ratio of 10/90, because it is possible to render the chemical structure of poly(carbon suboxide) with help of structural parameters which yielded by SAXS, and moreover, the chemical structure has no solvent dependence. After that, polymer conformation is investigated, which can be affected by different composition of solvent.

5.3.1 Comparison of different evaluation processes of scattering data

As discussed in chapter 3.1.5, the primary SAXS data were first normalized to the exposure time and the primary beam intensity. Figure 5.2 shows the scattering intensities at

different concentrations as a function of distance h from the center of the primary beam. The direct measured data shows that the scattering intensity increases with concentration.

Due to the low molecular weight of the investigated particles and poor optical contrast between particles and background, the scattering intensity of poly(carbon suboxide) dissolved in water/DMF is weak in comparison to the background, as shown in Fig 5.2.

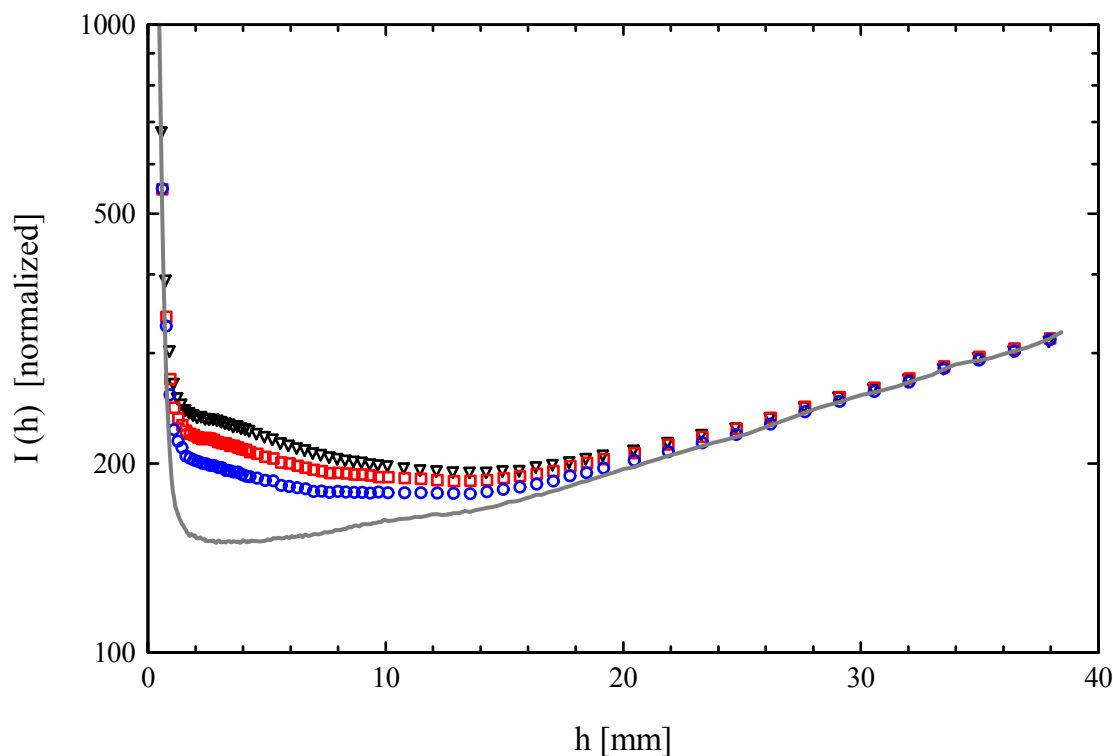


Fig. 5.2 Scattering intensities of poly(carbon suboxide) dispersed in binary water/DMF solvents with ratio of 10/90 as function of the distance h from the center of the primary beam at volume fraction of 0.27% (circles); 0.37% (squares) and 0.5% (triangles) in comparison to the background (solid line).

The first three steps, as in chapter 3.1.5 already described, are the same for all systems, i.e., they do not need any special attention. The scattering intensity of the background was measured separately and then subtracted from the data measured from the dispersions.

For Kratky camera the key step lies in the fourth step-desmearing for the finite dimension of the primary beam. Fig. 5.3 shows the desmeared scattering data without any preliminary or afterwards smoothing. They are strongly scattered due to the limited contrast, as discussed

above. The smoothing procedure is therefore absolutely necessary for data of such weakly scattered samples, which can theoretically be done either before or after desmearing.

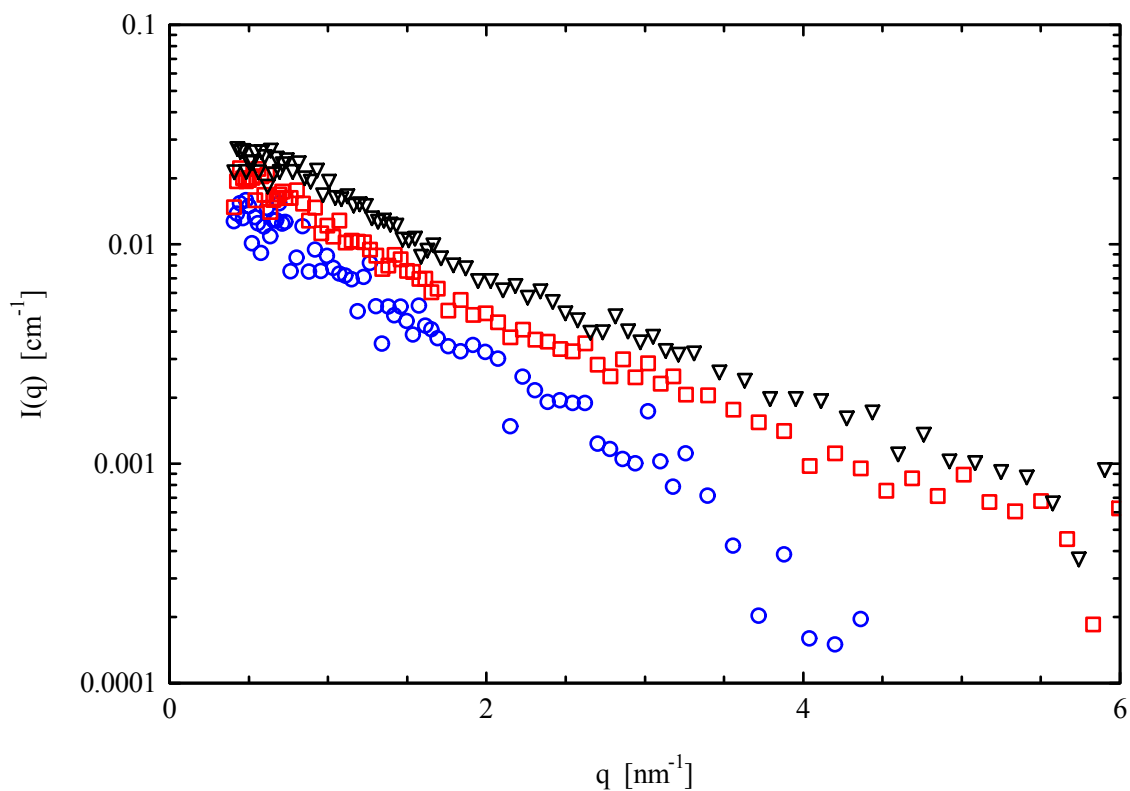


Fig. 5.3 Desmeared scattering intensities due to the finite dimension of the primary beam without any smoothing. Volume fractions: 0.27% (circles), 0.37%(squares) and 0.50% (triangles).

The background subtracted scattering data were then desmeared with preliminary/afterwards slightly smoothing (with ± 2 neighbors averaging) and compared in Fig. 5.4. The two sets of data are almost identical, i.e., the sequence of desmearing and slightly smoothing has no effect on the final data. Both of them can be chosen to evaluate the very scattered data.

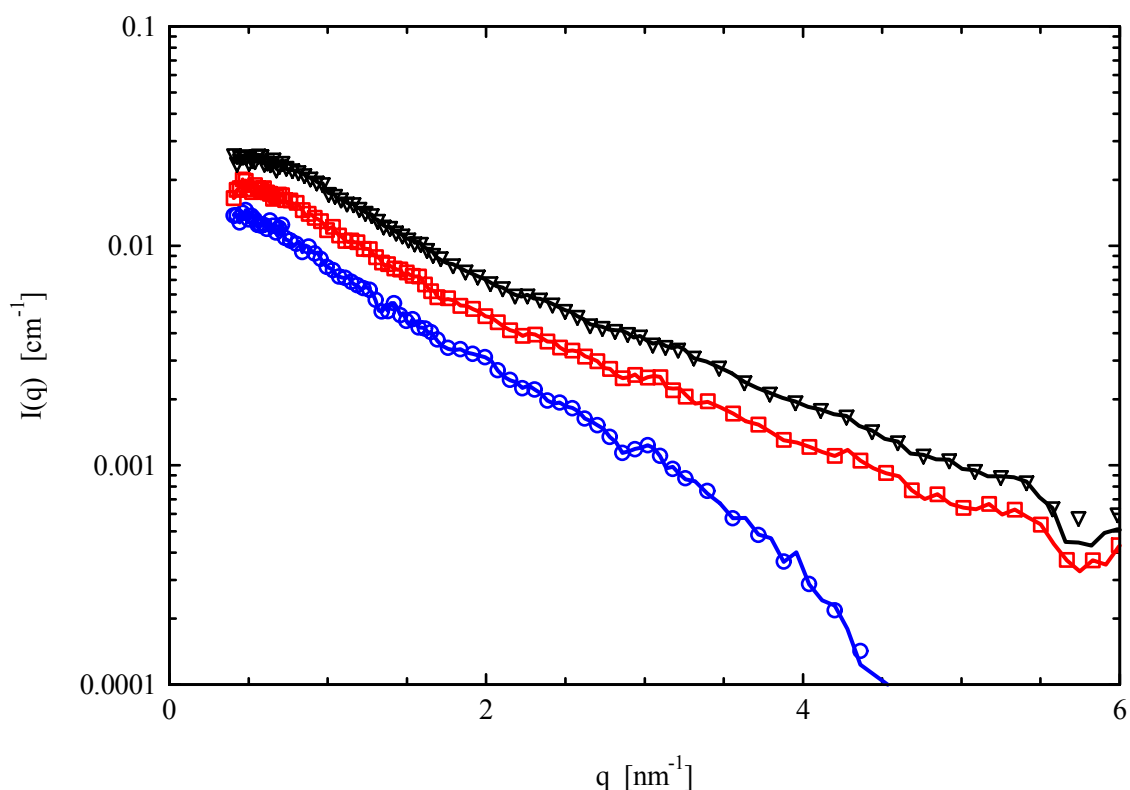


Fig. 5.4 Desmeared scattering intensities of poly(carbon suboxide) at volume fraction of 0.27% (circles), 0.37% (squares) and 0.50% (triangles) with preliminary (lines) / afterwards (points) slightly smoothing (averaging with ± 2 neighbors). For sake of clarity every second point is shown.

However, the sequence of heavily smoothing (with ± 6 neighbors averaging) has evident effect on the final data. As shown in Fig. 5.5, the smoothing after desmearing make the curves more smooth in bending positions than that before desmearing. The bending effect is resulted from the procedure of averaging which is performed on irregularly distributed data and the desmearing can enhance this bending effect. For clarity the inset in Fig. 5.5 shows the comparison of desmeared data in q range of $1.5\text{--}2\text{ nm}^{-1}$ again, where a bending position at $q = 1.72\text{ nm}^{-1}$ is found obviously for data represented by symbols which were obtained from preliminary smoothing. Therefore the smoothing process after the desmearing is recommended in case that a heavily smoothing is performed and moreover, the scattering data are distributed irregularly (density of the data in Fig. 5.5 decreases with increasing of q).

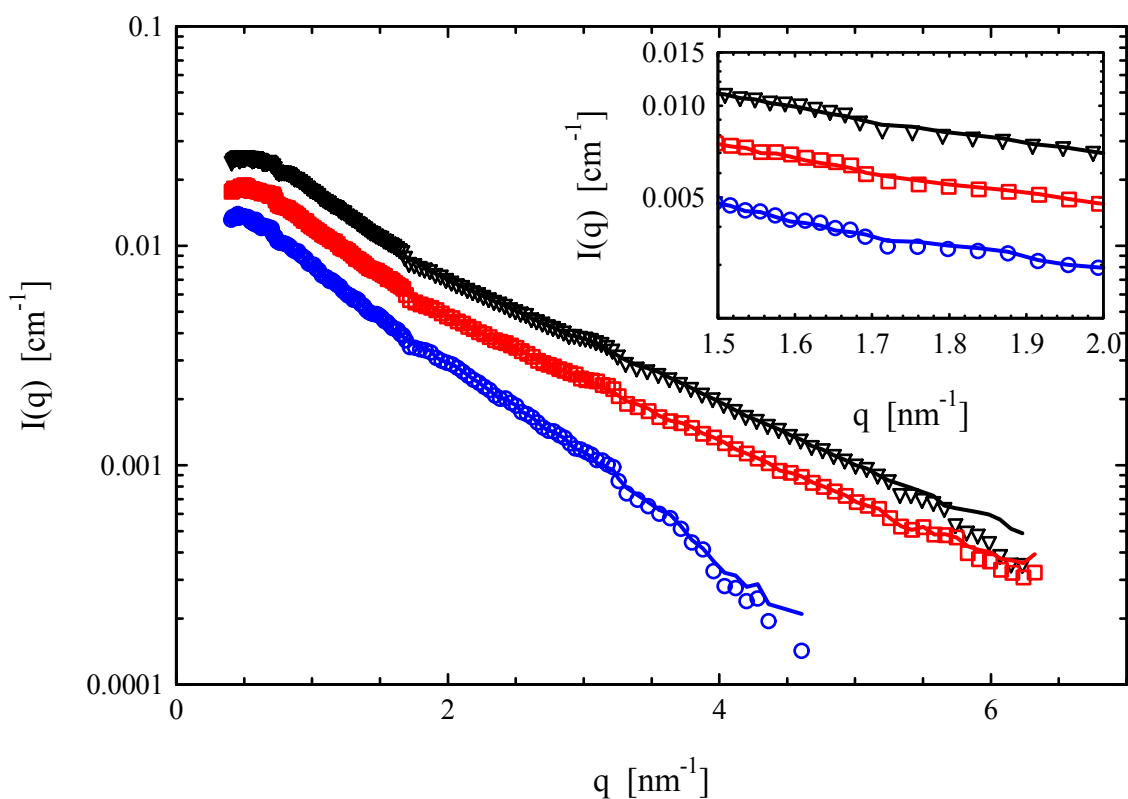


Fig. 5.5 Desmeared scattering intensities of poly(carbon suboxide) at volume fraction of 0.27% (circles), 0.37% (squares) and 0.50% (triangles) with preliminary (lines) / thereafter (points) heavily smoothing (averaging with ± 6 neighbours). For the sake of clarity, the inset shows the comparison again in q region of $1.5\text{--}2\text{ nm}^{-1}$, where one bending position at $q = 1.72\text{ nm}^{-1}$ was found significantly for data represented by symbols which are desmeared data with preliminary smoothing.

The desmeared and afterwards heavily smoothed scattering intensities (lines in Fig. 5.5) are normalized to the concentration and shown in Fig. 5.6 which will be used for further analysis. The normalized scattering intensities should coincide at high q if the structure of the particles is independent of the concentration. This is indeed the case as shown in Figure 5.6 at large q ($> 1.0\text{ nm}^{-1}$), where the merged data can be used further as the form factor of the investigated polymer chains.

At small q one can see a final influence of the structure factor $S(q,c)$ which always exists for practical measurable concentrations. To eliminate the effect of concentration on the scattering intensity, $\phi I(q)$ was extrapolated for each q -value to vanishing concentration (Fig.

5.7). The extrapolated data at vanishing concentration $I(q)_{\phi \rightarrow 0}$ (solid line in Fig. 5.6) was then treated as the form factor $P(q)$, provided it is normalized in such a way that $I(0)_{\phi \rightarrow 0} = 1$. It will be used not only to determine the molecular weight and the size of the scattering particles, but also to characterize the chemical and conformational structure of polymer in solution.

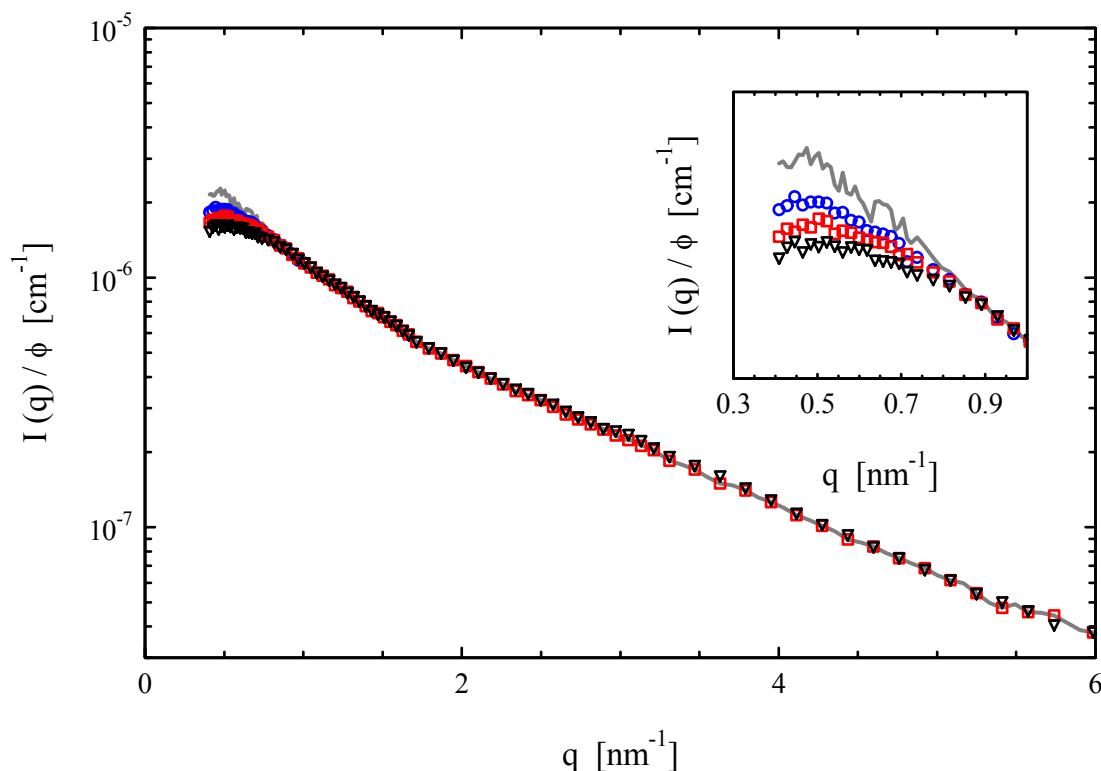


Fig. 5.6 Corrected scattering intensities normalized to the respective concentrations. The solid line represents the extrapolated scattering intensity to vanishing concentration, e.g. the form factor $P(q)$. The inset shows the same graph at low q range again for sake of clarity.

According to Guinier-law (eq. 2.14), the extrapolated data were performed as shown in Fig. 5.8 to determine the molecular weight M_W and radius of gyration R_g . From the intercept and slope of the linear regression there M_W and R_g were obtained to be 2750 ± 600 g/mol and 1.7 nm, respectively. This molecular weight is much larger than literature values, e.g. 420-560 g/mol from Carofiglio et al. [Carofiglio, 1986], 5-10 C_3O_2 units from Blake et al. [Blake, 1964], and 311-358 g/mol from Snow et al. [Snow, 1978], although the accuracy of measurements is limited due to the poor scattering contrast. The determined radius of gyration of 1.7 nm implies also a relative large investigated particle size.

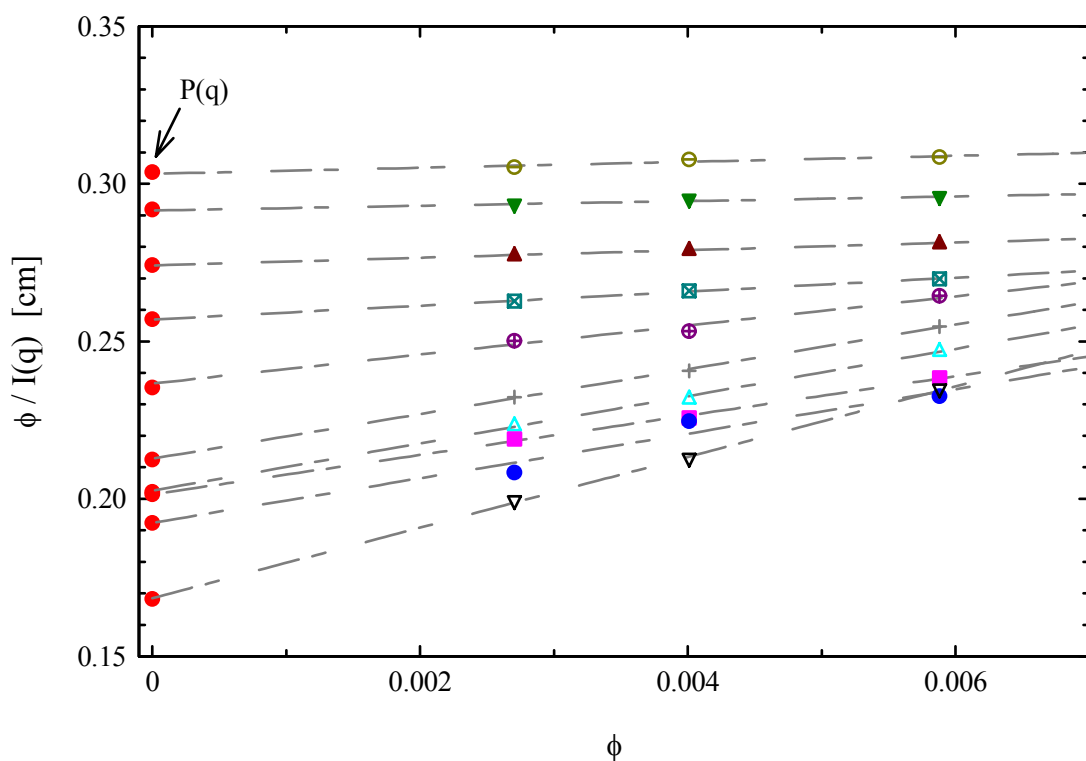


Fig. 5.7 Extrapolation of concentration at q range of $0.4 - 1.0 \text{ nm}^{-1}$.

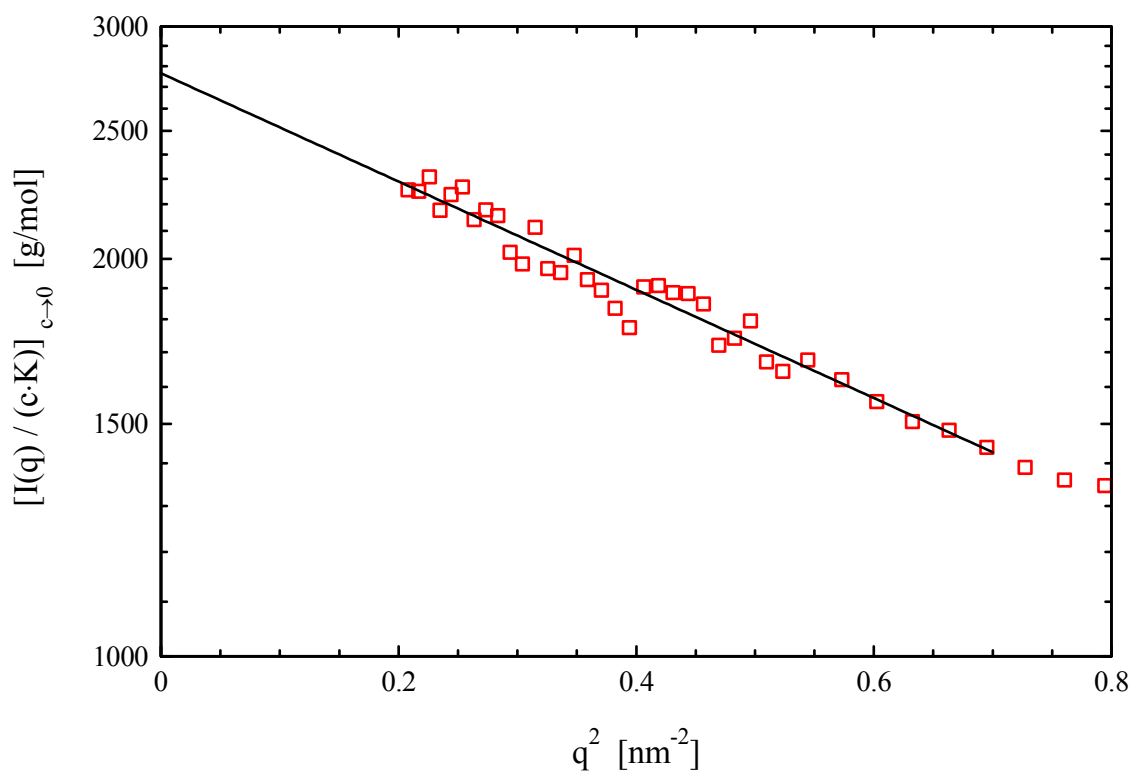


Fig. 5.8 Guinier-plot of extrapolated scattering intensity of poly(carbon suboxide) dispersed in water/DMF with percentage of 10/90.

5.3.2 Structural analysis

In order to find information about the shape and structure of the polymer particles in solutions, the analysis should be extended to scattering function at higher q . If the polymer has ladder chemical structure as expected from literature, the extrapolated scattering function at high q range should show a scaling law of $I(q)_{c \rightarrow 0} \sim q^{-1}$ (eq. 2.22), i.e., the polymer particles behave like rods or flexible chains. In comparison to cylinder, the flexible chain has one more parameter in fit program-persistence length b , which is a parameter to describe the flexibility of the chain. If the contour length L_C of a chain is much larger than its persistence length, the chain should be treated like a flexible coil. Otherwise, if the two lengths are comparable in value order, the chain behaves like a rod or the so-called semiflexible chain. Fig. 5.9 represents therefore the scattering function by plotting $I(q) \cdot q$ versus q^2 , where a linear relationship was found indeed for $q > 1.7 \text{ nm}^{-1}$. Thus the investigated particles in solutions can be concluded to be of the shape of polymer chains, their flexibility can be found out through fitting with a flexible chain model. Kholodenko's approximation (see section 2.2.3) was used here to fit the experimental data due to its universality, i.e., there exists no limit for the flexibility of chains by applying this model.

With knowledge about the particle shape-polymer chains, we can also use the plot of $I(q) \cdot q$ at vanishing concentration versus q^2 to determine two local structural parameters-molecular weight per nanometer M_L and radius of gyration in cross-section R_C , according to eq. (2.22). As shown in Fig. 5.9 from the linear regression, M_L and R_C were obtained to be 360 g/(mol.nm) and 0.3 nm, respectively. In comparison of the obtained M_L with molecular weight M_W , which was obtained above by Guinier-plot (Fig. 5.8), the contour length L_C of the polymer chains was resulted to be $7.7 \pm 1.7 \text{ nm}$. Furthermore, the obtained M_L and R_C permit us to confirm the chemical structure of poly(carbon suboxide) to repeated pyronic ring, as shown in Fig. 5.1 (2). According to this chemical structure every 5 repeat units are of the length of polymer chains about 1 nm, i.e. M_L is theoretically about 5 times molecular weight of monomers which is calculated to be 340 g/(mol.nm). This value is in good agreement with the above obtained one by SAXS measurements ($M_L = 350 \text{ g/(mol.nm)}$). Another characteristic parameter is the radius of gyration R_C perpendicular to the chain axis, which is calculated according to the chemical structure in Fig. 5.1 (2) to be 0.30 nm and is also in good agreement with SAXS result of $R_C = 0.3 \text{ nm}$.

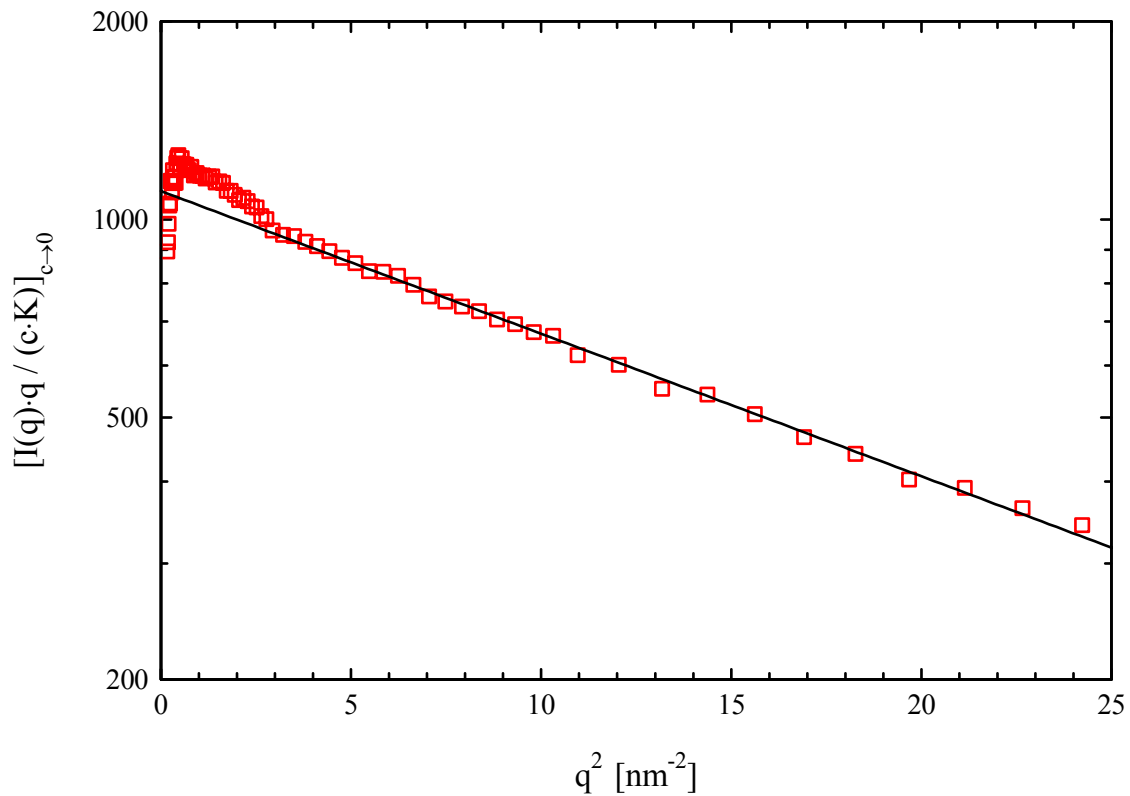


Fig. 5.9 Plot of $I(q)q/(Kc)$ as function of q^2 at vanishing concentration to obtain $M_L = 350 \text{ g}/(\text{mol}\cdot\text{nm})$ and $R_C = 0.3 \text{ nm}$ according to eq. (2.21). The intercept of the linear regression gives directly the value of πM_L .

The flexibility of the investigated polymer chains can be determined by the model fitting. One of another important parameters for characterization of polymer chains is the polydispersity of the length which should be taken into account in model fitting. Without any information about it, this polydispersity of length of the polymer chains was supposed to be 1.1 or 1.4 in Schulz-Zimm distribution (eq. (2.58)). The respective fitting results are shown in Fig. 5.10 by a so-called Holzer representation, with exclusion of the finite cross-section effect. Both fitting curves are in good agreement with experimental data, $b = 1.5 \text{ nm}$ for polydispersity of 1.1 and $b = 1.3 \text{ nm}$ for polydispersity of 1.4 were set in the model fittings, respectively.

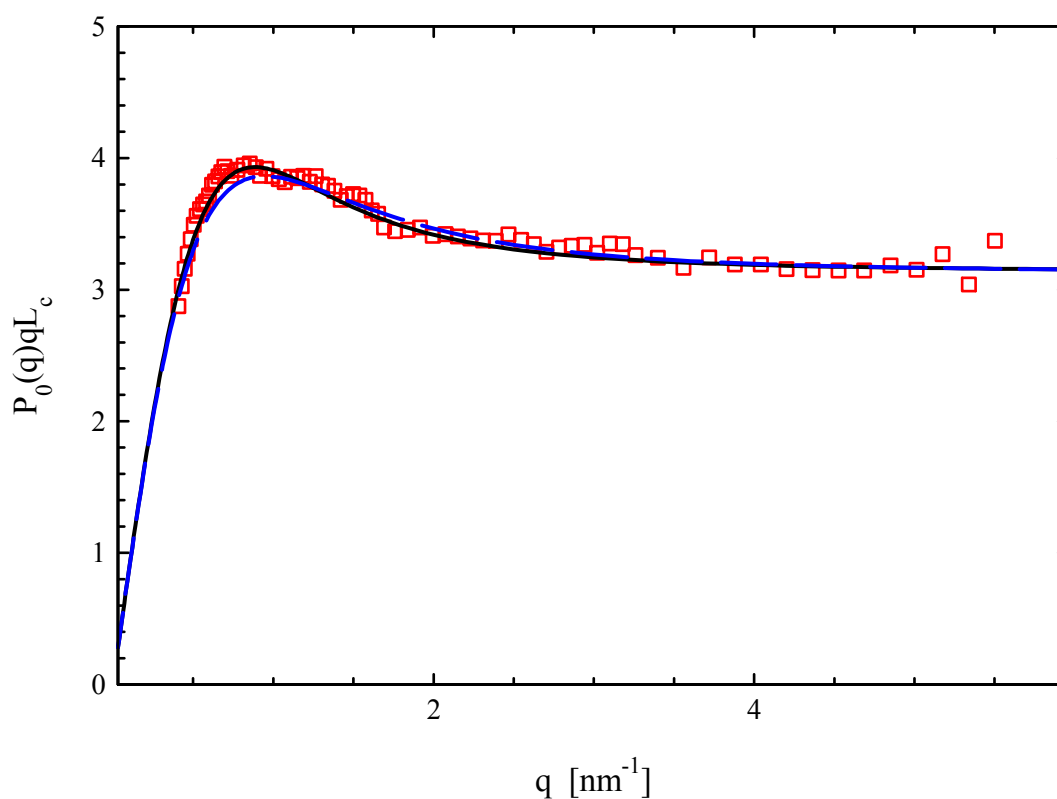


Fig. 5.10 Holzer representation of the corrected form factor $P_0(q)$ (signals), i.e., the effect of cross-section was excluded. The solid line is the fitting curve with $L_W/L_N = 1.1$, $b = 1.5$ nm, whereas the dashed line is the fitting curve with $L_W/L_N = 1.4$ and $b = 1.3$ nm.

5.4 Effect of the binary water/DMF solvents on the structure of poly(carbon suboxide)

The scattering intensities of poly(carbon suboxide) dissolved in 5 different percentages of water/DMF solvents as described in table 5.1 were measured, in order to investigate the effect of solvents on the conformation of the polymer chains. With the same evaluation procedure for the SAXS data of polymer chains dissolved in water/DMF of 10/90 as shown from Fig. 5.2 to Fig. 5.7 above, the extrapolated scattering intensities (form factors) for the rest four systems are evaluated and shown in Fig. 5.11 together, in comparison with the above already analyzed form factor of polymer chains dissolved in water/DMF of 10/90.

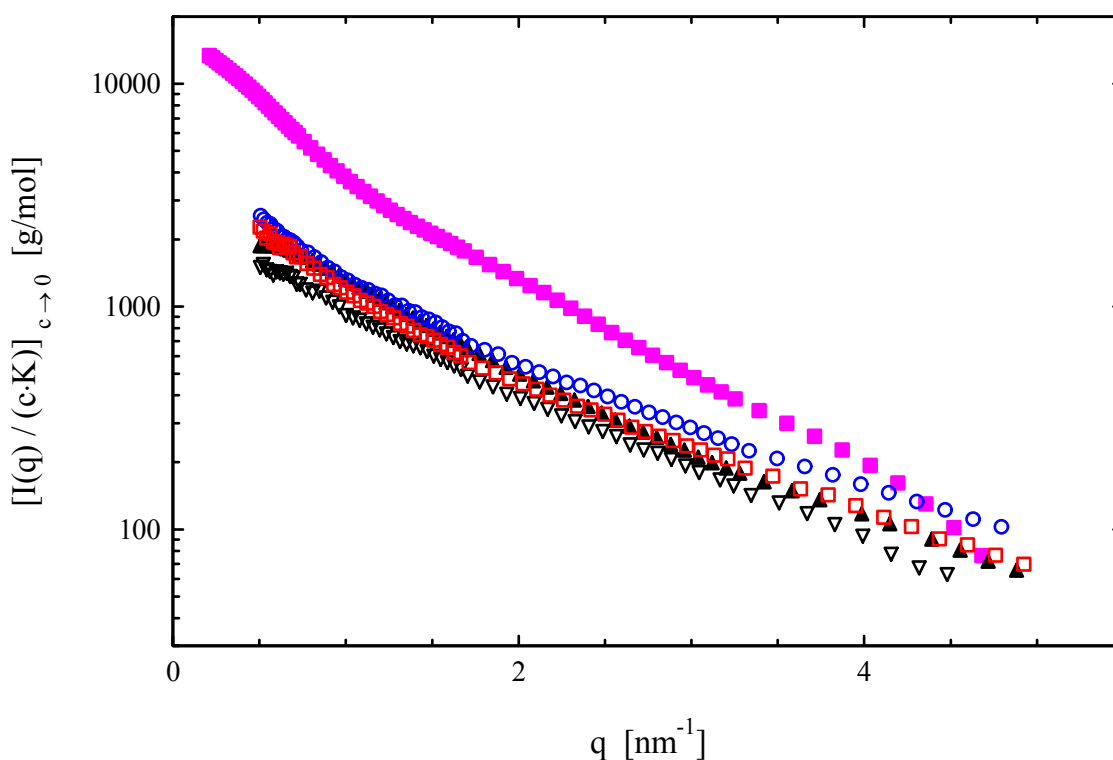


Fig. 5.11 Extrapolated scattering intensities (form factor) of the five investigated systems with different percentage of water: (○) 5%; (□) 10%; (▽) 30%; (▲) 60%; (■) 100%.

As shown in Fig. 5.11, the absolute scattering intensity of dissolved polymer in pure water is much higher than that of binary solvents systems, which means that poly(carbon suboxide) particles in pure water show much larger size and molecular weight than those dissolved in binary solvents. According to Guinier-law the molecular weight M_W and radius of gyration R_g were obtained for all the five systems and plotted in Fig. 5.12. Within error limit, the difference of M_W and R_g between the first four systems can be neglected. With a correction factor of $\pm 20\%$ (under experimental error range) the scattering functions for the first four systems were corrected and shown in Fig. 5.13. It is obvious that the first four systems have the same scattering form factors, i.e., the structure and conformation of polymer chains do not depend on the composition of the solvent, if the weight fraction of water is not more than 60%. All of them can be fitted by the same set of parameters in Kholodenko's approximation.

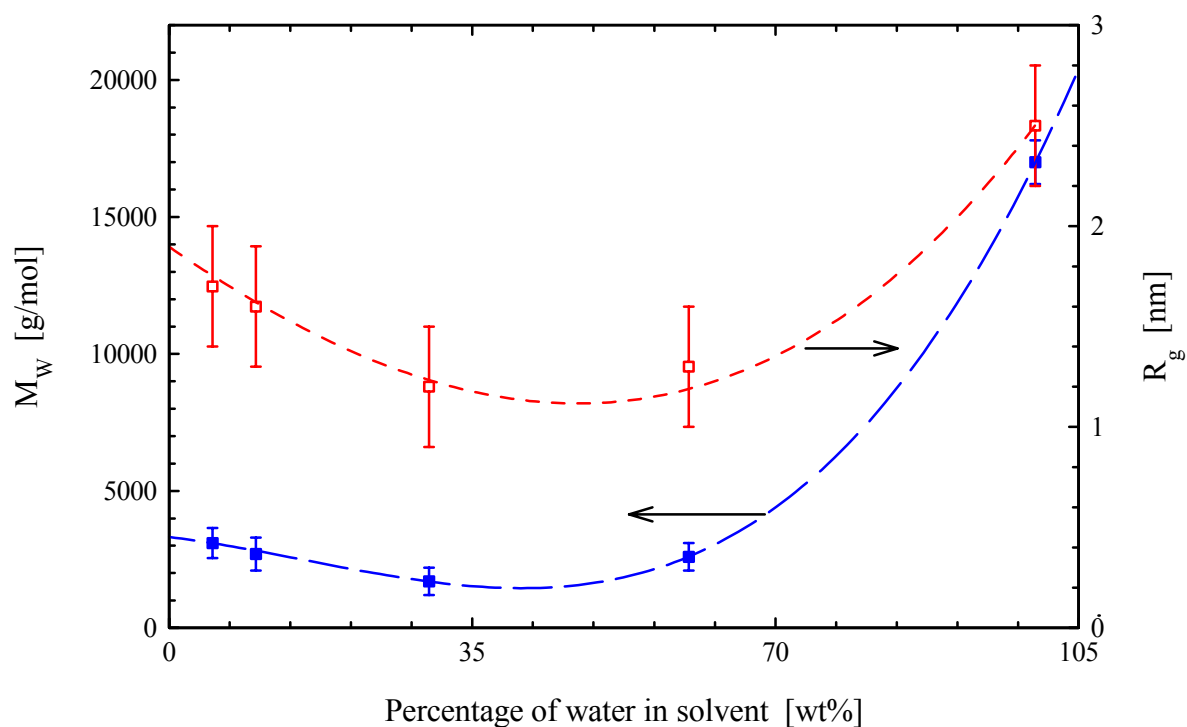


Fig. 5.12 Molecular weight M_w (filled squares) and radius of gyration R_g (hollow squares) of polymer chains in different percentage of water, obtained according to Guinier-law (eq. (2. 13)).

However, for polymer chains dissolved in pure water, the extrapolated scattering intensity is much higher than the other four systems which may be attributed to the appearance of aggregation. Although the scattering function in this case can also be fitted by Kholodenko's approximation, the resulted ratio of M_L/R_C differs strongly from that of the other four systems, i.e., M_L does not increase monotonically with R_C in aggregation state. In other words, the aggregation particles are not formed by the simple addition of polymer chains, which can not be explained until now. All the used parameters in model fittings for the investigated five systems are gathered in table 5.2, where n denotes the polymerization's degree which is the molecular weight of polymer chains M_w divided by the molecular weight of carbon suboxide.

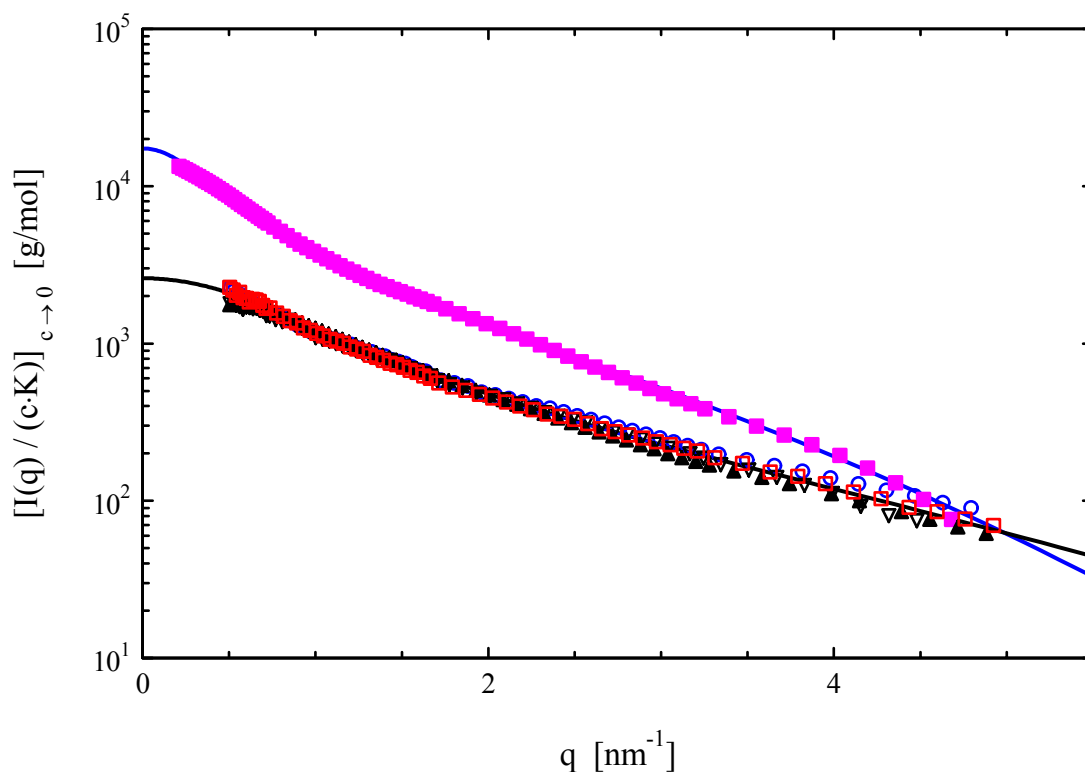


Fig. 5.13 Extrapolated scattering intensities (form factor) of the five investigated systems with different percentage of water: (○) 5%; (□) 10%; (▽) 30%; (▲) 60%; (■) 100% after correction of scattering intensity with factor of 0.88 for 5% water system and 1.2 for 30% water system, due to the limited accuracy of the data. The first four systems can be described by the same set of parameters in Kholodenko's approximation (solid line).

Table 5.2 Fit parameters for the SAXS data on poly(carbon suboxide) in binary water/DMF solvents using flexible chain approximation of Kholodenko.

| Water in solvent [wt%] | L_C [nm] | L_P [nm] | L_W/L_N | R_C [nm] | M_W [g/mol] | M_L [g/(nm·mol)] | R_g [nm] | n |
|---------------------------|---------------|---------------|-----------|---------------|------------------|-----------------------|---------------|-----|
| 5 | 8 | 1.5 | 1.1 | 0.30 | 3090 | 380 | 1.7 | 45 |
| 10 | 8 | 1.5 | 1.1 | 0.30 | 2760 | 350 | 1.7 | 40 |
| 30 | 8 | 1.5 | 1.1 | 0.30 | 2120 | 270 | 1.4 | 31 |
| 60 | 8 | 1.5 | 1.1 | 0.30 | 2620 | 330 | 1.3 | 39 |
| 100 | 12 | 3 | 1.4 | 0.45 | 16500 | 1470 | 2.5 | 240 |

The aggregation behavior of polymer chains in absence of DMF demonstrates that DMF plays an important roll in dissolving polymer carbon suboxide in water. Without DMF in solvent, hydrogen-bond bridge between particles, as shown in Fig. 5.14, may becomes the main force for the formation of aggregates. The presence of end hydroxy bond was testified by IR in present of water [Smith, 1963].

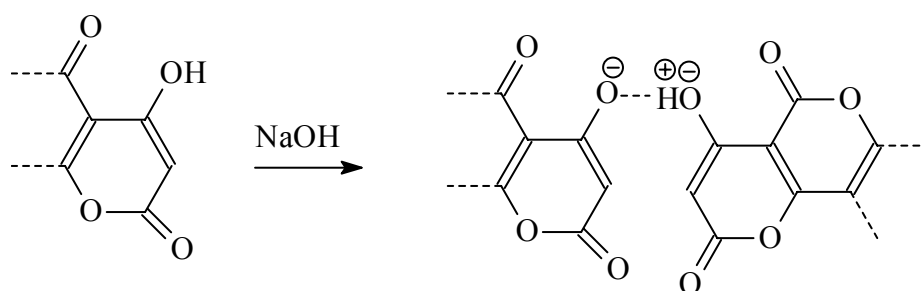


Fig. 5.14 Possible formation of the hydrogen-bond bridge between particles under effect of NaOH.

5.5 Conclusion

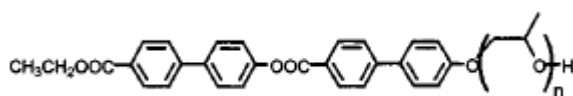
The size, shape and chemical structure of poly(carbon suboxide) particles in binary water/DMF solutions were investigated by means of SAXS using commercial Kratky camera. Without any assumption about its shape and structure the molecular weight and gyration radius of particles were determined to be 2760 g/mol and 1.7 nm, respectively. The polymerization's degree (carbon suboxide as repeat unit) is therefore determined about 40, which is much larger than 5-15 as reported in most literatures. Moreover, the scattering function of the polymer dispersed in binary solutions was predicted by a semi-flexible chain model with contour length of 8 nm and persistence length of 1.5 nm. The scattering function was also represented by plotting $\ln[I(q)q]$ vs. q^2 , where from the linear regression for the intermediate q range, the local structure of polymer chains can be analyzed. The obtained M_L (molecular weight per unit length) and R_C (gyration radius in cross-section) confirmed the chemical structure of repeat pyronic ring, which is supposed in most cases by literatures.

The effect of the binary solvent water/DMF on the formation of the polymer chains was studied as well. With the weight fraction of water in solvent not more than 60%, the polymer chains keep the same conformation. However, with increasing the fraction of water in solvent till 100%, i.e., in absent of DMF, the polymer chains aggregate in an unexpected way. The molecular weight of aggregates is determined to be about 6 times of molecular weight of single polymer chains, i.e., the average association number of aggregates is 6.

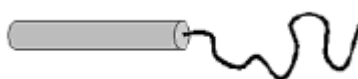
6 Structural analysis of nano-scaled aggregates derived from self-assembly of coil-ring-coil block copolymers

6.1 Introduction

One of the fascinating subjects in areas such as materials science and nanochemistry is concerned with the creation of supramolecular architectures with well-defined shapes and functions. Self-assembly of molecules through non-covalent forces including hydrophobic and hydrophilic effects, electrostatic interactions, hydrogen bonding, and microphase segregation has the great potential for creating such supramolecular structures [e.g. Lee, 2001; Lehn, 1995; Muthukumar, 1997; Whitesides, 1991; Förster, 1998; Israelachvili, 1985]. Among them, rod-coil block copolymers can produce a novel class of self-assembling materials due to the microphase separation of the rigid rod and the rather flexible coil blocks [e.g. Zubarev, 1999; Chen, 1966; Jenekhe, 1999; Klok, 2000, Engelkamp, 1999; Lee, 2001; Raez, 2002]. The nature of blocks, the molecular weight, the volume fraction of the rigid and the flexible blocks and the property of solvent can affect the formation of such supramolecular structure [e.g., Lee, 2001; Klok, 2001; Mao, 1997]. As an example, Fig. 6.2 represents a dramatic structural change in the melt state of a rod-coil block copolymers (Fig. 6.1) [Lee et al., 2001]. With increase of the coil length, the supramolecular structure changes from smectic A to bicontinuous cubic and further to the hexagonal columnar phases.



(a)



(b)

Fig. 6.1 A rod-coil diblock molecules consisting of ester linked two biphenyl groups as the rod part and PPO coil part: (a) chemical structure, (b) schematic description.

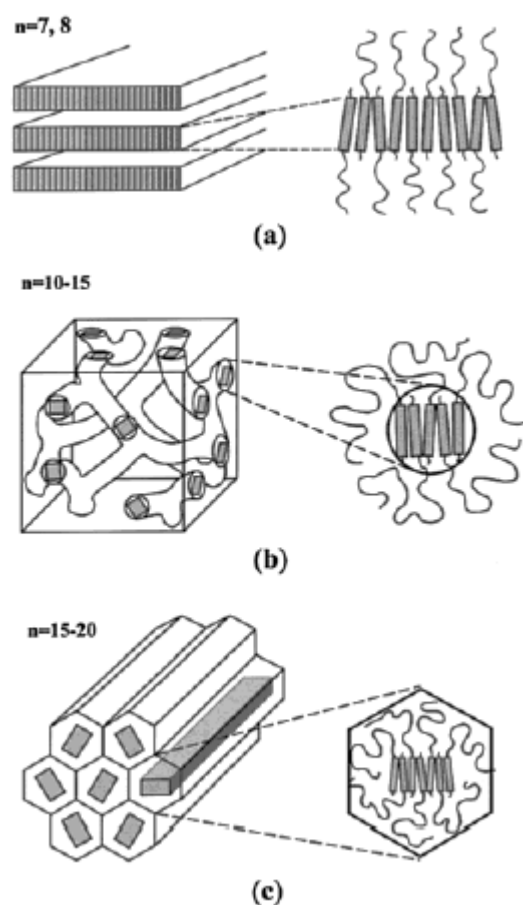


Fig. 6.2 Schematic representation of supramolecular structures of rod-coil molecules described in Fig. 6.1: (a) Smectic A, (b) bicontinuous cubic, and (c) hexagonal columnar phases [Lee et al., 2001].

Recently, Höger and coworkers [Rosselli et al, 2001; 2003; Höger et al., 2002; 2003; 2004] synthesized a subclass of rod-coil block copolymers in which the rigid part is a nano-sized shape-persistent macrocycle to which two polystyrene (PS) blocks are covalently attached (Fig. 6.3). The solubility of the rigid ring is largely enhanced due to the attachment of the flexible side groups.

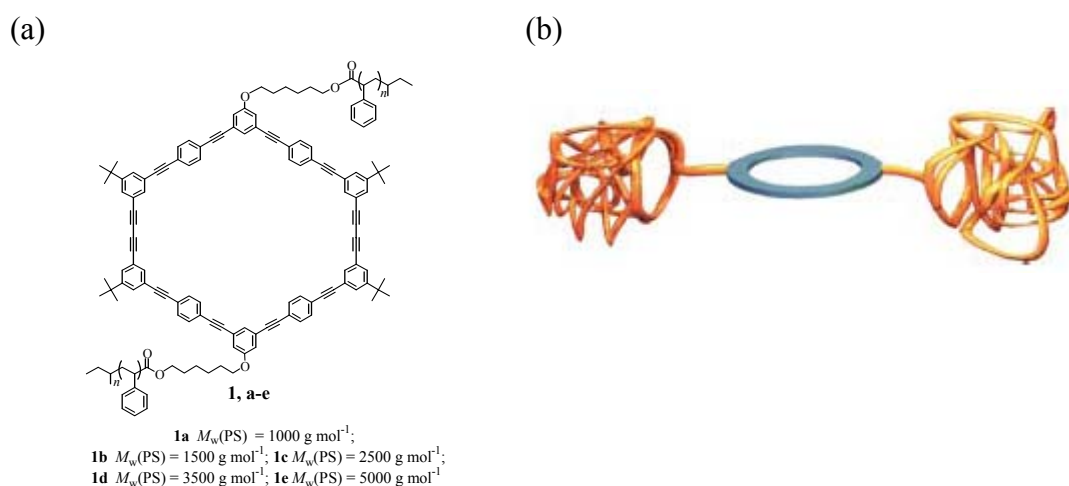


Fig. 6.3 Polystyrene(PS)-substituted macrocycles: (a) chemical structure with **1a-e** indicating the part of PS with different molecular weight, (b) schematic description.

Block copolymers of **1a-e** in Fig. 6.3 are well soluble in THF, toluene, or halogenated solvents at room temperature, however, the solubility of the block copolymers in aliphatic solvents strongly depends on the size of the coil part [Höger, 2004]. Among them, **1a** forms only a suspension even in warm cyclohexane, whereas **1b-e** are well soluble in cyclohexane at elevated temperatures. Upon cooling, **1b** forms a gel at concentration above 5 g/l, while **1c** and **1d** form viscous solutions within one hour and in several days, respectively. Their solutions are strongly birefringent except of solution of **1e**, which exhibits neither viscous nor birefringence. Höger et al. have attributed this phenomenon to the different solubility of the rigid and the flexible parts of the macrocycles, since cyclohexane is a theta solvent for PS, but, in contrast to THF or toluene, a non-solvent for the rigid core [Höger, 2004]. The special interest for further studying focuses therefore on solutions of **1c** in cyclohexane.

Solutions of **1c** have been studied by dynamic light scattering (DLS), electron microscopy and SAXS methods [Höger, 2002; 2004; Rosselli, 2001]. DLS was performed on solutions of **1c** in toluene and cyclohexane (Fig. 6.4), revealing that in toluene there is only one species with a hydrodynamic radius of about 2 nm which arises from single block copolymers, however, in cyclohexane two species are found with hydrodynamic radius of about 2 nm and 60 nm, respectively. With help of the angle-dependence studying of the scattering intensity the additional signal presented at about 60 nm with a broad distribution has been attributed to the presence of rod-like particles with length between 250 nm and

1300 nm, i.e., some supramolecular structure appears due to the rigid core and its solvophobic property [Höger et al., 2002]. The transmission electron micrograph (TEM) and atomic force microscopy (AFM) of a solution of **1c** (Fig. 6.5) show long rigid rods having a diameter of about 10 nm, among which some thicker rods are attributed to bundles of two or three cylindrical aggregates [Rosselli et al., 2001; Höger et al., 2002].

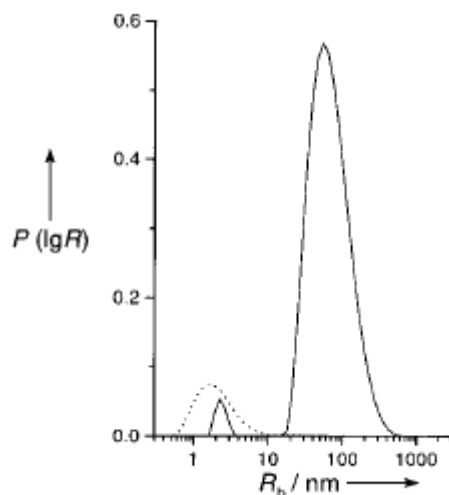


Fig. 6.4 DLS spectrum with CONTIN-fit: rate distribution of **1c** in toluene (....) and in cyclohexane (—) at a concentration of 0.11 wt% [Rosselli et al., 2001; Höger et al., 2002; 2004].

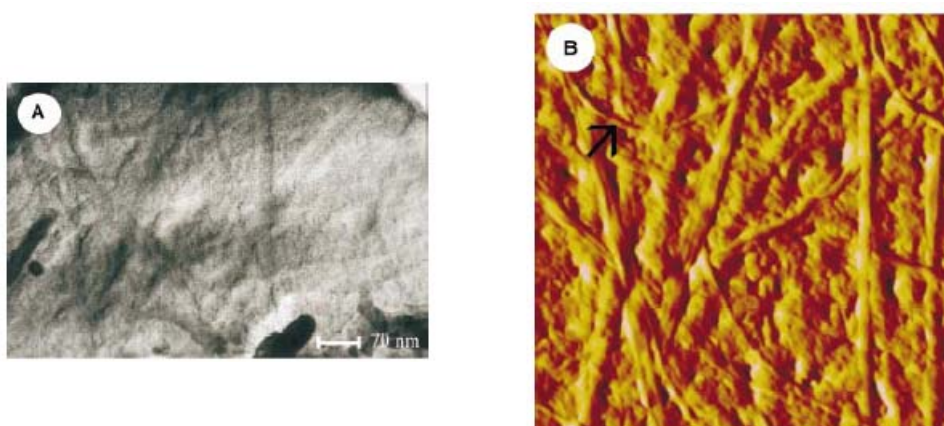


Fig. 6.5 A) TEM: C/Pt shadowed film obtained by freeze drying a 0.15 wt% cyclohexane solution of **1c**. B) AFM (amplitude picture: $1.5 \times 1.5 \mu\text{m}^2$): Film obtained by dipping mica into a 0.15 wt% cyclohexane solution of **1c** [Rosselli et al., 2001; Höger et al., 2002].

A preliminary analysis by small angle X-ray scattering (SAXS) has been performed to determine the diameter of these cylindrical objects while their lengths are out of the measurable range of SAXS. By comparison of the experimental form factor (taken from a 2.0 wt% cyclohexane solution of **1c**) with massive and hollow cylinder models (Fig. 6.6) the coil-ring-coil block copolymers are assumed to form hollow cylinder-shaped objects [Fig. 6.7] with an outer diameter $d_{out} = 10$ nm and inner diameter $d_{in} = 1.8$ nm, as well as the polydispersity is of 3.8 nm for outer and 0.5 nm for inner.

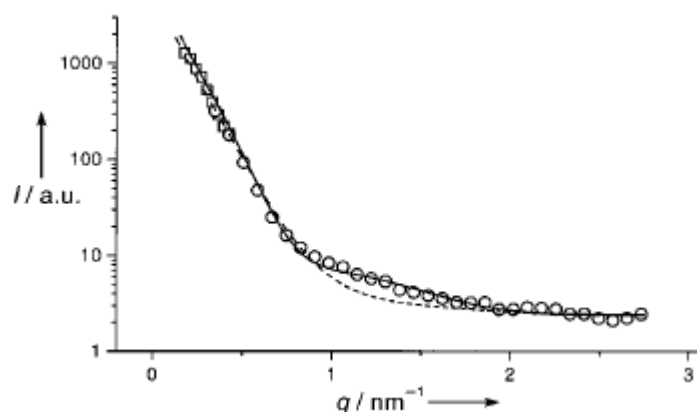


Fig. 6.6 SAXS data (signals) of a 2.0 wt% cyclohexane solution of **1c**. The lines represent the form factor for a massive cylinder (----) with an external diameter $d_{out} = 10$ nm, polydispersity $\sigma = 3.8$ nm, and for a hollow cylinder (—) with an external diameter $d_{out} = 10$ nm, polydispersity $\sigma = 3.8$ nm and an internal diameter $d_{in} = 1.8$ nm, polydispersity $\sigma = 0.5$ nm [Rosselli et al., 2001; Höger et al., 2002].



Fig. 6.7 Schematic description of aggregation of the coil-ring-coil block copolymers into hollow cylindrical brushes [Rosselli et al., 2001; Höger et al., 2002].

The motivation of the present work is to investigate the internal structure of single aggregates of **1c** by SAXS in detail on the base of the previous work of Höger et al.. The form factor of single aggregates will be determined by the scattering intensities of samples with a concentration serial in order to exclude interparticle interactions, instead of only by that of one solution in literature [Höger, 2002; 2004; Rosselli, 2001]. The determination of the absolute scattering intensity (which has not been done in literature) allows the determination of molecular weight per unit length M_L ($= M_w/L$, L denotes the total length of cylindrical objects), from which the important local structural information of the aggregates can be obtained.

6.2 Experimental

1c cyclohexane solutions were measured as received from prof. Höger, with concentrations of 3.6 g/l, 5.6 g/l, 11.1 g/l and 15.6 g/l, respectively. SAXS measurements were performed by using a modified Kratky camera in our laboratory. The instrumental setup and data treatment of this camera have been introduced in chapter 3. The scattering intensities of empty capillary, capillary filled with cyclohexane and **1c** solutions were measured separately.

The mass density of **1c** in cyclohexane was determined by a density meter (DMA 60, Paar) to be 1.07 g/cm³, which yields a value of 0.00845 mol/g² for the contrast factor K , according to eq. (2.23). The electron density of the coil-ring-coil block copolymer is deduced to be 344 e.u./nm³.

6.3 SAXS results and discussion

Scattering intensities of **1c** solutions with 4 different concentrations ranging from 3.6 g/l to 15.2 g/l and background (solvent + capillary) as function of distance h from center of primary beam are shown in Fig. 6.8. As expected, the scattering intensity enhances with concentration. One observation is that the scattering intensity of **1c** solutions in Fig. 6.8 is high at low h which implies that the scattered objects are huge; on the other hand, the scattering intensity decreases rapidly with increase of h , upon $h = 20$ mm (corresponding to scattering vector $q = 2$ nm⁻¹) the scattering intensities of solutions merge into background.

Another phenomenon is that at low h region there exists a shoulder of the scattering function for solution of $c = 15.2$ g/l (the highest concentration between the investigated solutions), which differs from the others significantly.

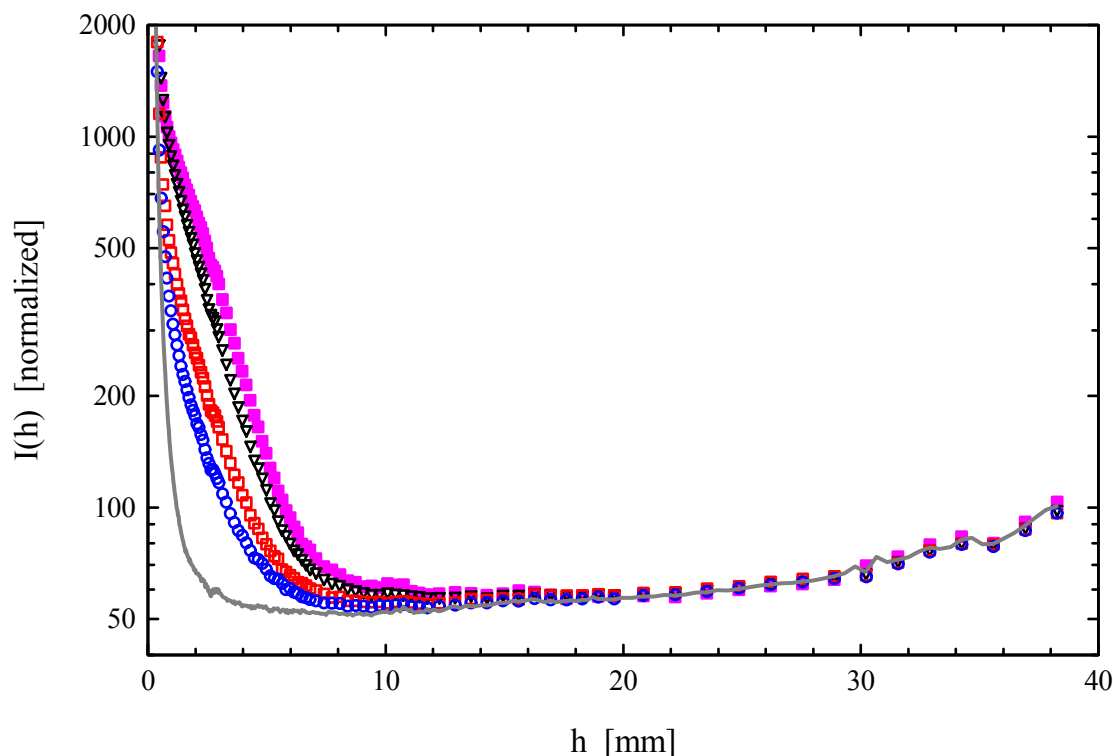


Fig. 6.8 Normalized scattering intensity as function of distance h from center of primary beam at concentration of 3.6 g/l (circles), 5.6 g/l (squares), 11.1 g/l (triangles) and 15.2 g/l (filled squares), in comparison to the background (solid curve).

As next step the scattering intensities of solutions have been subtracted from the background and corrected for the finite dimensions of the primary beam. Normalized to concentration, the absolute scattering intensity is plotted as function of the scattering vector q upon $q = 2 \text{ nm}^{-1}$ in Fig. 6.9. Except for the highest concentration sample, the scattering intensities of the other three solutions are identical for investigated q range (the slight discrepancy at $q > 0.75 \text{ nm}^{-1}$ is due to the limited difference of scattering intensity between solution and background in this q range). The scattering intensity of solution with the highest concentration ($c = 15.2$ g/l) is clearly lower than those of the other three in low q range ($0.05 - 0.25 \text{ nm}^{-1}$), which can be attributed to the concentration effect. It seems that interparticle interactions domain the scattering intensity in this q range at concentration $c > 11$ g/l.

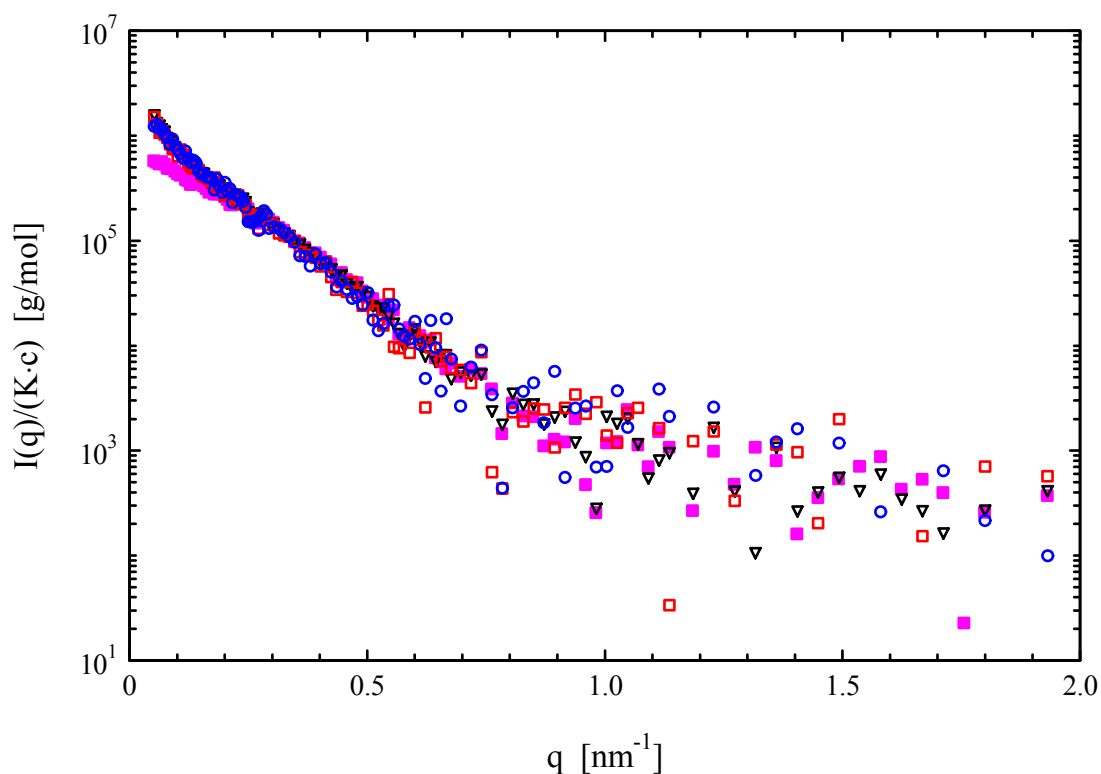


Fig. 6.9 Effect of concentration: Desmeared and for the concentration normalized scattering intensity $I(q)/(c \cdot K)$ as function of scattering vector q at concentration of 3.6 g/l (circles), 5.6 g/l (squares), 11.1 g/l (triangles) and 15.2 g/l (filled squares).

Since the scattering functions of solutions for the first three concentrations merge together, i.e., the concentration effect is negligible in this dilute range ($c \leq 11$ g/l), it is safe to treat these scattering functions as form factor of the supramolecular aggregates. For statistic reason the scattering data from solution with $c = 11.1$ g/l (the highest concentration among the first three solutions), is used as form factor for further analysis.

Although the whole size of the investigated objects can not be determined due to exceeding of experimental range (length $L > 200$ nm), its local size, such as molecular weight per unit length $M_L (= M_W/L)$ and radius of gyration of cross-section R_C can be determined directly by plotting $I(q) \cdot q$ against q^2 , based on the assumption that the investigated aggregates have cylindrical shape [Rosselli et al., 2001; Höger et al., 2004]. Fig. 6.10 represents the form factor in this way and a linear relationship was found indeed for data at low q range. M_L and R_C were thus determined to be 25730 ± 5100 g/(mol.nm) and 3.6 nm

from intercept and slope of the linear regression, respectively, based on equation (2.22) in chapter 2.

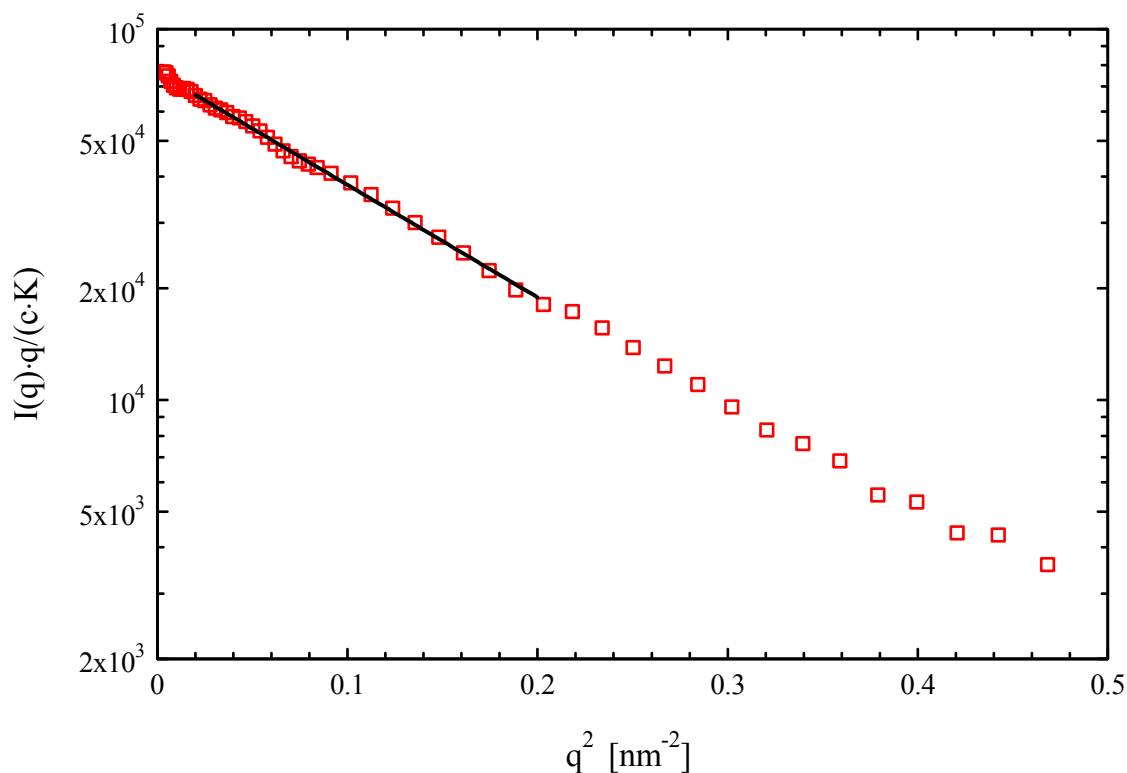


Fig. 6.10 Representation of the scattering intensity by plotting $I(q) \cdot q / (c \cdot K)$ vs. q^2 (data from the solution with $c = 11.1$ g/l). A linearly relationship was found for data at low q values, from which M_L (molecular weight per nanometer) was determined to be about 25730 ± 5100 g/(mol.nm).

Since the weight average molecular weight M_0 of one single coil-ring-coil block copolymer **1c** is known as 6500 g/mol, the average association number of this block copolymers in aggregates can be then concluded to be about 4/nm ($= M_L/M_0$). This is an unexpected large value in comparison to the thickness of 0.6 nm for each layer of coil-ring-coil block copolymers, which has been determined from the solid-state of **1c** by method of X-ray scattering of film reflection [Rosselli et al., 2003]. The possible arrangement of such 4 coil-ring-coil block copolymers (with distance of 0.6 nm between each other) into 1 nm length of aggregates is the formation of cylinder bundles, as shown in Fig. 6.11 (facing the cross-section), with coexistence of about 25% individual-, 25% bi-, and 50% tri-cylinder brushes. Such mixed cylinder bundles can give out the expected M_L , and the radius of individual cylinder brushes R_0 can be determined through fitting.

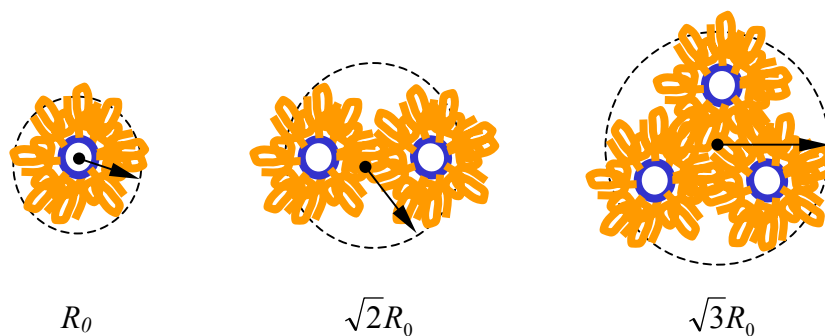


Fig. 6.11 Schematic description of bundles of individual-, bi- and tri-cylinder brushes (facing the cross-section) with effective radius R_0 , $\sqrt{2}R_0$ and $\sqrt{3}R_0$, respectively, corresponding to the equivalent scattering volume of a circular cylinder.

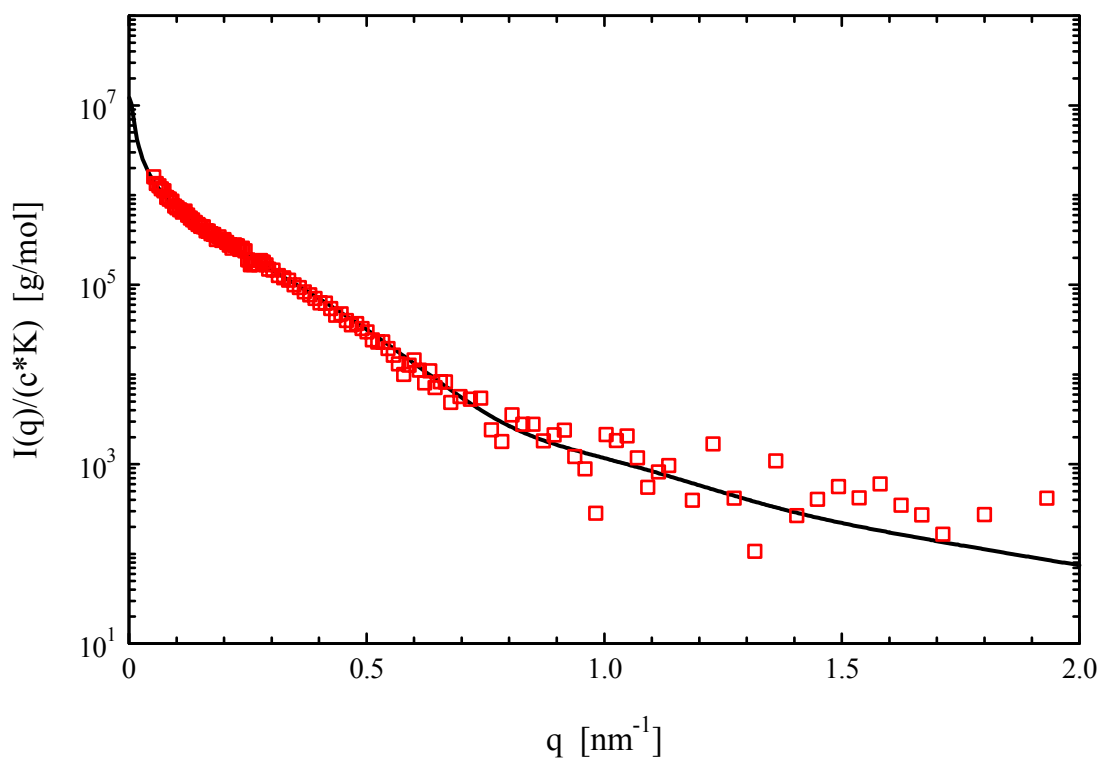


Fig. 6.12 Comparison of experimental form factor (open squares) with theoretical curve (solid line) of mixed bundles with coexistence of 25% individual-, 25% bi- and 50% tri-cylinder brushes. A hollow circular cylinder model was used for the individual cylinder brushes with $R_0 = 2.6$ nm, and a massive circular cylinder model was used for the bi- and tri-cylinder brushes with radius of $\sqrt{2}R_0$ and $\sqrt{3}R_0$, respectively. The whole length of these cylindrical objects is assumed to be 500 nm.

For such a complex system, the bi- and tri-cylinder bundles were approximated to circular cylinders with effective radii of $\sqrt{2}R_0$ and $\sqrt{3}R_0$, respectively, according to the equivalent scattering volume. The fitting was then executed by using a hollow circular cylinder model for the individual cylinder and a massive circular cylinder model for bi-, and tri-cylinder bundles with radius of $\sqrt{2}R_0$ and $\sqrt{3}R_0$, respectively. R_0 was determined to be 2.6 nm (polydispersity 20%) with a hollow inside of radius of 1.2 nm through the model fitting and the theoretical curve is shown in Fig. 6.12 by the solid line, in comparison with the experimental form factor. Since the present work is focused on the local structure of the cylindrical objects, the whole length of the cylindrical objects, which exceeds the experimental limit of the Kratky camera, is set to be 500 nm in the model calculation, according to the assumption of Höger et al. [Höger et al., 2004].

6.4 Conclusion

First of all, as observed by SAXS, the strong scattering intensity of **1c** solutions at low q range implies that the investigated coil-ring-coil block copolymers form suprastructural aggregates in solvent of cyclohexane, which may be of cylindrical shape due to the previous investigation of Höger et al..

The whole length of these cylindrical objects can be concluded to be longer than 200 nm, the exact value may be obtained by light scattering. In stead of that, a more valuable parameter, namely the molecular weight per unit length M_L was obtained to be 25730 ± 5100 g/(mol.nm) by SAXS data, which corresponds to the average association number about 4 per nm length of the cylindrical aggregates. With knowledge of $d = 0.6$ nm (distance between adjacent densely packed rings), the aggregates of **1c** can be concluded to be mixture of cylindrical bundles. The coexisted cylindrical bundles consist of probably individual hollow cylinder brushes with radius of 2.6 nm and a hollow inside ($R_{in} = 1.2$ nm), as well as bi- and tri-cylinder bundles with the same size parameters as individuals. The number ratio of single cylinder, bi- and tri-cylinder bundles is about 1:1:2.

7 Summary

The objective of this work is to analyze nano-scaled cylindrical particles by small angle X-ray scattering (SAXS). Three systems with cylinder-shaped particles: (1) Laponite particles in aqueous solutions, (2) Poly(carbon suboxide) particles in binary water/DMF solutions, and (3) Suprastructural aggregates of coil-ring-coil block copolymers in cyclohexane, have been studied by SAXS performing either a Kratky-Compact-Camera in our laboratory or ID2 beamline of the European Synchrotron Radiation Facility (ESRF) in Grenoble.

The synthetic clay particles, Laponites dispersed in a 10^{-3} mol/l NaCl solution at pH = 10, have been chosen as ideal disc-shaped model particles. In combination of SAXS with static light scattering (SLS), the scattering intensities of a concentration serial (volume fraction from 0.02% to 0.16%) were measured in almost three orders of magnitude of the scattering vector q . Through extrapolation of concentration the scattering intensity at vanishing concentration, i.e. the form factor $P(q)$ of particles was achieved. The form factor shows a q^{-2} decay at intermediate q range, which indicates that the shape of single Laponite particles in aqueous solution is platelet. The plateau of the form factor at low q range implies that there is no aggregate or cluster structure, and the Laponite particles are dispersed completely under the investigated conditions. More detailed structural information was then obtained by fitting of the extrapolated scattering function with disc-shaped particle model. The radii of the discs exhibit a large polydispersity. A radius of 10.5 nm with Schulz-Zimm distribution of $R_W/R_N = 1.5$ (where R_W and R_N denote weight and number average radius, respectively) was found to fit the form factor perfectly. The thickness of one single platelet was determined to be 0.9 nm from the plot of $\ln[I(q) \cdot q^2]$ vs. q^2 . The weight averaged molecular weight and radius of gyration were determined to be 930 ± 190 kg/mol and 13.4 nm, respectively. The inter-particle interactions of Laponite particles were investigated by the structure factor $S(q)$, from which the effective diameter of interparticle interactions d_{eff} was determined for the first time. The strong electrostatic Coulomb repulsion between charged Laponite particles was attributed to the much higher value of d_{eff} ($= 46 \pm 2$ nm), in comparison to $2R_g$ ($= 27$ nm) of Laponite particles. The recently developed multicomponent interaction site model was performed by Harnau to predict these experimental structure factors. An effective potential

of interaction, which pays attention to a screened Coulomb interaction as well as an attractive interaction, leads to the best description of the model to the experimental data.

By means of SAXS, the size of synthetic polymer carbon suboxide ((C₃O₂)_n) dissolved in binary water/DMF solutions was determined for the first time with radius of gyration $R_g = 1.7$ nm and molecular weight $M_w = 2760$ g/mol, which corresponds to a polymerization's degree of about 40. This value is much larger than literature data of 5-10. The form factor of polymer carbon suboxide can be described by a semiflexible chain model. The radius of gyration in cross-section R_C and molecular weight per unit length M_L were obtained to be 0.3 nm and 350 g/(mol.nm), respectively, which can confirm the fact that the chemical structure of poly(carbon suboxide) is repeated α -pyronic ring, as suggested in most literatures. The effect of solvent with different ratio of water/DMF on the conformation of dissolved polymer chains was investigated as well. With the weight fraction of DMF in solvent more than 40%, the structure and conformation of the polymer chains keep unchanged, however, without DMF in solvent at all, the scattering intensity increases dramatically, which is attributed to the formation of polymer aggregations with average association number of 6.

Finally, SAXS was employed to analyze a suprastructural aggregation system derived by self-assembly of coil-ring-coil block copolymers. This is a newly synthesized subclass of rod-coil block copolymers composed of a nanometer-sized shape-persistent macrocycle and two covalently attached polystyrene (PS) coils. The solubility of the rigid ring is largely enhanced due to the attachment of the flexible side groups. With suitable length of the flexible side groups (M_w (PS) = 2500 g/mol) the block copolymers can form colloidal-sized aggregates in selected solvent cyclohexane, which were concluded to be of cylindrical shape with the rigid rings packing densely in a tubular way and the flexible side groups arranging outside of the ring. Such aggregated cylinder brushes can be further confirmed to exist as a mixture of cylinder bundles by analyzing the local structural parameter M_L (= 25730 g/(mol.nm), molecular weight per nm length of cylindrical objects). In comparison of this value with M_0 (= 6500 g/mol, molecular weight of single coil-ring-coil block copolymer) and d (= 0.6 nm, distance of adjacent densely packed rings), the number fraction of coexisted single cylinder, bi- and tri-cylinder bundles was resulted to be 1:1:2. Through fitting by using approximated circular cylinder model the radius of single cylinders was determined to be 2.6 nm (polydispersity 20%) with a hollow inside of radius of 1.2 nm.

Zusammenfassung

Das Ziel der vorliegenden Arbeit ist die strukturelle Untersuchung von nanoskaligen zylinderförmigen Partikel mittels Röntgenkleinwinkelstreuung. Es wurden drei unterschiedliche Systeme zylinderförmiger Teilchen untersucht und zwar Laponit-Partikel in Wasser, Polymer-Kohlenstoffsuboxide in binären Wasser/DMF-Lösungen und Aggregate der Knäuel-Ring-Knäuel-Blockcopolymere in Cyclohexan. Die Untersuchungen wurden mittels einer Kratky-Kompakt-Kamera an der Universität Bayreuth und an der ID2-Beamline der European-Synchrotron-Radiation-Facility (ESRF) in Grenoble durchgeführt.

Zur Untersuchung scheibchenförmiger Systeme wurde Laponit als Modellsystem gewählt. Die Laponitpartikel ist in einer 10^{-3} mol/l NaCl Lösung (PH = 10) suspendiert. Durch Kombination von SAXS mit Lichtstreuung war es möglich, den q -Bereich um drei Größenordnungen zu erweitern. Die untersuchten Konzentrationen betragen 0.02 Vol-% bis 0.16 Vol-%. Durch Extrapolation der Streuintensität auf $c \rightarrow 0$ wurde der Formfaktor $P(q)$ ermittelt. Der Formfaktor weist einen Abfall von q^{-2} im mittleren q -Bereich der Streuintensitäten. Dieser Abfall ist ein Zeichen für die scheibchenförmige Gestalt der Laponit-Teilchen. Das Plateau des Formfaktors bei kleinen q -Werten bedeutet, dass die Partikel vollständig in Wasser suspendiert vorliegen und keine Aggregate oder Cluster bilden. Um detailliertere Information über die Struktur der Partikel zu gewinnen, wurden die extrapolierten Streuintensitäten mit dem Modell scheibchenförmiger Partikel verglichen. Der hierbei bestimmte Radius der Laponit-Teilchen weist eine Polydispersität auf. Weiterhin wurde festgestellt, dass die beste Beschreibung der experimentellen Daten bei einem Radius von 10.5 nm und unter Annahme einer Schulz-Zimm-Verteilung von $R_w/R_N = 1.5$ (R_w -Gewichtsmittel, R_N -Zahlenmittel) erhalten wurde. Die Dicke der einzelnen Scheibchen beträgt 0.9 nm. Dies wurde aus der Steigung der Auftragung $\ln[I(q)q^2]$ gegen q^2 berechnet. Das Massenmittel des Molekulargewichts beträgt 930 ± 190 kg/mol und der Gyrationradius 13.4 nm. Die Wechselwirkungen zwischen den Partikeln wurden mit Hilfe des Strukturformfaktors $S(q)$ untersucht, welcher den effektiven Durchmesser d_{eff} der interpartikulären Wechselwirkungen wiedergibt. Es wurde festgestellt, dass aufgrund starker elektronstatischer Coulomb-Wechselwirkungen zwischen den Laponit-Partikeln d_{eff} viel größer ist als $2R_g$. Der experimentelle bestimmte Strukturformfaktor wurde mit dem von Harnau entwickelten

„multicomponent interaction site model“ verglichen. Wenn man ein Wechselwirkungspotential verwendet, welches teilweise attraktiv ist, können die experimentelle Daten erfolgreich beschrieben werden.

Bei der Untersuchung der polymeren Kohlenstoffsuboxide $((C_3O_2)_n)$ wurde von der in der Literatur oft vorgeschlagenen Poly- α -Pyronstruktur ausgegangen. Die Konformation der Polymerketten wurde in Lösungen mit unterschiedlichem Wasser zu DMF-Verhältnis untersucht. Es wurde festgestellt, dass die Struktur und Konformation der Ketten mit der Erhöhung des Wasseranteils konstant bleiben. In reinem Wasser steigt die Streuintensität der Teilchen stark an, was auf eine Aggregation von durchschnittlich 6 Polymerketten hindeutet. Mit Hilfe der Guinier-Auftragung wurde M_w zu 2760 g/mol und R_g zu 1.7 nm für eine einzelne Polymerkette bestimmt. Der Polymerisationsgrad von 40 ist signifikant größer als bisher publizierte Werte von 5-10. Der Formfaktor der Polymerketten konnte über ein Modell für semiflexible Kette gefittet werden. Die lokale Struktur, nämlich der Gyrationradius im Querschnitt R_C und das Molekulargewicht pro 1 nm Teilchenlänge betragen 0.3 nm bzw. 350 g/(mol·nm). Dies stimmt sehr gut mit der angenommenen Poly- α -Pyronstruktur überein.

Schließlich wurden Aggregate selbstorientierender Knäuel-Ring-Knäuel-Blockcopolymere mit Hilfe der Röntgenkleinwinkelstreuung untersucht. Die in dieser Arbeit untersuchten Rod-Ring-Blockcopolymere bestehen aus einem formstabilen Makrozyklus und zwei am Makrozyklus kovalent gebundenen Polystyrolketten. Die Löslichkeit der steifen Ringe wird durch die Anbindung der Polymerketten erhöht. Bei geeigneter Länge der Polymerketten des Block-Copolymers werden sich kolloidale Aggregate ausbilden. Diese sind zylindersymmetrisch, wobei die starren Ringe röhrenartig angeordnet sind und die flexible Seitenketten der Ringe nach außen zeigen. Weiterhin konnte über die Analyse des lokalen Strukturparameters M_L (Molekulargewicht pro nm Länge der zylindrischen Objekte) gezeigt werden, dass derartige Zylinderbürsten zu zylindrischen Bündeln angeordnet sind. Unter Berücksichtigung von M_0 (Molmasse eines einzelnen Knäuel-Ring-Knäuel-Blockcopolymers) und d (Abstand benachbarter Ringe) wurde ein Zahlenverhältnis von einzel-, zwei- und dreisträngigen Bündeln von 1:1:2 erhalten. Über eine Anpassung unter Verwendung eines kreisförmigen Zylindermodells wurde der äußere Radius zu 2.6 nm und der innere Radius des Zylinders zu 1.2 nm bestimmt.

References

- Abou, B., Bonn, D. and Meunier, J., *J. Phys. Rev. E* **2001**, 64, 021510
- Apfel, U. ; Grunder, R.; Ballauff, M., *Colloid Polym. Sci.* **1994**, 272, 820
- Avery, R. G., Ramsay, J. D. F., *J. Colloid Interface Sci.* **1986**, 109, 448
- Ballauff, M.; Bolze, J.; Dingenouts, N.; Hickl, P.; Pötschke, D., *Makromol. Chem.* **1996**, 197, 3043
- Balnois, E., Durand-Vidal, S. and Levitz, P., *Langmuir* **2003**, 19, 6633
- Beaucage, G. ; Rane, S. ; and Sukumaran, S., et al., *Macromolecules* **1997**, 30, 4158
- Benoit, H.; Doty, P., *J. Phys. Chem.* **1953**, 57, 958
- Bhatia, S., Barker, J. and Mourchid, A., *Langmuir* **2003**, 19, 532
- Birkofer, L.; Sommer, P., *Chem. Ber.* **1976**, 109, 1701
- Blake, A. R.; Eeles, W. T. and Jennigs, P. P., *Trans. Faraday Soc.* **1964**, 60, 691
- Bolze, J., *Dissertation Karlsruhe*, **1997**
- Bolze, J.; Peng, B.; Dingenouts, N.; Panine, P.; Narayanan, T.; Ballauff, M.; *Langmuir* **2002**, 18,8364
- Bolze, J.; Pontoni, D.; Ballauff, M.;Narayanan, T.; Cölfen, H., *J. Colloid and Interface Science* **2004**, 277, 84
- Bonn, D., Tanaka, H., Wegdam, G., Kellay, H. and Meunier, J., *Europhys. Lett.* **1998**, 45, 52
- Bonn, D., Kellay, H., Tanaka, H., Webdam, G. and Meunier, J., *Langmuir* **1999**, 15, 7534
- Bösecke, P., *Rev. Sci. Instrum.* **1992**, 63, 438
- Brumberger, H., “*Modern Aspects of Small-Angle Scattering*”, Academic Publishers, **1995**
- Carofiglio, T.; Pandolfo, L. and Paiaro, G., *Eur. Polm. J.* **1986**, 6, 491
- Chen, J. T.; Thomas, E. L.; Ober, C. K.; Mao, G.-P., *Science* **1996**, 273, 343
- Debye, P., *Ann. Phys.* **1915**, 46, 809
- Debye, P., *J. Phys. Colloid. Chem.* **1947**, 51, 18-32
- Debye, P. and Bueche, A. M., *J. Appl. Phys.* **1949**, 20, 518
- de Gennes, P.-G., “*Scaling concepts in polymer physics*” **1979**, Cornell university press
- de Gennes, P. G. and Prost, J., “*The Physics of Liquid Crystals*” **1993**, Clarendon, Oxford
- Delville, A., *J. Phys. Chem. B* **1999**, 103, 8296
- Diels, O.; Wolf, B., *Ber. Deutsch. Chem. Ges.* **1906**, 39, 689
- Diels, O.; Meyerheim, G., *Chem. Ber.* **1907**, 40, 355

- Diels, O.; Beckmann, R.; Tönnies, G., *Liebigs Ann. Chem.* **1924**, 439, 76
- Dijkstra, M., Hansen, J.-P., and Madden, P. A., *Phys. Rev. E* **1997**, 55(3), 3044
- Dijkstra, M., Hansen, J.-P., and Madden, P. A., *Physical review letters* **1995**, 75, 2236
- Dingenouts, N., *Dissertation Karlsruhe*, ISBN 3-8265-6805-2, **1999**
- Dingenouts, N.; Bolze, J.; Pötschke, D.; Ballauff, M., *Adv. Polym. Sci.* **1999**, 144, 1
- Dingenouts, N.; Ballauff, M., *Acta Polymerica* **1998**, 49, 178
- Dingenouts, N.; Ballauff, M., *Macromolecules* **1998**, 31, 7423
- Dingenouts, N.; Bolze, J.; Pötschke, D. and Ballauff, M., *Advances in Polymer Science* **1999**, 144, 1
- Doi, M.; Edwards, S. F., “*The Theory of Polymer Dynamics*” **1986**, Oxford science publications, Clarendon Press: New York
- Ellern, A.; Drews, Thomas and Seppelt, K., *Z. Anorg. Allg. Chem.* **2001**, 627, 73
- Engelkamp, H.; Middelbeek, S.; Nolte, R. J. M, *Science* **1999**, 284, 785
- Föster, S.; Antonietti, M., *Adv. Mater.* **1998**, 10, 195
- Glatter, O. and Kratky, O., “*Small Angle X-ray Scattering*” **1982**, Academic Press, London
- Glatter, O. and Zipper, P., *Acta Physica Austriaca* **1975**, 43, 307
- Grimson, M. J., *J. Chem. Soc. Faraday* **1982**, 279, 817
- Grunder, R., *Dissertation Karlsruhe*, **1993**
- Guinier, A., *Ann. Phys.* **1939**, 12, 161
- Guinier, A and Fournet, G., “*Small Angle Scattering of X-Rays*”, Wiley, New York, **1955**
- Hansen, J.-P.; Hayter, J. B., *Mol. Phys.* **1982**, 46, 651
- Hansen, J.-P. and McDonald, I. R., “*Theory of simple liquids*” **1976**, Academic press,
- Harnau, L., Costa, D. and Hansen, J.-P., *Europhys. Letter* **2001**, 53(6), 729
- Harnau, L., Hansen, J.-P., *J. Chemical Physics* **2002**, 116(20), 9051
- Hayter, J. B.; Penfold, J., *Mol. Phys.* **1981**, 42, 109
- Hickl, P., *Dissertation Karlsruhe*, **1996**
- Hickl, P.; Ballauff, M.; Jada, A., *Macromolecules* **1996**, 29, 4006
- Hickl, P.; Ballauff, M., *Makromol. Chem. Macromol. Symp.* **1997**, 118, 683
- Hickl, P.; Ballauff, M.; Scherf, U.; Müllen, K.; Lindner, P., *Macromolecules*, **1997**, 30, 273
- Hoeger, S. Bonrad, K. Mourran, A. Beginn, U. Möller, M., *J. Am. Chem. Soc.* **2001**, 123, 5651
- Hoeger, S.; Enkelmann, V.; Bonrad, K.; Tschierske, C., *Angew. Chem.* **2000**, 112, 2356
- Hoeger, S., *Chem. Eur. J.* **2004**, 120, 1320
- Höger, S., *J. Polym. Sci.* **1999**, 37, 2685

- Höger, S.; Bonrad, K.; Rosselli, S.; Ramminger, A.-D.; Wagner, T.; Silier, B.; Wiegand, S.; Häußler, W.; Lieser, G.; Scheumann, *Macromol. Symp.* **2002**, 177, 185
- Israelachvili, J. N., “*Intermolecular and Surface Forces*” **1985**, Academic Press, New York
- Jenekhe, S. A.; Chen, X. L., *Science* **1999**, 283, 372
- Kerker, M., “*The Scattering of Light*”, **1969**, Academic Press, New York
- Kholodenko, A. L., *Macromolecules* **1993**, 26, 4179
- Kholodenko, A.; Ballauff, M.; Granados, M., *Physica A* **1998**, 260, 267
- Kirste, R. G. and Oberthür, R. C., in “*Small Angle X-ray Scattering*”, edited by Glatter, O. and Kratky, O., **1982**, 387, academic press
- Klok, H.-A.; Langenwalter, J. F.; Lecommandoux, S., *Macromolecules* **2000**, 33, 7819
- Klok, H.-A. ; Lecommandoux, S., *Adv. Mater.* **2001**, 13, 1217
- Koyama, R., *J. Phys. Soc. Jan.* **1974**, 36, 1409
- Kratky, O.; Porod, G., *Rec. Trav. Chim. Pays.-Bas* **1949**, 68, 1106
- Kratky, O., *Electrochem.* **1956**, 60, 245
- Kratky, O. and Skala, Z., *Z. Elektrochem.* **1958**, 62, 73
- Kratky, O., in “*Small Angle X-ray Scattering*”, edited by Glatter, O. and Kratky, O., **1982**, 53, academic press
- Kratky, O. and Müller, K., in “*Small Angle X-ray Scattering*”, edited by Glatter, O. and Kratky, O., **1982**, 499, academic press
- Kratky, O., in “*Small Angle X-ray Scattering*”, edited by Glatter, O. and Kratky, O., **1982**, 361, academic press
- Kroon, M., Wegdam, G. H., and Sprik, R., *Europhys. Lett.* **1996**, 35(8),621
- Kroon, M., Wegdam, G. H. and Sprik, R., *Physical Review E* **1996**, 54(6), 6541
- Kroon, M., Vos, W. L., and Wegdam, G. H., *Physical Review E* **1998**, 57(2), 1962
- Lide, D. R.(Editor in chief), *Handbook of chemistry and physics* 76th Edition, **1995-6**
- Kutter, S., Hansen, J.-P., Sprik, M. and Boek, E., *J. Chem. Phys.* **2000**, 112, 311
- Kybett, B. D.; Johnson, G. K.; Barker, C. K.; Margrave, J. L., *J. Phys. Chem.* **1965**, 69, 3603
- Lamaire, B. J., Panine, P., Gabriel J. C. P. and Davidson, P., *Europhys. Lett.* **2002**, 59(1), 55
- Lee, M.; Jeong, Y.-S.; Cho, B.-K., Oh, N.-K.; Zin, W.-C., *Chem. Eur. J.* **2002**, 8, 876
- Lee, M.; Cho, B.-K.; Zin, W.-C., *Chem. Rev.* **2001**, 101, 3869
- Lehn, J. M., “*Supramolecular Chemistry*”, VCH: Weiheim, Germany, **1995**
- Levitz, P. Mouchid, A. et al., *Europhysics Letters* **2000**, 49(5), 672
- Luzzati, V., *Acta Crystallogr.* **1960**, 13, 939

- Martin, C., Pignon, F., Piau, J.-M., Magnin, A., Lindner, P. and Cabane, B., *Phys. Rev. E* **2002**, 66, 021401
- Monovoukas, Y. and Gast, A. P., *J. Colloid Interface Sci.* **1989**, 128, 533
- Moonen, J. and Vrij, A., *Colloid Polym. Sci.* **1988**, 266, 1068
- Moonen, J. and Vrij, A., *Colloid Polym. Sci.* **1988**, 266, 1140
- Mori, Y., Togashi, K., Nakamura, K., *Advanced powder Technology* **2001**, 12(1), 45
- Morvan, M., Espinat, D., Lambard, J. and Zemb, Th., *Colloid and Surfaces A* **1994**, 82, 193
- Mourchid, A., Levitz, P. et al, *Langmuir* **1995**, 11, 1942
- Mourchid, A., Delville, A., and Levitz P., *Faraday Discuss.* **1995**, 101,275
- Mourchid, A., Delville, A., and Levitz, P., *Progr. Colloid Polym. Sci.* **1995**, 98, 39
- Mourchid, A., and Levitz, P. et al., *Langmuir* **1998**, 14, 4718
- Mourchid, A., and Levitz, P., *Physical Review E* **1998**, 57(5), 4887
- Muthukumar, M; Ober, C. K.; Thama, E. L., *Science* **1997**, 277, 1225
- Neugebauer, T., *Ann. Physik* **1943**, 42, 509
- Nicolai, T., and Cocard, S., *Langmuir* **2000**, 16, 8189
- Nicolai, T., and Cocard, S., *Eur. Phys. J. E* **2001**, 5, 221
- Nicolai, T. and Cocard, S., *J. Colloid and Interface Science* **2001**, 244, 51
- Onsager, L., *Ann. Acad. Sci.* **1949**, 51, 527
- Peterlin, A., *J. Polymer Science* **1960**, 47, 403
- Pignon, F., Magnin, A., Piao, J.-M., Cabane, B., Lindner, P. and Diat, O., *Physical Review E* **1997**, 56 (3), 3281
- Pignon, F., Piau, J.-M., and Magnin, A., *Physical review Letters* **1996**, 76(25), 4857
- Pignon, F., Magnin, A., and Piau, J.-M., *Physical review Letters* **1997**, 79(23), 4689
- Pignon, F., Magnin, A., and Piau, J.-M., *J. Rheol.* **1998**, 42 (6), 1349
- Pignon, F., Magnin, A., and Piau, J.-M., Cabane, B., Aimar, P., Meireles, M., Lindner, P., *J. Membrane Sci.* **2000**, 174, 189
- Pilz, I., in “*Small Angle X-ray Scattering*”, edited by Glatter, O. and Kratky, O., **1982**, 239, academic press
- Plummer, W. T. and Carson, R. K., *Science* **1969**, 166, 1141
- Pontoni, D.; Narayanan, T.; and Renne, A. R., *J. Applied Crystallography* **2002**, 35, 207
- Porion, P., Rodts, S., Al-Mukhtar, M., Faugere, A-M. and Delville, A., *Phys. Rev. Lett.* **2001**, 87(20), 208302
- Porion, P., Rodts, S., Al-Mukhtar, Meyer, S., M., Faugere, A-M., van der Maarel, J. R. C., and Delville, A., *J. Phys. Chem. B* **2001**, 105, 10505

- Porion, P., Faugere, M. P., Lecolier, E., Gheparadi, B., and Del ville, A., *J. Phys. Chem. B* **1998**, 102, 3477
- Porod, G., *Kolloid-Z.* **1951**, 124, 83
- Pötschke, D.; Hickl, P.; Ballauff, M.; Astrand, P.-O.; Pedersen, J. S., *Macromol. Theory and Simul.* **2000**, 9, 345
- Pötschke, D. and Ballauff, M., “*Structure and Dynamics of Polymer and Colloidal System*”, **2002**, 157-187, edited by Borsali, R. and Pecora, R., Kluwer Academic Publishers
- Pusey, P.N., in “*Liquid, Freezing and Glass Transitsion*” **1991**, 765, edited by Hansen, J.-P.; Levesque, D.; and Zinn Justin, J., North-Holland, Amsterdam
- Raez, J.; Manners, I.; Winnik, M. A., *J. Am. Chem. Soc.* **2002**, 124, 10381
- Ramsay, J. D. F., *J. Colloid and Interface Science* **1986**, 109(2), 441
- Ramsay, J. D. F. and Lindner, P., *J. Chem. Soc. Faraday Trans.* **1993**, 89, 4207
- Ramsay, J. D. F., Swanton, S. W. and Bunce, J., *J. Chem. Soc. Faraday Trans.* **1990**, 86, 3919
- Rawiso, M; Duplessix, R., and Picot, C., *Macromolecules* **1987**, 20, 630
- Rix, D., *J. Chem. Phys.* **1953**, 22, 429
- Rosenfeldt, S., Dingenouts, N., Ballauff, M., *Macromol. Chem. Phys.* **2002**, 203(13), 1995
- Rosselli, S.; Ramminger, A.-D.; Wagner, T.; Silier, B.; Wiegand, S.; Häußler, W.; Lieser, G.; Scheumann, V.; Höger, S., *Angew. Chem.* **2001**, 113, 3234
- Rosselli, S.; Ramminger, A.-D.; Wagner, T.; Lieser, G.; and Hoeger, S., *Chem. Eur. J.* **2003**, 9, 3481
- Rosta, L. and von Gunten, H. R., *J. Colloid and Interface Sci.* **1990**, 134, 397
- Rowan, D. G. and Hansen, J-P., *Langmuir* **2002**, 18, 2063
- Schmidt, P. W., “*Modern Aspects of Small-Angle Scattering*” (Edited by H. Brumberger), **1995**
- Schmidt, L.; Boehm, H. -P., und Hofmann, U., *Anorg. Allg. Chem.* **1958**, 296, 246
- Schmidt, P. W., *Acta Cryst.* **1965**, 19, 938
- Schulz, G. V. and Kirste, R. G., *Z. Physik. Chem. Neue Folg* **1961**, 30, 171
- Schweizer, K. S. and Curro, J. G., *Adv. Chem. Phys.* **1997**, 98, 1
- Smith, R. N.; Young, D. A.; Smith, E. N. and Carter, C. C., *Inorg. Chem.* **1963**, 2, 829
- Snow, A. W.; Haubenstock, H. and Yang, N. -L., *Macromolecules* **1978**, 11(1), 77
- Stabinger, H. and Kratky, O., *Makromol. Chem.* **1978**, 179, 1655
- Thomson, D. W. and Butterworth, J. T., *J. Colloid Interface Sci.* **1992**, 151, 236
- Thorson, W. R.; Nakagawa, I., *J. Chem. Phys.* **1960**, 33, 994

References

- Topp, A.; Bauer, B. J.; Tomalia, D. A.; Amis, E. J., *Macromolecules* **1999**, 32, 7232
- van Beurten, P., Vrij, A., *J. Chem. Phys.* **1981**, 74, 2744
- van Helden, A. K.; Vrij, A., *J. Colloid Int. Sci.* **1980**, 78, 312
- Veerman, J. A. C. and Frenkel, D., *Phys. Rev. A* **1992**, 45, 5632
- Vrij, A., *J. Chem. Phys.* **1979**, 71, 3267
- Whitesides, G. M.; Mathias, J. P.; Seto, C. P., *Science* **1991**, 254, 1312
- Willenbacher, N., *J. Colloid and Interface Science* **1996**, 182, 501
- Yang, N. L., Snow, A., Haubenstock, *Polymer Preprints (American Chemical Society, Division of Polymer Chemistry)* **1981**, 22(1), 52
- Zernicke, F. and Prins, J. A., *Physik* **1927**, 41, 184
- Ziegler, E., *Angew. Chem.* **1960**, 72, 582
- Zimm, B. H., *J. Chem. Phys.* **1948**, 16, 1093
- Zubarev, E. R.; Pralle, M. U.; Li, L.; Stupp, S. I., *Science* **1999**, 283, 523

Appendix

Appendix A Investigated samples of dissolved poly(carbon suboxide)

| <i>solvent</i> | | <i>concentration</i> | | | | |
|--------------------|-----------------|----------------------|--------------------|------------|-------------|----------------|
| <i>Water [wt%]</i> | <i>DMF[wt%]</i> | $(C_3O_2)_x[g]$ | <i>Solvent [g]</i> | <i>wt%</i> | <i>vol%</i> | <i>c [g/l]</i> |
| 5 | 95 | 0.0123 | 3.1599 | 0.384 | 0.223 | 3.661 |
| | | 0.0243 | 3.1467 | 0.765 | 0.445 | 7.313 |
| | | 0.0357 | 3.1540 | 1.119 | 0.651 | 10.703 |
| | | 0.0482 | 3.1532 | 1.505 | 0.878 | 14.418 |
| | | 0.0604 | 3.1546 | 1.878 | 1.097 | 18.021 |
| 10 | 90 | 0.0098 | 3.0124 | 0.324 | 0.178 | 3.121 |
| | | 0.0151 | 3.0116 | 0.498 | 0.273 | 4.803 |
| | | 0.0206 | 3.0170 | 0.677 | 0.372 | 6.537 |
| | | 0.0278 | 3.0179 | 0.912 | 0.501 | 8.810 |
| 30 | 70 | 0.0122 | 3.0085 | 0.402 | 0.236 | 3.877 |
| | | 0.0245 | 3.0116 | 0.805 | 0.473 | 7.772 |
| | | 0.0361 | 3.0329 | 1.176 | 0.691 | 11.353 |
| | | 0.0474 | 2.9936 | 1.557 | 0.917 | 15.069 |
| | | 0.0628 | 3.0028 | 2.047 | 1.208 | 19.850 |
| 60 | 40 | 0.0127 | 3.0222 | 0.418 | 0.250 | 4.110 |
| | | 0.0247 | 2.9992 | 0.816 | 0.489 | 8.029 |
| | | 0.0360 | 3.0049 | 1.184 | 0.710 | 11.665 |
| | | 0.0475 | 2.9988 | 1.560 | 0.937 | 15.399 |
| | | 0.0598 | 2.9981 | 1.954 | 1.175 | 19.312 |
| 0 | 100 | 0.0067 | 3.0119 | 0.221 | 0.135 | 2.218 |
| | | 0.0123 | 3.0044 | 0.407 | 0.249 | 4.092 |
| | | 0.0192 | 3.0077 | 0.633 | 0.388 | 6.372 |
| | | 0.0231 | 3.0042 | 0.764 | 0.468 | 7.695 |

Appendix B Derivation of eq. (2.22)

The scattering intensity of a cylindrical particle at $\frac{2\pi}{L} < q < \frac{1}{R_C}$ is given by [eq. (2.21)]

$$I_0(q) = H \cdot \frac{\pi}{q} \cdot (\Delta\rho)^2 \cdot A^2 \cdot \exp\left[-\frac{1}{2} R_C^2 q^2\right]$$

For a system with N_P identical dissolved rod-like particles (length H , radius of gyration in cross-section R_C) in volume V , the scattering intensity of this system

$$I(q) = \frac{N_P}{V} \cdot H \cdot \frac{\pi}{q} \cdot (\Delta\rho)^2 \cdot A^2 \cdot \exp\left[-\frac{1}{2} R_C^2 q^2\right]$$

$$\begin{aligned} \frac{N_P}{V} &= \frac{c}{M_w} \cdot N_A \\ &= \frac{c N_A}{M_w} \cdot \frac{\pi}{q \cdot H} \cdot V_P^2 \cdot (\Delta\rho)^2 \cdot \exp\left[-\frac{1}{2} R_C^2 q^2\right] \end{aligned}$$

$$\begin{aligned} \Delta n_e &= V_P \cdot \Delta\rho \\ &= \frac{c N_A}{M_w} \cdot \frac{\pi}{q \cdot H} \cdot (\Delta n_e)^2 \cdot \exp\left[-\frac{1}{2} R_C^2 q^2\right] \end{aligned}$$

$$\begin{aligned} \Delta n_e &= \Delta Z_2 \cdot M_w \\ &= \frac{M_w}{q \cdot H} \cdot \pi \cdot c \cdot N_A \cdot \Delta Z_2^2 \cdot \exp\left[-\frac{1}{2} R_C^2 q^2\right] \end{aligned}$$

$$\begin{aligned} K_{XS} &= N_A \cdot \Delta Z_2^2 \\ &= \frac{1}{q} \cdot M_L \cdot \pi \cdot c \cdot K_{XS} \cdot \exp\left[-\frac{1}{2} R_C^2 q^2\right] \end{aligned}$$

Publications

- Analyse des polymeren Kohlenstoffsuboxids durch Röntgen-Kleinwinkelstreuung
M. Ballauff*, L. Li, S. Rosenfeldt, N. Dingenouts, J. Beck* und P. Krieger-Beck
Angewandte Chemie **2004**, 116, 5967; Int. Ed. **2004**, 43(43), 5843
- An epoxy adhesive modified by Polyurethane
L. Li, X. Guo, *Chemistry and Adhesion* **1997**, 2, 63 (in Chinese)
- Effect of Organic Silicon on Polyurethane as Leather Finishing Agent
L. Li, X. Cheng, K. Xu, *Leather Chemicals* **1997**, 2, 11 (in Chinese)
- Structure's Effect on Property of Aqueous Polyurethane Dispersion used as Leather Finishing Agent
L. Li, K. Xu, X. Cheng, *J. Northwest Institute of Light Industry* **1994**, 12, 476 (in Chinese)

Erklärung

Die vorliegende Arbeit wurde von mir selbstständig verfasst und ich habe dabei keine anderen als die angegebenen Hilfsmittel und Quellen benutzt.

- Kapitel 4: Die SAXS-Messungen der Laponit-Partikel an der ID2-Beamline der European-Synchrotron-Radiation-Facility (ESRF) in Grenoble wurde von Dr. Sabine Rosenfeldt, Mushtaq Partel und Björn Haupt durchgeführt.

Ferner habe ich nicht versucht, anderweitig mit oder ohne Erfolg eine Dissertation einzureichen oder mich der Doktorprüfung zu unterziehen.

Bayreuth, den 05.01.2005

Li Li